N° d'ordre : 40837

THESE

Présentée à

L'UNIVERSITE DES SCIENCES ET TECHNOLOGIES DE LILLE

-UNIVERSITE LILLE NORD DE FRANCE-

Ecole Doctorale Sciences Pour l'Ingénieur

En vue de l'obtention du grade de

DOCTEUR DE L'UNIVERSITE

Spécialité : Micro et Nanotechnologies, Acoustique et Télécommunications

Par

Aurélien GAUTHIER-BRUN

GROWTH AND CHARACTERIZATION OF NITRIDE-BASED SEMICONDUCTOR MATERIALS APPLICATION TO HIGH-SPEED PHOTODIODES

Soutenue le 29 juin 2012

Directeur de thèse :	M. Elhadj DOGHECHE	Professeur à l'Université de Valenciennes
Co-encadrant :	M. Didier DECOSTER	Professeur à l'Université de Lille 1
Rapporteurs :	M. Abderrahim RAMDANE	Chargé de Recherche au Laboratoire de Photonique et de Nanostructures, Marcoussis
	M. Jean-Louis COUTAZ	Professeur à l'Université de Savoie
Examinateurs :	M. CHUA Soo Jin	Professor at the National University of Singapore
	M. TENG Jinghua	Senior Scientist at the Institute of Materials Research and Engineering, Singapore
	M. Tuami LASRI	Professeur à l'Université de Lille 1
	M. Jean CHAZELAS	Directeur de Recherche Associé, Thales Systèmes Aéroportés, Elancourt

INSTITUT D'ELECTRONIQUE DE MICROELECTRONIQUE ET DE NANOTECHNOLOGIE

Acknowledgements

The results presented in this thesis are the outcome of a collaboration work between the Institute of Electronics, Microelectronics and Nanotechnology (IEMN), the Institute of Materials Research and Engineering (IMRE) and Thales. I would like to thank Prof. A. Cappy and Prof. L. Buchaillot, directors of IEMN, as well as Dr. Lim K.W. and Prof. A. Hor, directors of IMRE for welcoming me in their laboratories, respectively as a member of Prof. D. Decoster's and Prof. Chua S.J.'s research groups.

I also thank the members of my jury, beginning with its president Dr. T. Lasri. Prof. A. Ramdane and Prof. J.L. Coutaz were the reviewers of this work and I strongly appreciate their in-depth assessment. I thank the other members of the panel, Dr. Teng J.H. (IMRE) and Dr. J. Chazelas (Thales Airborne Systems) for the time and attention they spent examining and discussing this research.

This thesis would not have been possible without the resources and support provided by my thesis director, Prof. E. Dogheche and my supervisor in Singapore Dr. Teng J.H., whose insight, mentoring and dedication were a constant help to me.

I also recognize the probing discussions, guidance, friendship and encouragement I received from Prof. E. Dumont, Dr. A. Gokarna, Prof. J.F. Lampin, Dr. D. Yarekha, Dr. Liu W., N. Ang, Dr. Guo H.C., R. Tan, Dr. S. Tripathy, Chew A.B., Wee Q.X., Dr. Zhang K., Dr. H. Tanoto, Dr. Wang B., Dr. S. Wu, Dr. J. Yang, , Dr. A. Stolz, T. Aviles, E. Wijaya, Dr. F. Leroy, D. Cherfi, Dr. A. Pagies, I. Saraswati, Dr. J. Harahi, Dr. V. Magnin, Dr. J.P. Vilcot, Dr. C. Sion, Dr. M. Halbwax, M. Pawlik, B. El Zein, Dr. E. Moreau, C. Legrand, P. Tilmant, M. François, Y. Deblock, B. Grimbert, A. Leroy, A. Mynard, and many more.

A final thanking word goes to the French Embassy in Singapore and its Attaché for Science and Higher Education Dr. W. Benzarti for their support awarded through the MERLION cooperation program.

Table of Content

ACKNOWLEDGEMENTS .... **I**

TABLE OF CONTENT .... **III**

LIST OF FIGURES .... **V**

LIST OF TABLES .... **VII**

INTRODUCTION **1**

CHAPTER 1 III-NITRIDE SEMICONDUCTORS IN MICROELECTRONICS **3**

1.1 FUNDAMENTAL PROPERTIES 4
1.2 GROWTH OF GAN AND INGAN 7
1.2.1 Choice of a substrate 7
1.2.2 Nucleation layer 8
1.2.3 Doping 10
1.2.4 InGaN growth 11
1.2.4.1 The InN challenge 11
1.2.4.2 InGaN growth model 12
1.2.4.3 Lattice mismatch and strain 14
1.2.4.4 Inhomogeneity and phase separation 14
1.3 OPTOELECTRONICS APPLICATIONS OF GAN AND INGAN 17
1.4 MOTIVATIONS AND OBJECTIVES OF THE THESIS 18
REFERENCES 19

CHAPTER 2 GROWTH AND CHARACTERIZATION OF INGAN THIN FILMS **25**

2.1 GROWTH OF INGAN THIN FILMS 26
2.1.1 Introduction to MOCVD 26
2.1.2 Experimental InGaN growth process 27
2.1.2.1 GaN growth 27
2.1.2.2 InGaN growth 29
2.2 STRUCTURE AND COMPOSITION CHARACTERIZATION OF INGAN THIN FILMS 33
2.2.1 InGaN monolayer thin films characterization 33
2.2.1.1 Microscopy 33
2.2.1.2 X-ray diffraction 36
2.2.1.3 Photoluminescence 39
2.2.1.4. Secondary ion-mass spectrometry 41
2.2.1.5 Summary 43
2.2.2 InGaN multilayer thin films characterization 44
2.2.2.1 Microscopy 44
2.2.2.2 X-ray diffraction 46
2.2.2.3 Photoluminescence 47
2.2.2.4 Secondary ion-mass spectrometry 48
2.2.2.5 Summary 50
2.2.3 Structures and compositions summary 51
REFERENCES 52

CHAPTER 3 OPTICAL CHARACTERIZATION OF INGAN THIN FILMS IN THE VISIBLE DOMAIN **57**

3.1 THE ELLIPSOMETRY OPTICAL CHARACTERIZATION METHOD 60
3.1.1 Interaction of an electromagnetic wave with a medium 60

3.1.1.1 Propagation of an electromagnetic wave through a medium [9,10] 60
3.1.1.2 Propagation of a polarized electromagnetic wave [9,11] 63
3.1.1.3 Interaction of an electromagnetic wave with a sample [12] 64
3.1.2 Modeling the optical response of a thin film on a substrate 66
3.1.2.1 Physical principle 67
3.1.2.2 Ideal thin films 67
3.1.2.3 Non-ideal thin films 73
3.1.3 Measures analysis methodology 77
3.1.3.1 Definition and determination of the parameters of the model 77
3.1.3.2 Regularization 78
3.2 EXPERIMENTAL STUDY OF INGAN THIN FILMS 79
3.2.1 Experimental study of a GaN thin film 80
3.2.2 Experimental study of InGaN thin films 82
REFERENCES 85
CHAPTER 4 OPTICAL CHARACTERIZATION OF INGAN THIN FILMS IN THE TERAHERTZ DOMAIN 89
4.1 THE TERAHERTZ TIME-DOMAIN SPECTROSCOPY [15] 91
4.1.1 Single layer 93
4.1.1.1 For optically thick samples 94
4.1.1.2 For optically thin samples 94
4.1.2 Thin film on a substrate 95
4.2 EXPERIMENTAL STUDY OF INGAN THIN FILMS 97
4.2.1 Experimental study of a GaN thin films 98
4.2.2 Experimental study of InGaN thin films 100
REFERENCES 104
CHAPTER 5 APPLICATION – FABRICATION OF AN INGAN-BASED TERAHERTZ PHOTODIODE 107
5.1 TERAHERTZ SOURCES 108
5.1.1 Electronics approach 109
5.1.1.1 Transistor-based oscillators 109
5.1.1.2 Resonant tunneling diodes 110
5.1.1.3 Frequency conversion 112
5.1.2 Optics approach 112
5.1.2.1 Gas lasers 112
5.1.2.2 Quantum cascade lasers 113
5.1.3 Optoelectronics approach 114
5.2 ULTRAFAST PHOTODIODE FOR TERAHERTZ GENERATION 115
5.2.1 Design of a terahertz photodiode 116
5.2.2 Fabrication of a terahertz photodiode 118
5.2.2.1 Growth of the structure 118
5.2.2.2 Technological steps for the fabrication of the photodiode 118
5.3 CONCLUSION AND PERSPECTIVES 124
REFERENCES 125
CONCLUSION 129
PUBLICATIONS AND COMMUNICATIONS 131
ABSTRACT 134

List of figures

Figure 1.1: Zinc-blende (left) and wurtzite (right) crystallographic structures. Larger and smaller spheres represent cations and anions, respectively 4
Figure 1.2: Bangap energy vs. lattice constant a for III-nitrides at 300 K 5
Figure 1.3: Bandgap of $In_xGa_{1-x}N$ as a function of indium composition x according to Eq. (1.1) and (1.2) 6
Figure 1.4: Schematic representation of a GaN film grown on a sapphire substrate 9
Figure 1.5: Equilibrium nitrogen vapor pressures of common III-V semiconductors 11
Figure 1.6: Reaction pathways for In adatoms on a growth surface 12
Figure 1.7: Cracking efficiency of NH3 as a function of temperature 13
Figure 1.8: Phase diagrams of (a) relaxed and (b) strained $In_xGa_{1-x}N$ films 15
Figure 1.9: Band-bending in a quantum well due to the piezoelectric field 16
Figure 2.1: IMRE MOCVD reactor 27
Figure 2.2: Temperature profile of the GaN growth process 29
Figure 2.3: Structures of the GaN template (left) InGaN samples (middle) and InN sample (right) 31
Figure 2.4: Structures of the studied InGaN multilayer samples 32
Figure 2.5: SEM images of samples InGaN-1 (left) and InN (right) 33
Figure 2.6: TEM images of samples InGaN-1 (left), InGaN-2 (center) and InGaN-3 (right) 34
Figure 2.7: Schematic view of a v-defect 35
Figure 2.8: TEM images of v-pits in sample InGaN-1 (left), InGaN-2 (center) and InGaN-3 (right) 35
Figure 2.9: AFM picture of the v-defects on sample InGaN-1 36
Figure 2.10: Conditions required for Bragg diffraction 37
Figure 2.11: (0002) XRD scans of samples InGaN-1 (black), InGaN-2 (red), InGaN-3 (blue) and InN (green) 38
Figure 2.12: Normalized room-temperature micro-PL emission spectra for samples InGaN-1 (black), InGaN-2 (red), InGaN-3 (blue) and InN (green) 39
Figure 2.13: SIMS profiles of samples InGaN-1 (black), InGaN-2 (red) and InGaN-3 (blue) 41
Figure 2.14: SIMS profile of the InN sample for In (solid) and Ga (dashed) 42
Figure 2.15: SEM images of samples InGaN-1-ML (top center), InGaN-2-ML (bottom left) and InGaN-3-ML (bottom right) 44
Figure 2.16: TEM image of sample InGaN-3-ML 45
Figure 2.17: (0002) XRD scans of samples InGaN-1-ML (black), InGaN-2-ML (red) and InGaN-3-ML (blue) 46
Figure 2.18: Normalized room-temperature micro-PL emission spectra for samples InGaN-1-ML (black), InGaN-2-ML (red) and InGaN-3-ML (blue) 47
Figure 2.19: SIMS profiles of samples InGaN-1-ML (black), InGaN-2-ML (red) and InGaN-3-ML (blue) 49
Figure 3.1: Principle diagram of the prism coupling technique 58
Figure 3.2: Reflection spectra at 1539 nm for polatizations s and p (left); dispersion of the refraction index as a function of wavelength measured by prism coupling and comparison to literature (right) 59
Figure 3.3: Principle diagram of the ellipsometry technique 60
Figure 3.4: Elliptical polarization diagram 64
Figure 3.5: Definition of the reflected and transmitted electric fields for a sample 65
Figure 3.6: Reflection and transmission at an interface 68
Figure 3.7: Reflection and transmission in a thin film on a substrate 69
Figure 3.8: Reflection and transmission in a stack of thin films 71
Figure 3.9: Microstructure and index profile for ideal and real films 74
Figure 3.10: Decomposition of a non-homogeneous optical index profile into homogeneous films 75
Figure 3.11: Profile indices of a smooth and a rough interface; equivalence with interface diffusion 76
Figure 3.12: Schematic representation and profile index of a non-ideal thin film on a substrate 76

Figure 3.13: Spectroscopic ellipsometry cos(Δ) (left) and tan(Ψ) (right) results showing the experimental data (black plain lines) and the best numerical fit (red dotted line) for GaN 80
Figure 3.14: Extracted values (red) of refractive index (left) and extinction coefficient (right) for GaN with comparative results from prism coupling (blue) along s (plain) and p (dotted) polarizations 81
Figure 3.15: Index profiles for the best numerical fits for GaN at 458 nm (black) and 633 nm (red) 82
Figure 3.16: Spectroscopic ellipsometry cos(Δ) (left) and tan(Ψ) (right) results showing the experimental data (black plain lines) and the best numerical fit (red dotted line) for InGaN 82
Figure 3.17: Extracted values of refractive index (left) and extinction coefficient (right) for samples InGaN-1 (black), InGaN-2 (red), InGaN-3 (blue) and GaN (green) 83
Figure 3.18: Index profiles for the best numerical fits (left) at 458 nm (black) and 633 nm (red) and layer structure (right) for sample InGaN-2 84
Figure 4.1: The "THz gap" 90
Figure 4.2: Schematic diagram of the THz-TDS set-up 92
Figure 4.3: THz signals without (black) and with (red) sample in the time (left) and frequency (right) domains 92
Figure 4.4: Transmission (left) and phase shift (right) of the complex transmission coefficient, ratio of the THz signals with and without a sample 93
Figure 4.5: THz-TDS measurements necessary for the analysis of a thin film deposited on a substrate 95
Figure 4.6: THz signals without any sample (black), with a substrate (red) and with a thin film on a substrate (blue) in the time (left) and frequency (right) domains 96
Figure 4.7: Etched sample and measured signals necessary to the THz-TDS analysis 98
Figure 4.8: Refractive indices (left) and extinction coefficients (right) of samples GaN-1 (black plain line), GaN-2 (red dashed line) and GaN-3 (blue dotted line) and comparison with values provided in other works [10-13] 99
Figure 4.9: Refractive indices (left) and extinction coefficients (right) of samples GaN-1 (plain black), InGaN-1 (red), InGaN-2 (blue), InGaN-3 (green) and InN (dotted black) 100
Figure 4.10: Conductivity functions for GaN-1 (top), InGaN-2 (middle) and InN (bottom) samples 102
Figure 5.1: THz emission power as a function frequency. Ovals denote recent THz sources. 108
Figure 5.2: Typical layer structure of a HEMT 109
Figure 5.3: Typical layer structure of HBT 110
Figure 5.4: Typical layer structure of a resonant tunneling diode 111
Figure 5.5: Step by step building of the current-voltage characteristics of a resonant tunneling diode 111
Figure 5.6: Schematic diagram of the conduction band in the active region of a QCL 113
Figure 5.7: Principle diagram of a THz optoelectronic source 114
Figure 5.8: Laser-gated photoconductive semiconductor antenna 115
Figure 5.9: Band structure of a UTC photodiode 116
Figure 5.10: Suggested UTC photodiode design using an InN absorption layer and an InGaN collector 117
Figure 5.11: MOCVD-grown layer structure 118
Figure 5.12: Step-by-step technological etching process 120
Figure 5.13: Step-by-step technological planarization process 120
Figure 5.14: Step-by-step technological metallization process 122
Figure 5.15: Masks for the design of the photodiodes. Global view of the semi-wafer (top), inserts detail one antenna (top left corner) and one photodiode (top right corner). Devices with coplanar lines are added for electrical microwave testing (bottom) 123

List of tables

Table 1-1: Basic parameters for binary wurtzite III-nitrides at 300 K 6
Table 1-2: Properties of GaN, InN and some of their potential substrates 8
Table 2-1: Experimental conditions of the GaN growth steps 28
Table 2-2: List of the studied GaN samples 29
Table 2-3: Experimental conditions of the InGaN growth 30
Table 2-4: List of the studied InGaN samples 31
Table 2-5: List of the studied InGaN multilayer samples 32
Table 2-6: Layer thicknesses of the InGaN monolayer samples 34
Table 2-7: XRD results for the InGaN monolayer samples 38
Table 2-8: Micro-PL results for the InGaN monolayer samples 40
Table 2-9: SIMS results for the InGaN monolayer samples 43
Table 2-10: Structures of the InGaN monolayer samples summary 43
Table 2-11: Composition of the InGaN monolayer samples summary 43
Table 2-12: Layer thicknesses of the InGaN multilayer samples 45
Table 2-13: XRD results for the InGaN multilayer samples 47
Table 2-14: Micro-PL results for the InGaN multilayer samples 48
Table 2-15: SIMS results for the InGaN multilayer samples 49
Table 2-16: Structures of the InGaN multilayer samples summary 50
Table 2-17: Composition of the InGaN multilayer samples summary 50
Table 2-18: Structure and composition of the samples used for the rest of this study 51
Table 4-1: Carrier concentrations and mobilities from THz-TDS analysis and Hall effect measurements for GaN samples 99
Table 4-2: Carrier concentrations and mobilities from THz-TDS analysis and Hall effect measurements for GaN, InGaN and InN samples 101

Introduction

Long regarded as a scientific curiosity, III-nitrides have attracted significant attention in science and technology of semiconductor devices and have earned substantial commercial interest for modern electronics and optoelectronics devices. Every alloy of this group has a direct bandgap ranging from 0.7 eV (InN) to 3.4 eV (GaN) and 6.2 eV (AlN) which covers the entire visible, near-ultraviolet and near-infrared portions of the electromagnetic wave spectrum. Therefore, devices performing in this wide spectral range can be tailored by adjusting the composition of binary alloys. There is also great scientific interest as this material system appears to form one of the first semiconductor material systems in which extended defects do not affect severely the optical properties of the devices. Moreover, nitride-based devices are the most environmentally friendly of the compound semiconductors. InGaN/GaN structures constitute an indispensable part of the III-nitrides-based devices. The recently identified smaller bandgap of InN implies that $In_xGa_{1-x}N$ can be utilized for optoelectronic applications in a broader spectral range than previously suspected. All these properties render the InGaN materials system indispensable for development of optoelectronics applications such as LEDs and LDs. Despite recent technological advances, a number of questions regarding fundamental material aspects have been left unanswered.

This is the main question that first drove the collaboration of the Institute of Electronics, Microelectronics and Nanotechnology (IEMN, Lille, France) and the Institute of Materials Research and Engineering (IMRE, Singapore). Within the framework of the Hubert Curien MERLION program from the Embassy of France in Singapore, both institutes decides to start a research project with the goal of improving the global knowledge on III-nitrides in general, and InGaN in particular, which laid the foundations of this thesis.

Benefiting the strong capabilities of IMRE for epitaxial growth and material characterization and the ability of IEMN to complete structural characterization and lead optical characterization, I have been given a unique chance to describe precisely a set of InGaN samples and determine their optical indices. Work is first focused on the visible and near infrared range. Outside collaborators suggested that InGaN was also a very potent candidate for applications in the terahertz range and that fundamental properties in this domain were absolutely unkown.

The terahertz (THz) frequency range lies from 0.3 THz to 10 THz, which corresponds to wavelengths between 1 mm and 30 µm. It is an exceptionally underused domain of the electromagnetic spectrum, although THz radiations have a great number of potential applications in several domains: spectroscopy in physics, in chemistry (gas detection, pollution and environment control), in astronomy (detection of gas, atoms and ionized molecules), in telecommunications (wireless and broadband networks, short range networks, radars), in industrial imaging (materials, devices and systems controlling), in medicine (detection of caries, oncology) or in security (detection of weapons and dangerous materials). Therefore the realization of devices able to operate at these frequencies has great potential still held back by the lack of efficient sources and detectors. There is however a huge international effort to develop low-cost, reliable, compact and tunable sources, able to operate continuously at ambient (or near-ambient) temperature and compatible with the standard technologies to achieve easy integration in complex systems and circuits. In this race, III-nitrides possess a number of electrical and optical advantages that would make it a solution to the emission/reception bottleneck.

This study is composed of 5 chapters, each treating a separate aspect of the issues we've exposed so far. Chapter 1 establishes the ground knowledge we need on III-nitrides to understand what the state of the art in the global research community is to date. Chapter 2 details the growth and microstructural/compositional characterization of our samples. Chapter 3 and 4 follow the similar goal to determine the optical indices of several $In_xGa_{1-x}N$ samples in the visible/near-infrared and THz frequency ranges respectively. Finally, we broaden in chapter 5 the focus of our study by suggesting and discussing the design and fabrication process of a THz photodiode.

Chapter 1
III-nitride semiconductors in microelectronics

CHAPTER 1 III-NITRIDE SEMICONDUCTORS IN MICROELECTRONICS 3

1.1 FUNDAMENTAL PROPERTIES 4
1.2 GROWTH OF GAN AND INGAN 7
1.2.1 Choice of a substrate 7
1.2.2 Nucleation layer 8
1.2.3 Doping 10
1.2.4 InGaN growth 11
1.2.4.1 The InN challenge 11
1.2.4.2 InGaN growth model 12
1.2.4.3 Lattice mismatch and strain 14
1.2.4.4 Inhomogeneity and phase separation 14
1.3 OPTOELECTRONICS APPLICATIONS OF GAN AND INGAN 17
1.4 MOTIVATIONS AND OBJECTIVES OF THE THESIS 17
REFERENCES 19

1.1 Fundamental properties

The III-nitride materials are referring to compounds of group III elements with nitrogen, commonly known as aluminum nitride (AlN), gallium nitride (GaN), indium nitride (InN) and their alloys.

III-nitrides crystallize into two crystallographic structures: the cubic zinc-blende and the hexagonal wurtzite structures, but the more commonly studied allotrope is the wurtzite one, as it is the more thermodynamically stable form under ambient conditions. Nitrogen atoms form a hexagonal close packed structure and the group III atoms occupy half of the tetrahedral available sites as shown in Figure 1.1 [1].

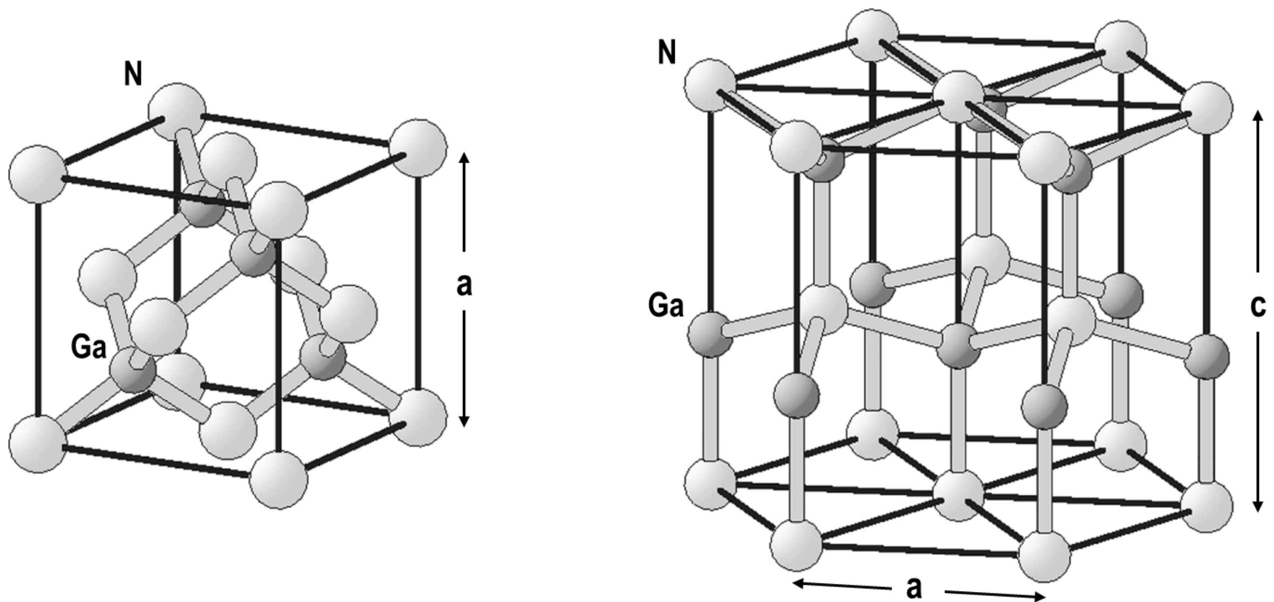

Figure 1.1: Zinc-blende (left) and wurtzite (right) crystallographic structures. Larger and smaller spheres represent cations and anions, respectively

What makes the III-nitride alloy system particularly suitable for optoelectronics is its direct bandgap, which covers continuously the entire visible, near ultraviolet and near infrared portions of the electromagnetic wave spectrum as illustrated in Figure 1.2 [2].

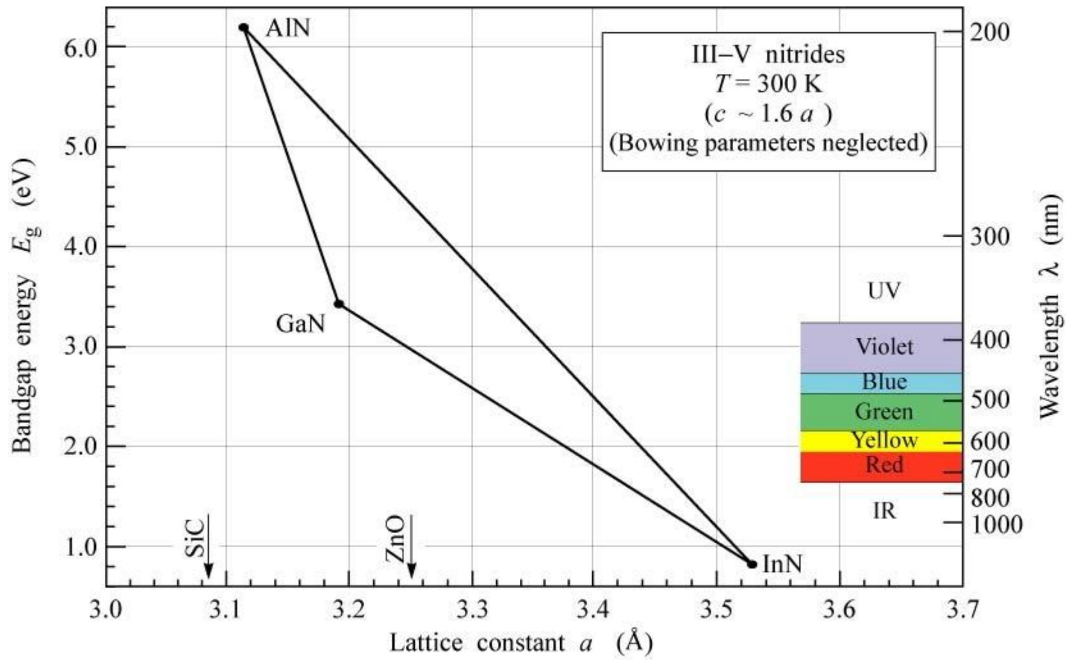

Figure 1.2: Bangap energy vs. lattice constant a for III-nitrides at 300 K

The bandgap energy for GaN is 3.4 eV [3]. Early studies reported values of 1.8 to 2 eV for InN [4] but improvements in epitaxial growth techniques eventually lead to a bandgap around 0.76 eV [5,6]. The bandgap energy of the ternary alloy $In_xGa_{1-x}N$ is calculated as [7,8]:

$$\boldsymbol{E_g(x) = x \cdot E_g(InN) + (1 - x) \cdot E_g(GaN) - b(x) \cdot x \cdot (1 - x)} \qquad (1.1)$$

where the bowing parameter b(x) accounts for the deviation from a linear interpolation between GaN and InN:

$$\boldsymbol{b(x) = (1 - x) \cdot (11.4 - 19.4 \cdot x)} \qquad (1.2)$$

Equation (1.2) was determined experimentally and provides values for the bowing parameter such as b(0.25)=4.9, b(0.5)=0.9 and b(0.75)=-0.8. Figure 1.3 represents the evolution of $E_g(x)$.

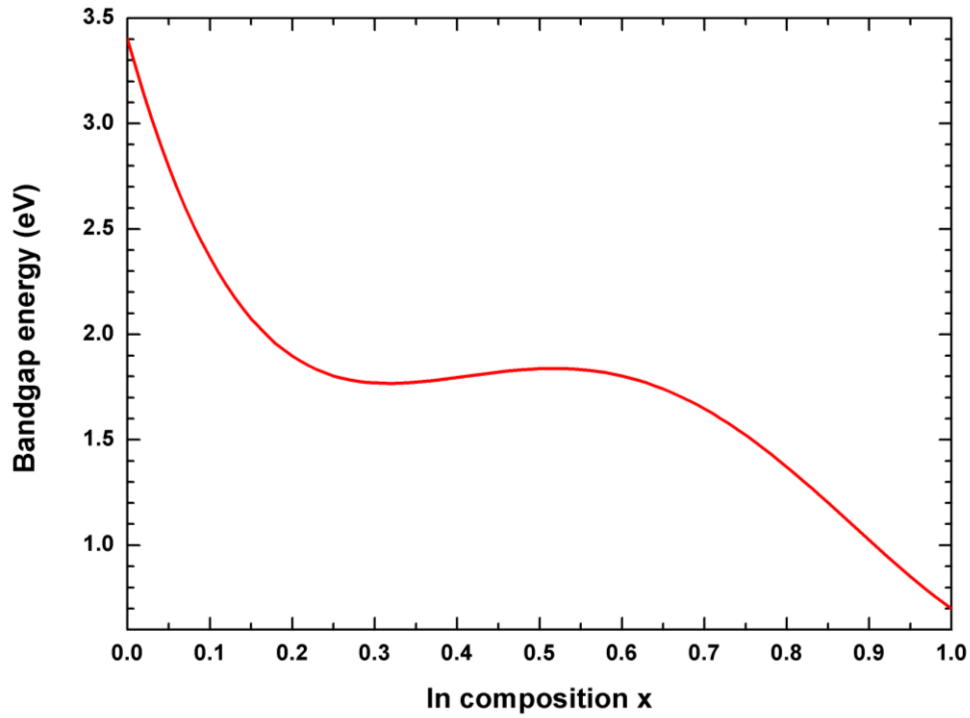

Figure 1.3: Bandgap of $In_xGa_{1-x}N$ as a function of indium composition x according to Equ. (1.1) and (1.2)

Table 1-1 presents some basic parameters for the wurtzite III-nitride binary compounds [5,6,9,10].

Parameters	**AlN**	**GaN**	**InN**
Lattice constant a (Å) c (Å)	 3.112 4.982	 3.189 5.185	 3.548 5.760
Poisson's ratio ν	0.202	0.205	0.272
Bandgap energy E_g (eV)	6.2	3.4	0.7
Electron mobility μ_e (cm^2/V.s)	300	1100	3200
Dielectric constant ε_r	9.1	8.9	15.3
Electron saturation velocity V_{sat} (× 10^7 cm/s)	1.8	2.7	4.4
Effective electron mass m_e^* (m_0)	0.3	0.22	0.14

Table 1-1: Basic parameters for binary wurtzite III-nitrides at 300 K

1.2 Growth of GaN and InGaN

The emergence of III-nitrides-based devices has been made difficult by a number of technical challenges associated with the growth and processing of the materials. Developing sophisticated growth techniques, finding suitable substrates and achieving doping, especially p-type, have been slowing down the rise of this system.

GaN was first synthesized in 1910 [11] and crystals were grown in 1932 by *Johnson et al.* by reacting metallic gallium with ammonia gas at 900-1000°C [12], but the material was polycrystalline and could not be used for semiconductors devices. It's only much later, with the development of modern epitaxial growth techniques, that GaN single crystals on sapphire substrate were achieved: first by hydride vapor phase epitaxy (HVPE) in 1969 [13], then in 1971 by metalorganic chemical vapor deposition (MOCVD) [14] and in 1974 by molecular beam epitaxy (MBE) [15].

1.2.1 Choice of a substrate

Due to its high melting temperature (over 2500°C), GaN crystals cannot be produced by typical techniques like Czochralski or Bridgeman, which means that homoepitaxy is not possible. Instead, the heteroepitaxy of GaN lead to an intensive search for suitable substrates [10, 16]. Such substrates have different physical properties compared to those of III-nitrides, especially lattice constants and thermal dilatation coefficients. These differences increase the stress of the grown layers and the misfit and threading dislocation densities, causing higher leakage currents and poorer thermal dissipation. Table 1-2 details the properties of the most popular substrates used to grow GaN [17].

Parameters	**GaN**	**InN**	**Si (111)**	**6H-SiC (0001)**	**Al_2O_3 (0001)**
Crystal structure	wurtzite	wurtzite	diamond	wurtzite	wurtzite
Lattice constant a (Å)	3,189	3,548	5,431	3,081	4,785
Lattice constant c (Å)	5,185	5.760	-	15,117	12,991
Lattice mismatch with GaN	0%	+11%	+17%	-3,4%	-16%
Thermal dilatation coeff. α_c ($\times 10^{-6}$ K^{-1})	3,17	2,9	2,6	4,7	4,3
Approximate price of a 2in-wafer (USD)	3000	-	30	1000	100

Table 1-2: Properties of GaN, InN and some of their potential substrates

Silicon is the substrate of choice for many applications in micro- and nanotechnologies and is still an interesting option for III-nitrides as it is well-established, well-known and very affordable, but it has a different crystal structure (diamond cubic) and the lattice mismatch with GaN is large (17%).

Silicon carbide (SiC) on the other end presents a much closer lattice matching (-3.4%) and already possesses a wurtzite structure, but its cost is very high.

Sapphire (Al_2O_3) is a good compromise and remains the most popular alternative: it is affordable and available in large high-quality wafers, has a hexagonal structure; the lattice mismatch, although not good (16%), is better than silicon and it presents good chemical and thermal stability. Its transparent nature and electrical insulator properties can also be advantages.

1.2.2 Nucleation layer

The growth of GaN on sapphire was held back for a decade by poor nucleation that was causing high dislocation densities. A major breakthrough occurred in 1986 when *Amano et al.* demonstrated that a low-temperature nucleation layer (or "buffer layer") of AlN was dramatically improving the quality of GaN-on-sapphire, if grown prior to the actual epilayer

[18]. In 1991, *Nakamura et al.* reported that a low-temperature GaN nucleation layer was further improving the epilayer quality [19].

The buffer layer grown at low temperature (450 – 550 °C) provides high nucleation centers density and promotes the lateral growth of the main GaN layer. AFM and TEM studies show that under these conditions, the Volmer-Weber growth mode is favored, which leads to 3-D islands [20,21]. In this islanding process, individual grains are made of dislocation-free cubic GaN crystals and most threading dislocations result from islands coalescence, as represented in Figure 1.4 [22].

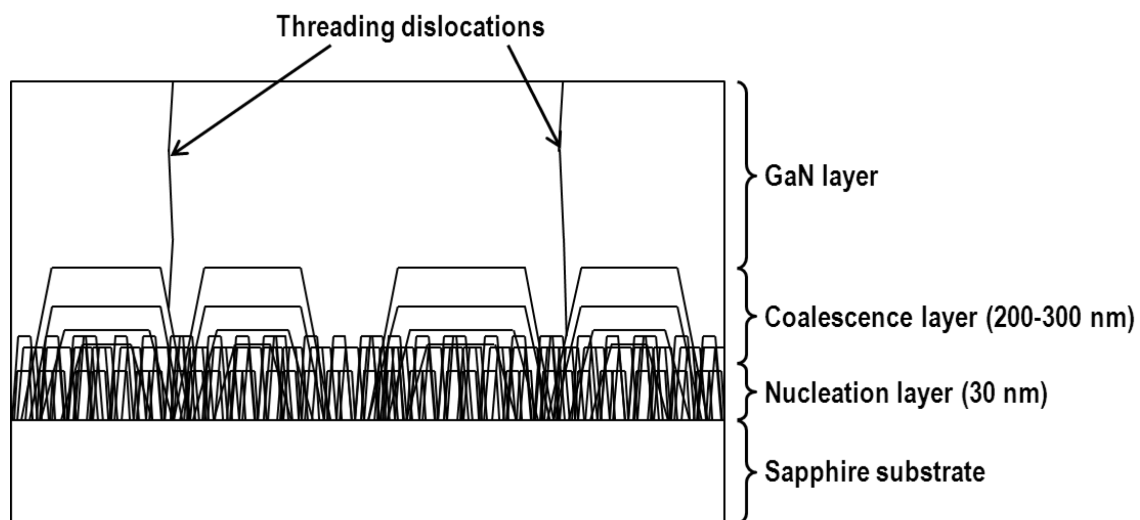

Figure 1.4: Schematic representation of a GaN film grown on a sapphire substrate

A high-temperature annealing, in which the buffer layer is slowly brought up to GaN growth temperature (~ 1050 °C) and held for a short time, causes the 3-D islands to coarsen and coalesce into a continuous layer and makes the crystal structure evolve into a mostly hexagonal configuration [23,24]. This recrystallization process, although empirically well-known and commonly used today, still remains unclear due mostly to the lack of in-situ control data. It's been observed that the thickness of the nucleation layer, its growth temperature and rate, as well as the annealing parameters all influence the quality of the GaN epilayer. An optimal point can be found to grow high-quality layers, but the mechanism by which the buffer layer evolves during the annealing is not well established.

1.2.3 Doping

Due to nitrogen vacancies and Si, O or C impurities that keep the dislocation density as high as 10^7 – 10^{10} cm^{-2}, GaN layers grown under normal conditions exhibit a high donor background carrier concentration (~ 10^{17} cm^{-3}) [12]. Understanding and controlling the residual and intentional doping levels is a key requirement for the growth of devices nonetheless and both n-type and p-type doping must be carefully studied.

Silicon is the universally-used n-type dopant (typically in silane SiH_4 precursor for MOCVD growth) as its covalent radius is close to the one of gallium, which allows it to incorporate easily into the GaN lattice by occupying the Ga sites. It has a very shallow activation energy (~ 17 meV), which enables high n-type conductivity with no change in growth parameters other than the introduction of a silicon source [25]. By varying the SiH_4 flow rate, the carrier concentration can be linearly controlled from undoped (10^{14} cm^{-3}) to 10^{19} cm^{-3}.

P-type doping on the other hand has proven to be significantly more challenging. Numerous acceptors have been studied (Li, Na, K, Be, Zn, Ca) but the most common p-type dopant for GaN is magnesium Mg. Through bis(cyclopentadienyl)magnesium precursor in MOCVD, Mg atoms are incorporated in Ga sites and become acceptors. The large activation energy of Mg in GaN (~ 160 meV) leads to a low ionization fraction, requiring the incorporation of large amounts of dopant to obtain significant doping [26]. It’s also necessary to compensate the background electron concentration, demanding even higher Mg incorporation.

Adding the dopant alone is not sufficient to obtain conductive Mg-doped layers as Mg atoms tend to combine with hydrogen to form Mg-H complexes, which get incorporated in the film and make it highly resistive. These complexes are electrically neutral and don’t contribute to the doping, and a post-growth treatment is required. *Amano et al.* first incidentally discovered in 1989 that low-energy electron beam irradiation (LEEBI) can break the Mg-H bond and activate the Mg acceptor center, dramatically enhancing the conductivity of the GaN layer [27]. Further progress was made in 1992 when *Nakamura et al.* demonstrated that thermal annealing in N_2 could achieve the same result [28].

1.2.4 InGaN growth

1.2.4.1 The InN challenge

A full understanding of the InGaN ternary alloy begins with a discussion of the InN compound. InN has not received as much attention as GaN or AlN and is far less studied and understood despite its supposedly superior optical and electrical properties. Thanks to its low electron mass especially (the lowest one for III-nitride materials), InN offers significantly higher electron saturation velocity and mobility compared to GaN (see Table 1-1). Early theoretical and experimental studies of InN reported a bandgap of ~ 1.9 eV [4], which was making other well-known compounds such as AlGaAs [29] more suitable alternatives as they can be easily grown on matched substrates. But in 2002, the first single crystal of InN was grown by *Davydov et al.* who measured a bandgap energy of 0.7 – 0.8 eV [5,30]. This made InN a candidate for new applications and helped to build up the interest for InGaN as it could be utilized for optoelectronics applications on a much broader spectral range.

The core problem with InN is the difficulty to grow high-quality crystals, mostly due to its high N_2 equilibrium vapor pressure at typical CVD deposition temperatures (~ 10^3 Torr at 800 °C), as seen in Figure 1.5 [31]. At these temperatures, this leads to InN premature dissociation on the growth surface and formation of metallic indium that will evaporate subsequently.

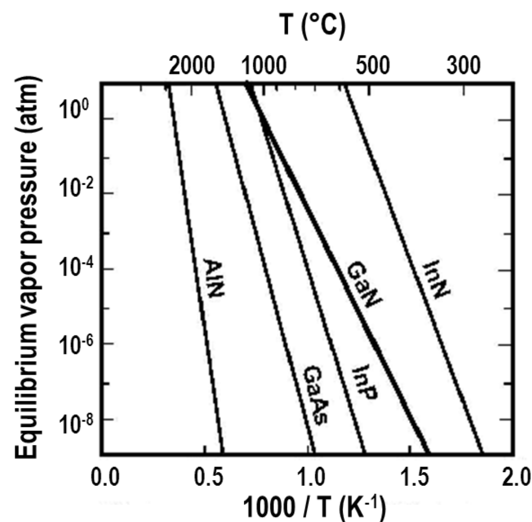

Figure 1.5: Equilibrium nitrogen vapor pressures of common III-V semiconductors

InGaN, while suffering from the same (but less pronounced) issues, is a lot easier to grow, especially at low (<10%) indium concentrations, and has been used by the optoelectronics industry for 10 years.

1.2.4.2 InGaN growth model

Bedair et al. proposed a model describing the competitive processes that occur during the InGaN growth process [32]. The model defines three possible pathways for an In adatom on the growth surface:

- the In atom can be incorporated in the solid ternary alloy
- the In atom can be incorporated as a metallic In droplet
- the In atom can be released by the growth surface (desorption)

These three pathways are concurrent processes that result in the following mass balance equation:

$$\boldsymbol{F_{in} = F_s + F_m + F_d} \qquad (1.3)$$

with F_{in}, F_s, F_m and F_d representing the fluxes of incident In, In incorporated in the solid, In forming metal droplets and In desorption from the growth surface respectively, all in atoms/cm².s, as shown in Figure 1.6.

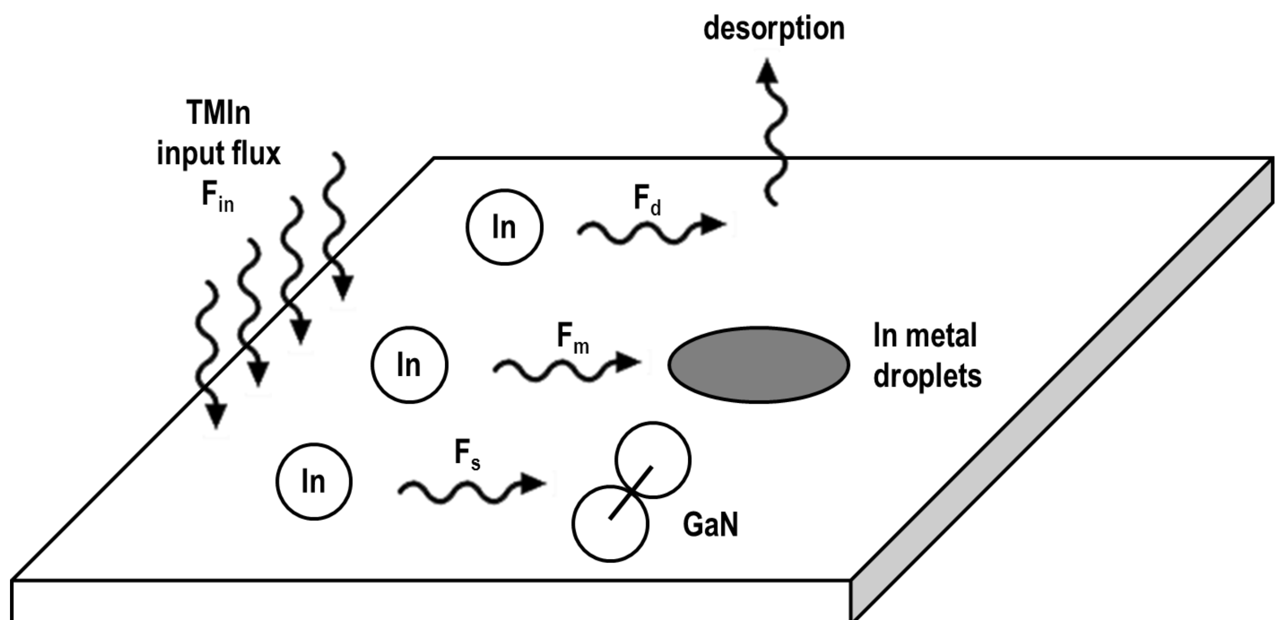

Figure 1.6: Reaction pathways for In adatoms on a growth surface

The Bedair model links F_d with the residence lifetime of an In adatom on the growth surface τ:

$$\tau = \tau_0 \cdot e^{E_d/k \cdot T} \quad (1.4)$$

where E_d is the activation energy for desorption, τ_0 is fixed for a given set of conditions and T is the growth temperature. The desorption rate can then be represented as:

$$F_d \propto e^{-E_d/k \cdot T} \quad (1.5)$$

Although E_d has not yet been determined for III-nitride materials, the weakness of the In-N bond compared to Ga-N means that F_d is much higher for In than for GaN. Experimental data showing that In content in InGaN films is inversely proportional to the growth temperature confirm this analysis, which means that very high In/Ga flux ratio is necessary to incorporate InN in InGaN crystals [33].

Lowering the growth temperature also has the effect of lowering the cracking efficiency of ammonia [32], as seen in Figure 1.7 [34], which reduces the amount of nitrogen available for bonding. This leads to the formation of small droplets of In metal that act as sinks for other In adatoms, increasing F_m and further reducing F_s.

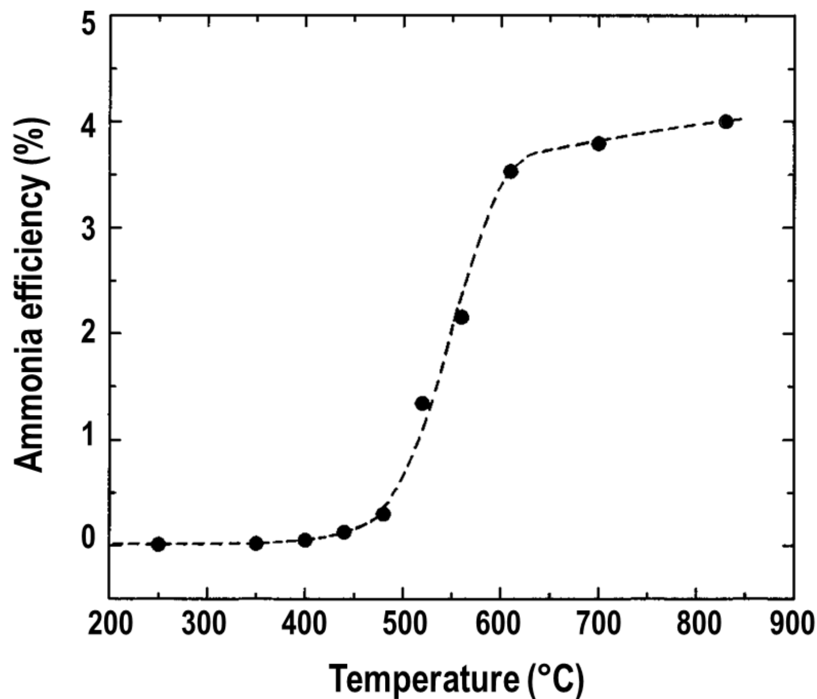

Figure 1.7: Cracking efficiency of NH3 as a function of temperature

Desorption and metal droplets formation remain the biggest challenges to grow InGaN layers, as balancing growth temperature, indium flux and nitrogen pressure proves increasingly difficult with higher In content films.

1.2.4.3 Lattice mismatch and strain

Another major issue related to the growth of InGaN is the large lattice mismatch between GaN and InN (11%, see Table 1-2) that affects the material through strain and composition inhomogeneity. The misfit strain for $In_xGa_{(1-x)}N$ can be approximated as [35]:

$$\boldsymbol{\varepsilon = -0.1065 \cdot x - 0.0003} \qquad (1.6)$$

This results in significant strains for semiconductor crystals: -1.1% at x=0.10 and -2.2% at x=0.20. This compressive strain in the a-plane is compensated by the elongation of the lattice along the c-direction in accordance with Poisson’s ratio. It increases with the thickness of the InGaN layer, until the Critical Layer Thickness (CLT) is reached (typically a few 10s of nanometers [36]), beyond which misfit dislocations form to fully or partially release the strain energy and allow the film to grow unconstrained. Monitoring the strain inside an InGaN film is important as internal strain affects the lattice parameter and, with it, fundamental values such as bandgap energy, composition and internal fields.

1.2.4.4 Inhomogeneity and phase separation

The lattice parameter difference between GaN and InN heavily affects their miscibility which favors the emergence of inhomogeneities in the local In incorporation and concentration in the alloy. Theory from *Tersoff et al.* [37] and TEM observation on InGaN/GaN multiple quantum wells structure [38] have shown the presence within the material of nanometer-scale regions with high In content, which arise from different mechanisms: strain-induced islands formation [37], spinodal decomposition [39], composition pulling effect [40] and surface segregation effect [41]. While being an inconvenience for electronic transport properties and overall efficiency of optoelectronic devices, this can also be put to good use in the case of light emission, as these quantum dot-like nanoclusters create localized minima/maxima in the conduction and valence bands, providing energy traps for charge carriers. This enhanced confinement prevents the carriers from diffusing to non-radiative recombination centers such as dislocations and therefore increase the internal quantum efficiency of the structure.

In more extreme cases though, the lattice mismatch can result in phase separation by spinodal decomposition, in which the up-hill diffusion of In atoms leads to the formation of two phases with high and low In content. *Ho et al.* [39] provided a study of the temperature dependence of the bimodal and spinodal lines of InGaN using a valence-force-field model to predict that the equilibrium solubility of In in GaN is less than 6% at 800 °C for a relaxed film, as shown in the phase diagram in Figure 1.8 (a) [42].

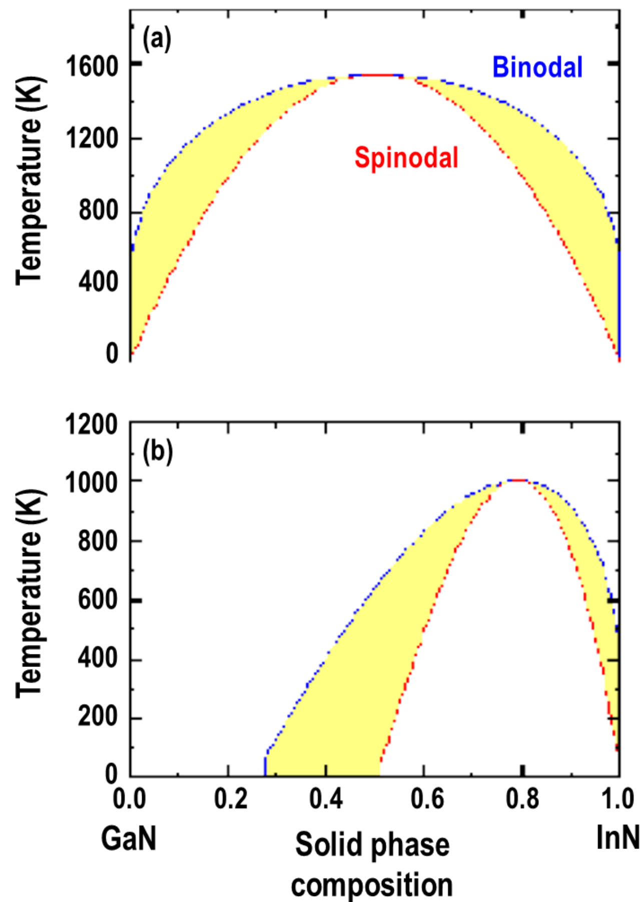

Figure 1.8: Phase diagrams of (a) relaxed and (b) strained $In_xGa_{1-x}N$ films

Points above the binodal are thermodynamically stable and the alloy can be grown. Below the spinodal curve, the material is unstable and will transform homogeneously via spinodal decomposition into two phases whose composition can be predicted by the intersection of the isotherm and the binodal curve. Between the two curves, a metastable state of the material can exist and phase separation will only occur if triggered by discontinuities [43] or InN precipitation [44, 45].

It is important to understand the role of strain in phase separation. Cahn's spinodal decomposition theory [46] mentions that a spinodal phase transformation involves three energy terms: the free energy which is the driving force of the spinodal decomposition while the gradient energy (due to composition fluctuations) and strain energy work to stabilize the material. A strained film can therefore sustain higher In content and be grown at lower temperature, explaining for example the higher stability of GaN/InGaN quantum-well structures. This can be seen in Figure 1.8 (b) [42].

1.2.4.5 Polarization

Wurtzite III-nitride materials meet the requirements for polarization due to highly ionic bonds resulting from the large electronegativity difference between group III elements (Ga, Al, In) and N and the wurtzite crystal structure that lacks inversion symmetry. III-nitrides also display piezoelectricity as they can convert mechanical stress and strain into an electric field [47]. The high strain values in InGaN/GaN structures thus induce a significant piezoelectric field along the (0001) direction that leads to the bending of the conduction and valence bands and is responsible for the quantum-confined Stark effect [48] that occurs in quantum wells when the energy gap between the two bands is reduced, as illustrated in Figure 1.9 [49].

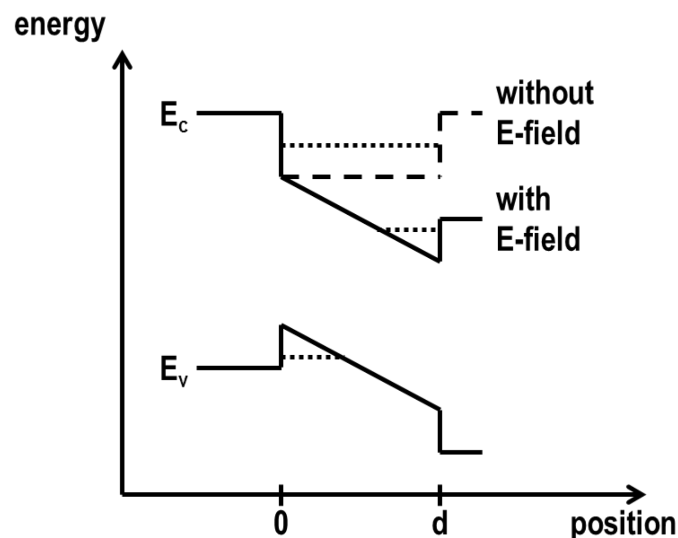

Figure 1.9: Band-bending in a quantum well due to the piezoelectric field

When the band bending takes place, the minima of the two bands shift to a lower energy level. The maximum of the valence band, however, remains at the same energy, which lowers

the effective bandgap of the material and results in a redshift. While this effect is extremely interesting and useful to build structures that achieve longer emission wavelength than otherwise possible (especially given the difficulty of growing high In content InGaN), it introduces two drawbacks: the broadening of the emission spectrum, and, more importantly, the reduction of the internal quantum efficiency due to the decreased overlap of the electron and hole wavefunctions.

1.3 Optoelectronics applications of GaN and InGaN

The late discovery of the role of nucleation layer and p-type doping delayed for a long time the rise of GaN-based industrial devices, but as soon as these were established, blue and green light-emitting diodes (LEDs) and laser diodes (LDs) started to appear that lead to the commercialization of the first candela-class GaN-based blue LEDs in 1993, shortly followed by yellow and amber LEDs based on InGaN [50]. In 1996 the first white LED was demonstrated, combining a blue LED with phosphor coating [51]. More recently, phosphor free white LEDs have been reported [52]. Solid-state lighting has been for a long time a driving force to keep working on GaN-based LEDs as it presents a number of potential applications ranging from full color electroluminescent displays to automotive or general lighting, replacing incandescent light bulbs and fluorescent lamps for energy savings in a global market that will soon reach US$ 100 billion [53]. To further increase the efficiency of the GaN-based devices, researchers now work on incorporating quantum dots with various In content inside InGaN layers to directly emit white light.

The first InGaN LD with continuous wave operation was built in 1996 [54] and the first commercial room-temperature continuous-wave blue-violet laser diode reached the market in 2001 and had massively spread through high-density optical disk video recording applications under the Blu-ray disc technology.

Other applications of III-nitrides include metal-oxide-semiconductor and metal-semiconductor field-effect transistors (MOSFETs and MESFETs) [55] and more recently high electron mobility transistors (HEMTs) [56], high frequency and high power amplifiers. The superior electrical properties of InN also open opportunities in high-speed electronics.

A further area of research is visible-blind and solar-blind ultraviolet (UV) photodetectors used in space-to-space communication, UV astronomy, chemical and biological agent detection, flame detection or engine and furnace monitoring. After the first report of GaN UV photodetector in 1992 [57], GaN p-n junction photodiode in 1995 [58] and metal-semiconductor-metal GaN photodetectors [59], the discovery of the lower-than-expected bandgap energy of InN triggered a movement to produce high-efficiency solar cells as the solar spectrum can be reproduced with an InGaN-multiple layer arrangement [60]. Still in the energy harvesting field, photo-electrochemical cells based on GaN and InGaN were used for H2 generation by splitting water via sunlight [61].

GaN is also a biocompatible material [62], which could lead to biomedical electronic applications.

1.4 Motivations and objectives of the thesis

InGaN, because of its tunable properties according to the In content, can be a very versatile material system for many applications. But the fundamental structural, optical and electrical properties of the alloy remain mostly unstudied. In spite of the successful demonstration and commercialization of a number of devices including LEDs, LDs and photodetectors, a complete understanding of InGaN is still an absolute necessity to keep developing the knowledge of the compound and overcome the challenges that come with its growth.

The main objective of this thesis project is to investigate in detail the structure and optical properties of InGaN thin films grown on GaN-on-sapphire by MOCVD with In content of up to 20% and thus increase the global knowledge and understanding of the material.

Chapter 2 will describe the growth process that was used and how the microstructure of the subsequent films is characterized. Chapter 3 and 4 will focus on the optical characterization of the InGaN thin films in two frequency ranges of interest for further applications of InGaN materials: the UV/visible range and the terahertz range respectively. Finally, chapter 5 will detail the design process, the fabrication and the characterization of an InGaN-based terahertz photodiode.

References

[1] C. Stampfl and C.G. Van de Walle, "Density-functional calculations for III-V nitrides using the local-density approximation and the generalized gradient approximation", *Phys. Rev. B* **59**(8), 5521 (1999)

[2] E.F. Schubert, *Light Emitting Diodes, 2nd Edition*, Fig. 12.12, Cambridge University Press, Cambridge (2006)

[3] V. Bougrov, M.E. Levinshtein, S.L. Rumyantsev and A. Zubrilov, *Properties of Advanced Semiconductor Materials GaN, AlN, InN, BN, SiC, SiGe*, p.1-30, John Wiley & Sons, Inc., New York (2001)

[4] T.L. Tansley and C.P. Foley, "Optical band gap of indium nitride", *J. Appl. Phys.* **59**, 3241 (1986)

[5] V.Yu. Davydov, A.A. Klochikhin, R.P. Seisyan, V.V. Emtsev, S.V. Ivanov, F. Bechstedt, J. Furthmuller, H. Harima, A.V. Mudryi, J. Aderhold, O. Semchinova and J. Graul, "Absorption and Emission of Hexagonal InN. Evidence of Narrow Fundamental Band Gap", *Phys. Stat. Solidi (b)* **229**, R1-R3 (2002)

[6] T. Matsuoka, H. Okamato, M. Nakao, H. Harima, and E. Kurimoto, "Optical bandgap energy of wurtzite InN", *Appl. Phys. Lett.* **81**, 1246 (2002)

[7] F. Bechstedt, J. Furthmüller, M. Ferhat, L. K. Teles, L. M. R. Scolfaro, J. R. Leite, V. Yu. Davydov, O. Ambacher and R. Goldhahn, "Energy gap and optical properties of $In_xGa_{1-x}N$", *Phys. Stat. Sol. (a)* **195**, 628-633 (2003)

[8] M. Anani, H. Abid, Z. Chama, C. Mathieu, A. Sayede, B. Khelifa, "$In_xGa_{1-x}N$ refractive index calculations", *Microelectron. J.* **38**, 262-266 (2007)

[9] I. Vurgaftman and J. R. Meyer., "Band parameters for nitrogen-containing semiconductors", *J. Appl. Phys.* **94**, 3675-3696 (2003)

[10] S. Strite and H. Morkoc, "GaN, AlN, and InN: A review", *J. Vac. Sci. Technol. B* **10** (4), 1237-1266 (1992)

[11] F. Fischer and F. Schroter, "Über neue Metall-Stickstoff-Verbindungen und ihre Stabilität an der Hand des periodischen Systems", *Berichte der Deutschen Chemischen Gesellschaft* **43**, 1465-1479 (1910)

[12] V.C. Johnson, J.B. Parsons and M.C. Crew, "Nitrogen compounds of gallium", *J. Phys. Chem.* **36**, 2588 (1932)

[13] H. P. Maruska and J. J. Tietjen, "The preparation and properties of vapor-deposited single-crystal-line GaN", *Appl. Phys. Lett.* **15**, 327 (1969)

[14] H. M. Manasevit, F. M. Erdmann and W. I. Simpson, "The Use of Metalorganics in the Preparation of Semiconductor Materials", *J. Electrochem. Soc.* **118**, 1864 (1971)

[15] I. Akasaki and I. Hayashi, "Research on blue emitting devices", *Ind. Sci. Technol.* **17**, 48 (1976)

[16] S. Nakamura, S. Pearton and G. Fasol, *The Blue Laser Diode: The Complete Story*, Ch. 6.3, Springer, Berlin (2000)

[17] D.R. Lide (Editor-in-Chief), *CRC Handbook of Chemistry and Physics, 78th Edition*, CRC Press, Boca Raton, New York (1997)

[18] H. Amano, N. Sawaki, I. Akasaki and Y. Toyoda, "Metalorganic vapor phase epitaxial growth of a high quality GaN film using an AlN buffer layer", *Appl. Phys. Lett.* **48**, 353 (1986)

[19] S. Nakamura, "GaN Growth Using GaN Buffer Layer", *Jpn. J. Appl. Phys.* **30**, L1705 (1991)

[20] X.H. Wu, D. Kapolnek, E.J. Tarsa, B. Heying, S. Keller, B.P. Keller, U.K. Mishra, S.P. DenBaars and J.S. Speck, "Nucleation layer evolution in metal-organic chemical vapor deposition grown GaN", *Appl. Phys. Lett.* **68**, 1371 (1996)

[21] S. D. Hersee, J. C. Ramer and K. J. Malloy, "The microstructure of MOCVD GaN on sapphire", *MRS Bull.* **22**, 45-51 (1997)

[22] K. Hiramatsu, S. Itoh, H. Amano, I. Akasaki, N. Kuwano, T. Shiraishi, and K. Oki, "Growth mechanism of GaN grown on sapphire with AlN buffer layer by MOVPE", *J. Cryst. Growth* **115**, 628-633 (1991)

[23] L. Sugiura, K. Itaya, J. Nishio, H. Fujimoto and Y. Kokubun, "Effects of thermal treatment of low-temperature GaN buffer layers on the quality of subsequent GaN layers", *J. Appl. Phys.* **82**, 4877 (1997)

[24] I. Akasaki and H. Amano, "Recent progress of crystal growth, conductivity control and light emitters of group III nitride semiconductors", *Tech Dig. Int. Electron Devices Meet.* **96**, 231-237 (1996)

[25] J.K. Sheu and G.C. Chi, "The doping process and dopant characteristics of GaN", *J. Phys.: Condens. Matt.* **14**, R657 (2002)

[26] C. Stampfl, J. Neugebauer and C.G. Van de Walle, "Doping of $Al_xGa_{1-x}N$ alloys", *Mater. Sci. Eng. B* **59**, 253-257 (1999)

[27] H. Amano, M. Kito, K. Hiramatsu and I. Akasaki, "P-Type Conduction in Mg-Doped GaN Treated with Low-Energy Electron Beam Irradiation (LEEBI)", *Jpn. J. Appl. Phys.* **28**, L2112-L2114 (1989)

[28] S. Nakamura, T. Mukai, M. Senoh and N. Iwasa, "Thermal Annealing Effects on P-Type Mg-Doped GaN Films", *Jpn. J. Appl. Phys.* **31**, L139-L142 (1992)

[29] A. Adachi, "GaAs, AlAs, and $Al_xGa_{1-x}As$: Material parameters for use in research and device applications", *J. Appl. Phys.* **51**, R1 (1985)

[30] J. Wu, W. Walukiewicz, K.M. Yu, J.W. Ager, E.E. Haller, Hai Lu, W.J. Schaff, Y. Saito and Y. Nanishi, "Unusual properties of the fundamental band gap of InN", *Appl. Phys. Lett.* **80**, 3967 (2002)

[31] T. Matsuoka, H. Tanaka, T.Sasaki and A. Katsui, "Wide-gap semiconductor (In,Ga)N." *Inst. Phys. Conf. Ser. No 106: International Symposium on GaAs and Related Compounds*, 141 (1989)

[32] S.M. Bedair, F.G. McIntosh, J.C. Roberts, E.L. Piner, K.S. Boutros, N.A. El-Masry, "Growth and characterization of In-based nitride compounds", *J. Cryst. Growth* **178**, 32-44 (1997)

[33] T. Matsuoka, N. Yoshimoto, T. Sakaki and A. Katsui, "Wide-Gap Semiconductor InGaN and InGaAIN Grown by MOVPE", *J. Electron. Mat.* **21**, 157-163 (1992)

[34] T. Mastuoka, T. Sasaki and A. Katsui, "Growth and properties of a wide gap semiconductor InGaN", *Optoelectronics Tokyo* **5**, 53-64 (1990)

[35] P.T. Barletta, E.A. Berkman, B.F. Moody, N.A. El-Masry, A.M. Emara, M.J. Reed and S. M. Bedair, *Appl. Phys. Lett.* **90**, 151109 (2007)

[36] M. Leyer, J. Stellmach, C. Meissner, M. Pristovsek and M.Kneissl, "The critical thickness of InGaN on (0001) GaN", *J. Cryst. Growth* **310**, 4913-4915 (2008)

[37] J. Tersoff, "Enhanced nucleation and enrichment of strained-alloy quantum dots", *Phys. Rev. Lett.* **81**, 3183-3186 (1998)

[38] Y.S. Lin, K.J. Ma, C. Hsu, S.W. Feng, Y.C. Cheng, C.C. Liao, C.C. Yang, C.C. Chou, C.M. Lee and J.I. Chyi, "Dependence of composition fluctuation on indium content in InGaN/GaN multiple quantum wells" *Appl. Phys. Lett.* **77**, 2988 (2000)

[39] I.H. Ho and G.B. Stringfellow, "Solid phase immiscibility in GaInN." *Appl. Phys. Lett.* **69**, 2701 (1996)

[40] K. Hiramatsu, Y. Kawaguchi, M. Shimizu, N. Sawaki, T. Zheleva, R.F. Davis, H. Tsuda, W. Taki, N. Kuwano, K. Oki, "The composition pulling effect in MOVPE grown InGaN on GaN and AlGaN and its TEM characterization", *MRS Internet J. Nitride Semicond. Res.* **2**, 6 (1997)

[41] N. Grandjean, J. Massies, S. Dalmasso, P. Vennegues, L. Siozade and L. Hirsch, "GaInN/GaN multiple-quantum-well light-emitting diodes grown by molecular beam epitaxy", *Appl. Phys. Lett.* **74**, 3616 (1999)

[42] S.Y. Karpov, "Suppression of phase separation in InGaN due to elastic strain", *MRS Internet J. Nitride Semicond. Res.* **3**, 16 (1998)

[43] T.D. Moustakas, "Growth of wide-bandgap nitride semiconductors by MBE" *Gallium-Nitride-based Technologies*, p.1, SPIE Optical Engineering Press, Bellingham (2002)

[44] F.A. Ponce, S. Srinivasan, A. Bell, L. Geng, R. Liu, M. Stevens, J. Cai, H. Omiya, H. Marui and S. Tanaka, "Microstructure and electronic properties of InGaN alloys", *Phys. Stat. Sol. (b)* **240**, 273 (2003)

[45] M.K. Behbehani, E.L. Piner, S.X. Liu, N.A. El-Masry and S.M. Bedair, "Phase separation and ordering coexisting in $In_xGa_{1-x}N$ grown by metal organic chemical vapor deposition", *Appl. Phys. Lett.* **75**, 2202 (1999)

[46] J.W. Cahn, "Spinodal decomposition", *Trans. of the Metall. Soc. Of AIME* **242**, 166 (1968)

[47] E.T. Yu, X.Z. Dang, P.M. Asbeck, S.S. Lau and G.J. Sullivan, "Spontaneous and piezoelectric polarization effects in III-V nitride heterostructures", *J. Vac. Sci. Tech. B* **17**, 1742 (1999)

[48] D.A.B. Miller, D.S. Chemla, T.C. Damen, A.C Gossard, W. Wiegmann, T.H. Wood and C.A. Burrus, "Band-edge electroabsorption in quantum well structures: the quantum-confined stark effect", *Phys. Rev. Lett.* **53**, 2173 (1984)

[49] M.E. Aumer, S.F. LeBoeuf, B.F. Moody, and S.M. Bedair, "Strain-induced piezoelectric field effects on light emission energy and intensity from AlInGaN/InGaN quantum wells", *Appl. Phys. Lett.* **79**, 3803 (2001)

[50] S. Nakamura, M. Senoh, N. Iwasa and S. I. Nagahama, "High-Brightness InGaN Blue, Green and Yellow Light-Emitting Diodes with Quantum Well Structures", *Jpn. J. Appl. Phys.* **34**, L797-L799 (1995)

[51] Y. Sato, N. Takahashi and S. Sato, "Full-Color Fluorescent Display Devices Using a Near-UV Light-Emitting Diode", *Jpn. J. Appl. Phys.* **35**, L838 (1996)

[52] C.B. Soh, W. Liu, J.H. Teng, S.Y. Chow, S.S. Ang and S.J. Chua, "Cool white III-nitride light emitting diodes based on phosphor-free indium-rich InGaN nanostructures", *Appl. Phys. Lett.* **92**, 261909 (2008)

[53] T. Baumgartner, F. Wunderlich, D. Wee, A. Jaunich, T. Sato, U. Erxleben, G.Bundy, R. Bundsgaard, *Lighting the way: Perspectives on the global lighting market*, McKinsey & Company, Inc., New York (2011)

[54] S. Nakamura, M. Senoh, S. I. Nagahama, N. Iwasa, T. Yamada, T. Matsushita, Y. Sugimoto and H. Kiyoku,, "Continuous-wave operation of InGaN multi-quantum-well-structure laser diodes at 233 K" *Appl. Phys. Lett.* **69**, 3034 (1996)

[55] M. Asif Khan, J.N. Kuznia, A.R. Bhattarai, D.T. Olson, "Metal semiconductor field effect transistor based on single crystal GaN", *Appl. Phys. Lett.* **62**, 1786 (1993)

[56] D. Yuvaraj, A. Chakraborty, L. McCarthy, S. Keller, S. DenBaars, U. Mishra, "High Breakdown Voltage Achieved on AlGaN/GaN HEMTs With Integrated Slant Field Plates", *IEEE Electron Device Letters* **27**, 713(2006)

[57] M. Khan, J. N. Kuznia, D. T. Olson, J. M. Van Hove, M. Blasingame and L. F. Reitz, "High-responsivity photoconductive ultraviolet sensors based on insulating single-crystal GaN epilayers", *Appl. Phys. Lett.* **60**, 2917 (1992)

[58] X. Zhang, P. Kung, D. Walker, J. Piotrowski, A. Rogalski, A. Saxler and M. Razeghi, "Kinetics of photoconductivity in n-type GaN photodetector", *Appl. Phys. Lett.* **67**, 3792 (1995)

[59] D. Walker, E. Monroy, P. Kung, J. Wu, M. Hamilon, F. J. Sanchez, J. Diaz and M. Razighi, "Optical poling and its application in optical storage of a polyimide film with high glass transition temperature", *Appl. Phys. Lett.* **74**, 762 (1998)

[60] J. Wu, W. Walukiewicz, W. Shan, K. M. Yu, J. W. Ager, III, E. E. Haller, Hai Lu, and William J. Schaff, "Effects of the narrow band gap on the properties of InN", *Phys. Rev. B* **66**, 201403 (2002)

[61] R.M. Sheetz; E. Richter, A.N. Andriotis, S. Lisenkov, C. Pendyala, M.K. Sunkara, M. Menon, "Visible-light absorption and large band-gap bowing of $GaN_{1-x}Sb_x$ from first principles", *Phys. Rev. B* **84**, 075304–1 (2011)

[62] S.A. Jewett, M.S. Makowski, B. Andrews, M.J. Manfra, A. Ivanisevic, "Gallium nitride is biocompatible and non-toxic before and after functionalization with peptides", *Acta Biomaterialia* **8**, 728-733 (2012)

Chapter 2
Growth and characterization of InGaN thin films

2. CHAPTER 2 GROWTH AND CHARACTERIZATION OF INGAN THIN FILMS........................25

2.1 GROWTH OF INGAN THIN FILMS 26

2.1.1 Introduction to MOCVD 26

2.1.2 Experimental InGaN growth process 27

2.1.2.1 GaN growth.. 27

2.1.2.2 InGaN growth 29

2.2 STRUCTURE AND COMPOSITION CHARACTERIZATION OF INGAN THIN FILMS 33

2.2.1 InGaN monolayer thin films characterization.. 33

2.2.1.1 Microscopy 33

2.2.1.2 X-ray diffraction 36

2.2.1.3 Photoluminescence... 39

2.2.1.4. Secondary ion-mass spectrometry... 41

2.2.1.5 Summary 43

2.2.2 InGaN multilayer thin films characterization 44

2.2.2.1 Microscopy 44

2.2.2.2 X-ray diffraction 46

2.2.2.3 Photoluminescence... 47

2.2.2.4 Secondary ion-mass spectrometry... 48

2.2.2.5 Summary 50

2.2.3 Structures and compositions summary.. 51

REFERENCES 52

2.1 Growth of InGaN thin films

The first step in the experimental study of InGaN-based materials is the growth of high-quality nominally-undoped GaN and InGaN layers. Many methods have been employed to grow III-nitride thin films. With the development of crystal growth technology, each new technique has been applied to the III-nitrides growth and today, almost all the high-quality III-nitride material are reportedly grown using one of two modern techniques: molecular beam epitaxy (MBE) and chemical vapor deposition (CVD).

This dissertation utilizes metalorganic chemical vapor deposition (MOCVD) for the epitaxial growth of III-nitride films.

2.1.1 Introduction to MOCVD

The groundwork for MOCVD was laid by *Manasevit et al.* in 1968 [1]. Alkyls of the group III metals (hence the metalorganic terminology) and ammonia are used as precursor species. Their diluted vapors are transported at near-room temperature to the heated surface of the substrate where a pyrolysis reaction occurs that can be generalized as:

$$R_3M + NH_3 \rightarrow MN + 3RH \quad (2.1)$$

M represents the group III metal, either indium or gallium in our case, and R is the organic radical, typically an alkyl. The metalorganic precursors used for GaN and InN deposition are trimethylgallium (TMGa) and trimethylindium (TMIn) respectively, which translates equation (2.1) into:

$$(CH_3)_3Ga + NH_3 \rightarrow GaN + 3CH_4 \quad (2.2)$$

$$(CH_3)_3In + NH_3 \rightarrow InN + 3CH_4 \quad (2.3)$$

In the case of $In_xGa_{1-x}N$, the alloy composition x is determined by the relative speed of the two reactions, which depends on a number of factors including gaseous diffusion, thermodynamics, intermediate steps and gas dynamics.

Our samples were grown at the Institute of Materials Research and Engineering (IMRE) on the EMCORE Discovery 180 vertical MOCVD reactor pictured on Figure 2.1. The system is dedicated to the epitaxial growth of group-III nitride materials. It has a vertical stain-less steel

chamber in which the deposition can take place from room temperature to 1100 °C and GaN, InGaN and AlGaN thin films and multiple layer structures with n-type or p-type doping can be grown. Temperature is monitored and controlled inside the chamber via thermal couples and pyrometers. In-situ monitoring of the growth process is provided using spectroscopic reflectance. [2,3]

Figure 2.1: IMRE MOCVD reactor

2.1.2 Experimental InGaN growth process

2.1.2.1 GaN growth

The GaN growth is performed on 330 µm thick, 2 inch diameter, (0001) sapphire substrates. The wafers are epi-ready so require no cleaning process and are chamber-ready. A non-intentionally doped (i-GaN) or n-doped (n-GaN) GaN layer will be grown on all the substrates, either to obtain a GaN sample or as a GaN-on-sapphire template to later grow InGaN and InN layers.

Table 2.1 lists the detailed step-by-step growth recipe that was found experimentally to give the highest quality GaN. It follows the generally accepted recipe for GaN growth [4] and is composed of the following steps:

(i) Substrate cleaning and restructuring: the substrate is baked at 1080 °C under H_2 overpressure to desorb water and hydrocarbons, and to deplete O_2 from the Al_2O_3 and obtain an aluminum-rich surface.

(ii) Nucleation layer: TMGa and NH_3 are introduced into the chamber at 530 °C to deposit a 35 nm-thick buffer layer. At this low temperature, nucleation rate is high and small islands of cubic GaN are formed, as described in paragraph 1.2.2.

(iii) Buffer anneal: the wafer is heated up to 1050 °C and annealed for 30 seconds for GaN islands to coarsen and coalesce. This operation also initiates the transformation of the cubic structure to a hexagonal one.

(iv) Coalescence layer: to accommodate the stress between sapphire and GaN and thus further improve the quality of the subsequent GaN thin film, an extra 200 nm-thick layer of GaN is grown at 950 °C.

(v) GaN epilayer: Finally, the bulk GaN layer can be grown at 1030 °C at a V/III ratio of 250. A thickness of 2.2 to 2.3 µm is achieved in 45 to 50 minutes. To obtain n-type GaN, a silane (SiH_4) flux is added.

Step	**Temperature [°C]**	**Pressure [torr]**	**TMGa flux [sccm]**	**NH3 flux [slm]**	**H2 flux [slm]**	**Time [s]**
Clean/Bake	1080	500	-	-	20	300
Buffer layer	530	500	20	30	20	240
Buffer anneal	1050	500	-	-	20	30
Coalescence layer	950	500	100	25	20	280
Bulk GaN growth	1030	500	100	25	20	-

Table 2-1: Experimental conditions of the GaN growth steps

This process is represented graphically in Figure 2.2. The time between each step depends on the thermal inertia of the reactor chamber and may not be accurately depicted.

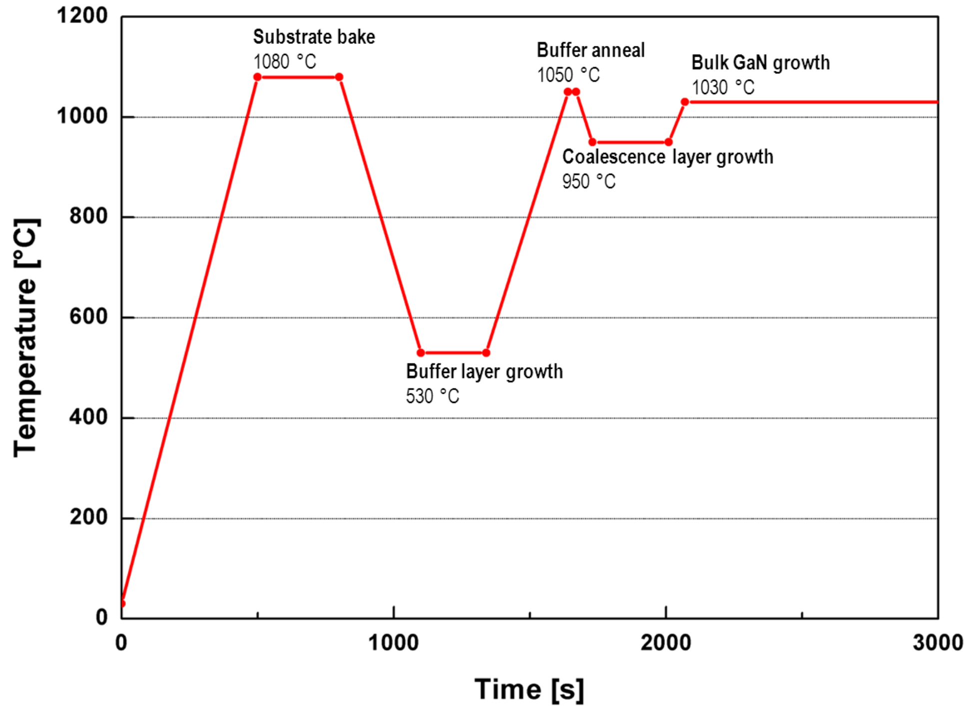

Figure 2.2: Temperature profile of the GaN growth process

Four GaN samples were grown using this procedure, as described in Table 2-2. Several samples with the GaN-0 properties were grown to be later used as a template for InGaN growth. GaN-1, GaN-2 and GaN-3 are thicker and cover a range of carrier concentrations, as determined by Hall effect measurements.

Sample name	**Estimated GaN thickness [μm]**	**Carrier concentration [cm^{-3}]**
GaN-0	2	3.1×10^{17}
GaN-1	4	2.5×10^{17}
GaN-2	6	1.8×10^{18}
GaN-3	4	3.3×10^{18}

Table 2-2: List of the studied GaN samples

2.1.2.2 InGaN growth

InGaN films are grown on the GaN-on-sapphire template described in the previous paragraph. The goal of this study is to obtain and characterize a set of InGaN thin films with

varying In fractions. As discussed in section 1.2.4.2, increasing the TMIn flux to increase the final In content of the film is not enough. Studies have actually shown that the InGaN alloy composition is mostly dependent on the growth temperature. [5,6]

The Bedair model [7] shows that at high temperature, the desorption flux is the controlling factor and increasing the incident In flux only results in more desorption. In contrast, reducing the growth temperature is an effective way to increase the incorporation of In in the compound. Altogether, it's important to remember that the growth temperature, not the In/Ga adatoms ratio, is the primary parameter to control the indium content of a layer.

The conditions to grow InGaN films differ from the ones used for GaN in a number of ways:

- TMIn is introduced in the chamber as the indium source. It is important to maximize the In/Ga flux ratio to oppose the effect of the weaker In-N bond compared to the Ga-N one. Therefore, TMIn flux is chosen as high as possible and TMGa is lowered significantly.
- The growth temperature is dropped to the 700 – 800 °C range in order to incorporate a higher amount of In in the alloy.
- H_2 is replaced with N_2 in the chamber as it has been demonstrated that hydrogen has a negative impact on In incorporation. [8]
- To grow an InN layer, the temperature is further decreased to 595 °C and the TMGa inlet is closed. Growth of InN layer directly on GaN is very difficult because of their large miscibility gap. Inserting a 50 nm-thin $In_{0.3}Ga_{0.7}N$ interlayer helps the nucleation of InN as it reduces the lattice mismatch. [9]

These conditions are tabulated in Table 2-3:

Step	**Temperature [°C]**	**Pressure [torr]**	**TMGa flux [sccm]**	**TMIn flux [sccm]**	**NH3 flux [slm]**	**N2 flux [slm]**
Bulk InGaN growth	700 - 800	150	3	400	20	6
Bulk InN growth	595	150	-	400	12	6

Table 2-3: Experimental conditions of the InGaN growth

Using these parameters, three InGaN samples were grown at varying temperatures, as well as one InN sample with its $In_{0.3}Ga_{0.7}N$ 50 nm-thick transition layer. They are presented in Table 2-4 and Figure 2.3:

Sample name	Top layer thickness [nm]	Intended In fraction [ ]	Carrier concentration [cm^{-3}]
InGaN-1	200-300	0.01	5.1×10^{17}
InGaN-2	200-300	0.1	6.4×10^{17}
InGaN-3	200-300	0.3	6.5×10^{17}
InN	300	1	4.4×10^{18}

Table 2-4: List of the studied InGaN samples

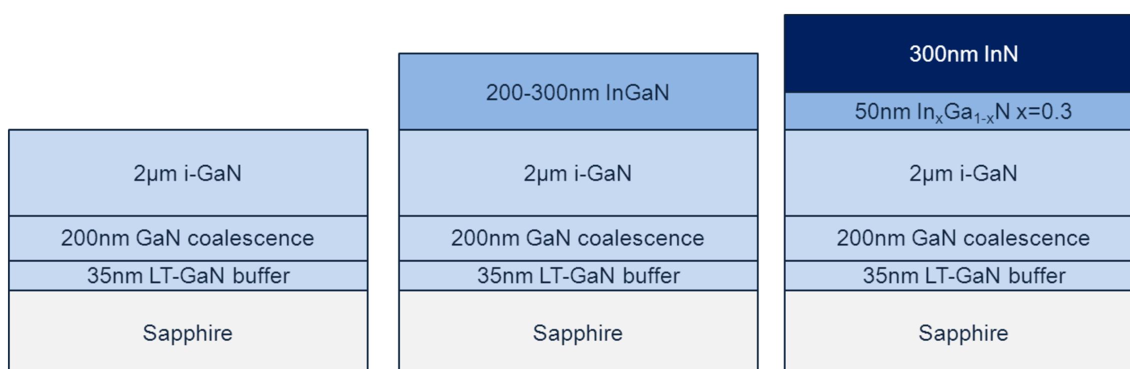

Figure 2.3: Structures of the GaN template (left) InGaN samples (middle) and InN sample (right)

An important aspect of MOCVD is its capability to grow III-N alloys in a single apparatus, in any sequence during a single deposition experiment, creating heterostructures with novel physical properties (e. g. different doping levels for junctions or different material compositions for multi-quantum-well structures). It means that we can grow multilayered (ML) InGaN/GaN structures. This is very interesting as we have established in paragraph 1.2.4.4 that a strained film can accommodate a higher In fraction than a relaxed one (see Figure 1.8 (b)). By alternating thin layers of GaN and InGaN, we are therefore able to grow InGaN films with higher In content and lower dislocation concentration densities (typically from 10^9 cm^{-2} to 10^7 cm^{-2}) [10-11].

Three samples were grown with several InGaN layers separated by 10 nm-thick GaN interlayers and different In fractions:

Sample name	**Structure**	**Intended In fraction [ ]**
InGaN-1-ML	3 * 130 nm	0.3
InGaN-2-ML	6 * 60 nm	0.3
InGaN-3-ML	6 * 60 nm	0.2

Table 2-5: List of the studied InGaN multilayer samples

Figure 2.4 represents the two structures used for the samples. Two 10 nm-thick layers with lower In fractions are grown as transition layers between the GaN-on-sapphire template and the first InGaN layer.

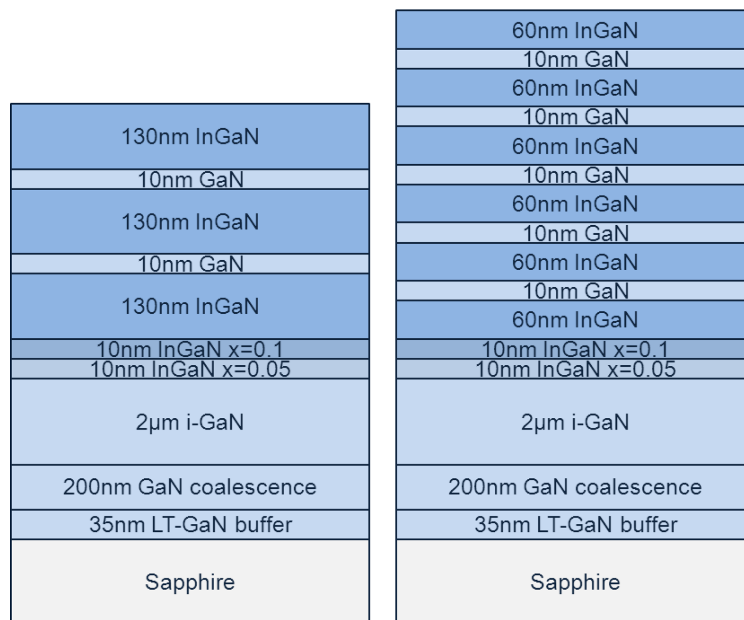

Figure 2.4: Structures of the studied InGaN multilayer samples

2.2 Structure and composition characterization of InGaN thin films

Due to the difficulties of growing III-nitrides, a thorough study of the grown layers is necessary. Several studies of the InGaN growth by MOCVD have focused on specific aspects such as surface morphology [12,13] or the rate and fraction of indium incorporation as a function of the temperature [14,15], TMI flux [16] or H_2 flux [8], V/III ratio [17] and growth rate [7].

High-resolution X-ray diffraction (XRD) [7,12,15,18], photoluminescence (PL) [7,16,19], Rutherford backscattering spectrometry (RBS) [12], X-ray photoelectron spectroscopy (XPS) [12] and secondary ion-mass spectrometry (SIMS) [20,21] have been employed in these studies. The accurate determination of the $In_xGa_{1-x}N$ composition is usually not straightforward, as compositional inhomogeneity and internal strain can cause discrepancies between the measures and the actual values of the In fraction.

2.2.1 InGaN monolayer thin films characterization

2.2.1.1 Microscopy

The layer structure can be directly observed using cross-sectional scanning electron microscopy (SEM) and transmission electron microscopy (TEM). Figure 2.5 and 2.6 show respectively SEM and TEM pictures of the InGaN and InN samples. The thicknesses of the GaN templates and InGaN layers are measured and reported in Table 2-6.

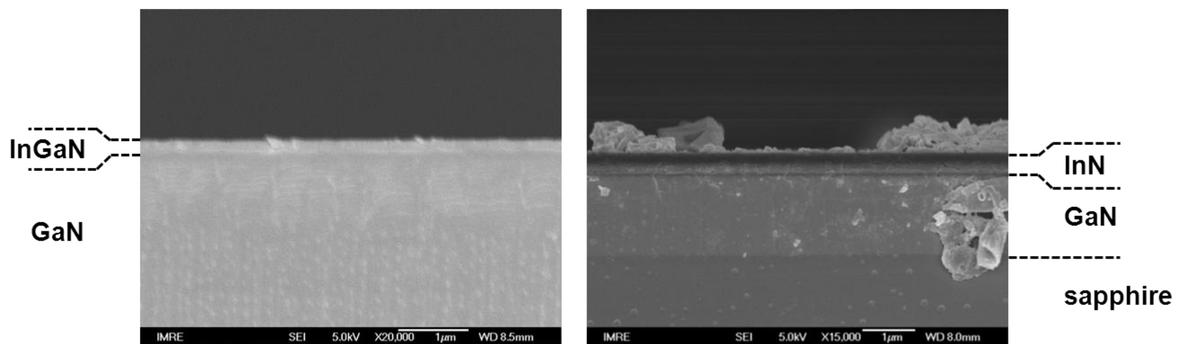

Figure 2.5: SEM images of samples InGaN-1 (left) and InN (right)

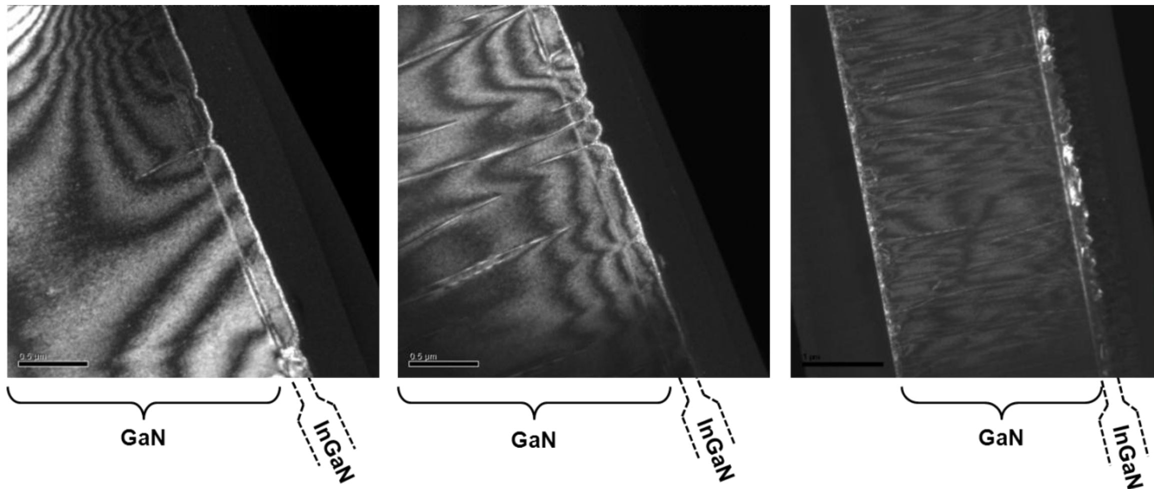

Figure 2.6: TEM images of samples InGaN-1 (left), InGaN-2 (center) and InGaN-3 (right)

Sample name	GaN layer thickness [µm]	Top layer thickness [nm]
InGaN-1	2.4	180
InGaN-2	2.2	190
InGaN-3	2.2	250
InN	1.6	350

Table 2-6: Layer thicknesses of the InGaN monolayer samples

The TEM pictures provide further information on the internal structure of the InGaN layers by showing threading dislocations and v-pits. The v-pits are hexagonal pits often associated with the growth of InGaN films by MOCVD. They have been identified and characterized extensively on both thin films and single and multiple quantum well structures using TEM [22-28] and atomic force microscopy (AFM) [23,26]. The defects present a six-sided inverted pyramid with a measured inclination of 60° which suggests that the sidewalls are inclined to the {1 0 -1 1} plane, as represented in Figure 2.7 [29]. Their average diameter increases with thickness and has been found to be greater than 50 nm for bulk layers thicker than 100 nm [23,26-28].

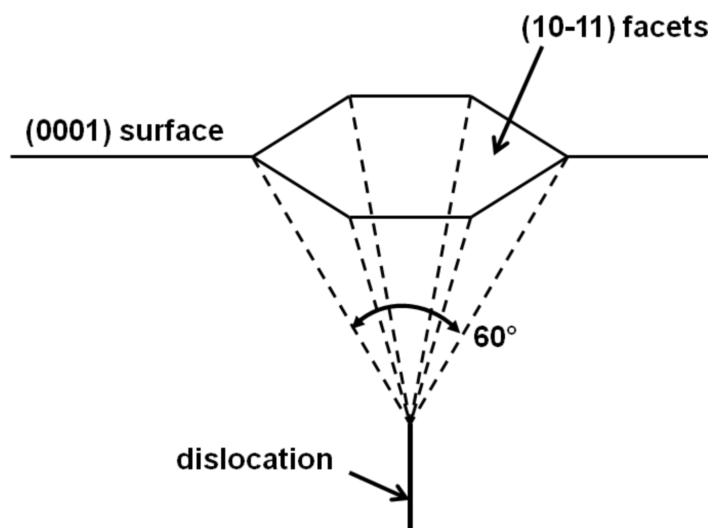

Figure 2.7: Schematic view of a v-defect

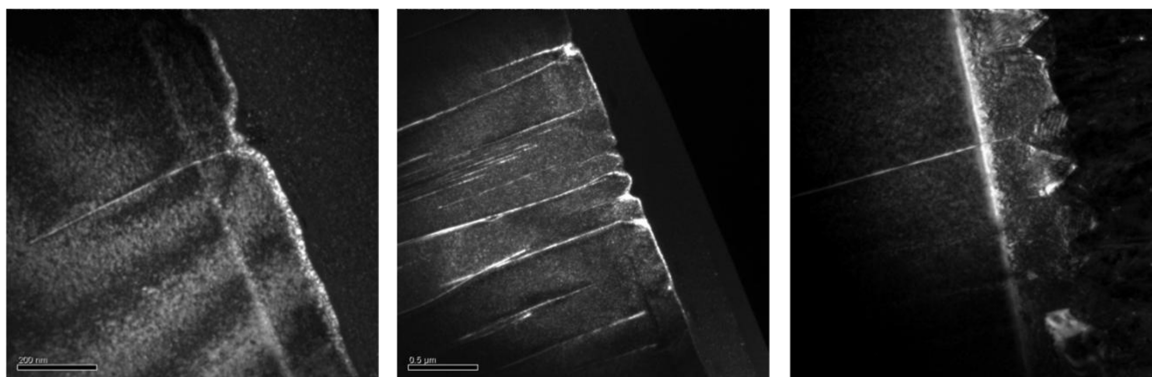

Figure 2.8: TEM images of v-pits in sample InGaN-1 (left), InGaN-2 (center) and InGaN-3 (right)

Figure 2.8 shows more precise TEM images of the v-pits. Notably, we can observe the intersection of a threading dislocation core with the apex of a defect. Each dislocation is not necessarily related to a v-pit, but TEM pictures cannot be used to verify this: while we can observe images of v-defects without an associated threading dislocation, it can be because the dislocation core is in front of or behind the section examined by TEM. It's also interesting to note that the dislocation density in InGaN grown by MOCVD lies between 10^8 cm^{-2} and 10^{10} cm^{-2} while the density of the v-defects has been reported to be between 10^6 cm^{-2} and 10^9 cm^{-2} [25-27,30]. In our own AFM measurements (Figure 2.9), we can count a couple of dozens of v-defects per square micron, i.e. a density of about 10^7 cm^{-2}.

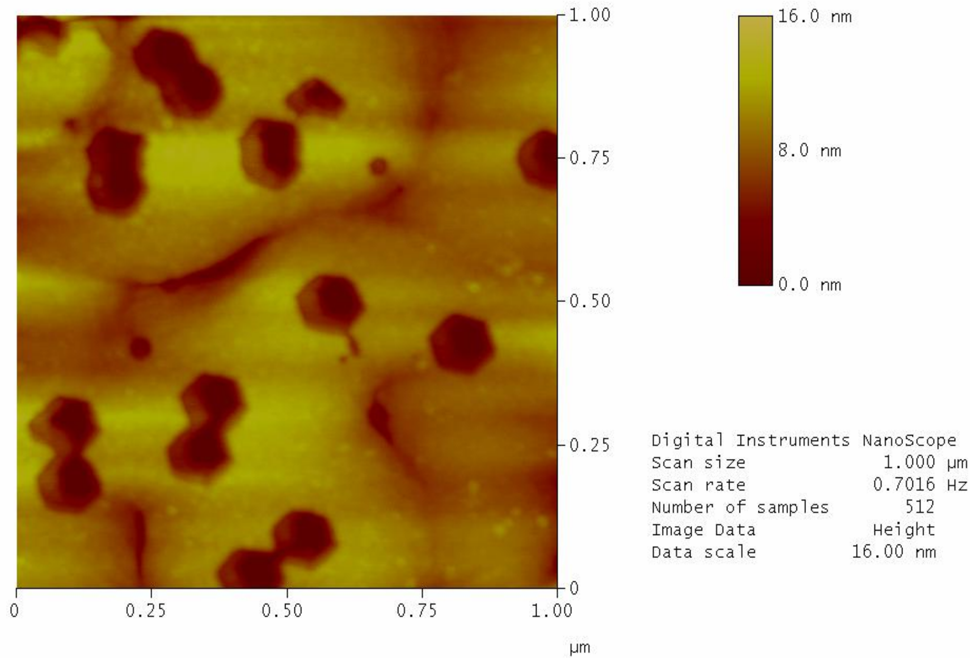

Figure 2.9: AFM picture of the v-defects on sample InGaN-1

The nucleation of a v-defect in the InGaN film is the result of complex interactions between chemical inhomogeneity, strain due to the lattice mismatch with the GaN underlayer and surface mediation by dislocation cores [27,30]. It is seen from a thermodynamic standpoint as a way to release surface energy, strain energy and the termination of dislocation core energy [29].

2.2.1.2 X-ray diffraction

The estimation of the In mole fraction from XRD spectra are based on the shift in planar spacing associated with the substitution of an alloying element. ω-2θ scans of the 0002 diffraction peaks were conducted on a PANalytical X'Pert PRO XRD with a Cu sealed anode and a four-crystal monochromator with Ge(220) configuration.

According to Bragg's law, constructive interferences occur when the path difference is an integer of wavelength, as seen in Figure 2.10.

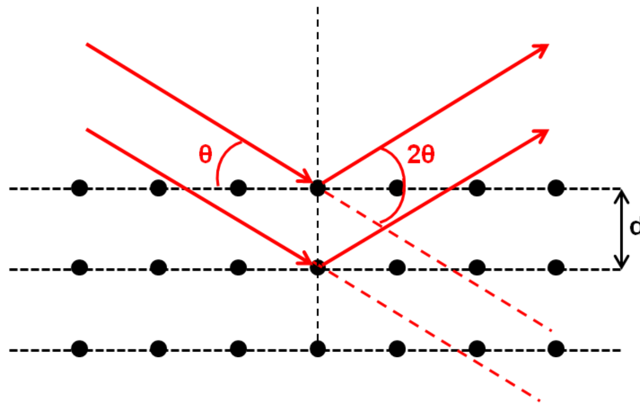

Figure 2.10: Conditions required for Bragg diffraction

$$n \cdot \lambda = 2d \cdot sin\,(\theta) \qquad (2.4)$$

n being the order of reflection, λ the wavelength of the incident x-ray (λ=1.5406 Å for the Cu-Kα line), d the interplanar spacing and θ the Bragg angle [31]. The composition x can be calculated by applying Vegard's law, following a linear interpolation of the lattice parameter with the pure binary alloys as end points and under the assumption that any increase in planar spacing is isotropic throughout the solid:

$$x = \frac{d_{InGaN} - d_{GaN}}{d_{InN} - d_{GaN}} \qquad (2.5)$$

d_{GaN} and d_{InN} are calculated with the values of c given in Table 1-1 as c=2.d for (0002) planes.

Data of the symmetric (0002) reflections are plotted in Figure 2.11 and measured values of x are reported in Table 2-7. The position of the InGaN peaks shift to a lower angle with the increase of x, indicating the expected increase in the c lattice constant [18]. The peak's width (through their measure full width at half maximum, or FWHM) broadens with x which suggests an increase in the compositional inhomogeneity with films of higher In fraction [32].

It's important to keep in mind that a single symmetric XRD measurement can only provide one of the two lattice parameters of the material [31]. On- and off-axis scans are necessary to extract the composition and strain of the films which both influence the position of the XRD peaks [15,18,33]. In our case, we can assume that our samples are partially or fully relaxed as we are well above the critical layer thickness, which makes the contribution of the strain less important. Still, we should observe an overestimation of the compositions compared to results from other methods due to this internal strain.

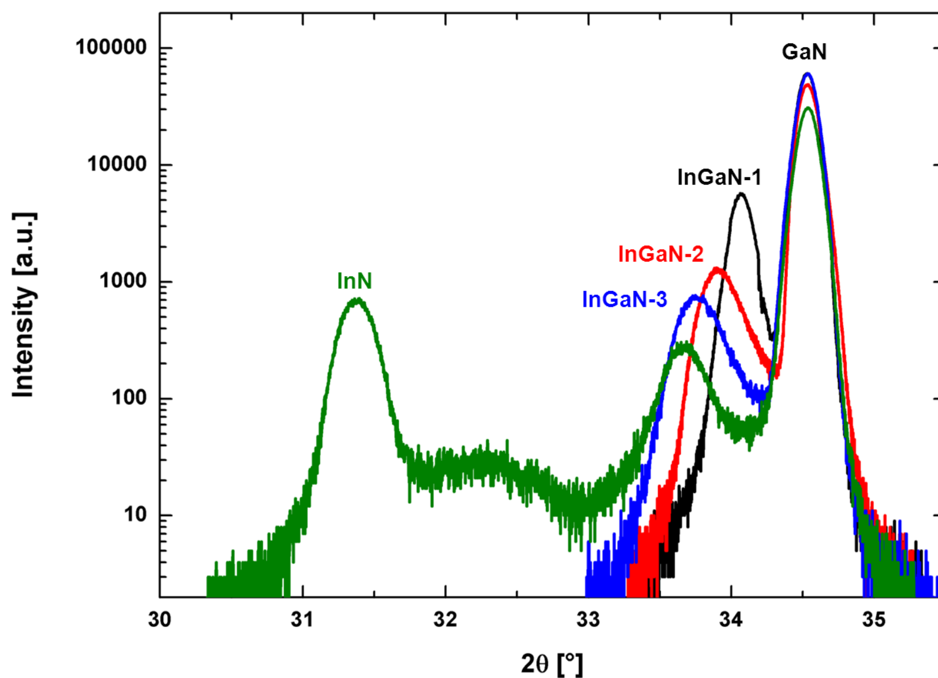

Figure 2.11: (0002) XRD scans of samples InGaN-1 (black), InGaN-2 (red), InGaN-3 (blue) and InN (green)

Sample name	Layer	Peak position [°]	FWHM [°]	XRD In fraction [ ]	Intended In fraction [ ]
InGaN-1	InGaN	34.069	0.082	0.077	0.01
InGaN-2	InGaN	33.904	0.118	0.121	0.1
InGaN-3	InGaN	33.749	0.138	0.165	0.3
InN	InGaN	33.671	0.140	0.187	0.3
	InN	31.373	0.129	0.969	1

Table 2-7: XRD results for the InGaN monolayer samples

The measured values are quite different from the expected ones, higher for InGaN-1 and InGaN-2, lower for InGaN-3 and InN. This goes to show the difficulty to estimate the indium incorporation rate in a thin film grown by MOCVD. In our case, reaching In fraction superior to 0.2 is limited by the maximum TMIn flux we can insert in the MOCVD reactor (400sccm). Decreasing the TMGa flux to 3 sccm to maximize the In/Ga adatoms ratio only has a limited influence as the primary factor remains the temperature. The width (FWHM) of the peaks

increases with the indium fraction, suggesting a less homogeneous and/or more stress inside the InGaN layers, yet no phase separation is observed.

2.2.1.3 Photoluminescence

We established in chapter one a relationship between the bandgap energy and the indium fraction using Equations (1.1) and (1.2) so the measurement of the band gap of our samples through photoluminescence (PL) provides us with another way to determine the composition of $In_xGa_{1-x}N$ thin films.

However, internal strain could have a strong influence on the measurements and skew our results if not accounted for [34]. By using micro-PL, we focus the incident beam at the surface of our samples where we expect the films to be relaxed, hence providing values of the bandgap energy that can be directly related to the composition.

Room-temperature micro-PL spectra are collected using a 325 nm HeCd excitation laser for the InGaN samples and 785 nm laser for InN and are reported in Figure 2.12. Intensities are being normalized to clearly distinguish peak features. Without normalization, the peak intensities are inversely proportional to emission wavelength. Estimation results using Equations (1.1) and (1.2) are tabulated in Table 2-8.

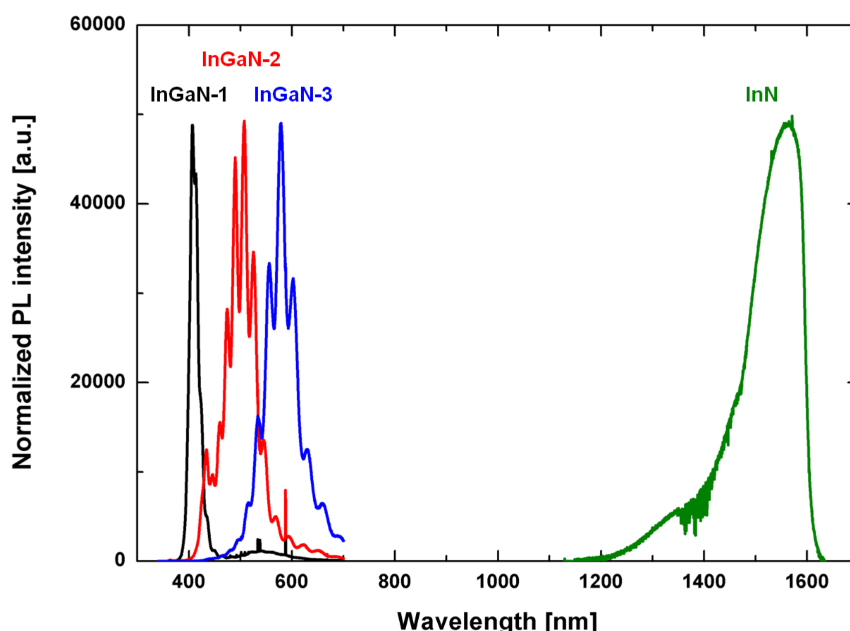

Figure 2.12: Normalized room-temperature micro-PL emission spectra for samples InGaN-1 (black), InGaN-2 (red), InGaN-3 (blue) and InN (green)

Sample name	Peak position [nm]	Peak position [eV]	FWHM [nm]	Micro-PL In fraction [ ]	Intended In fraction [ ]
InGaN-1	410	3.02	18	0.03	0.01
InGaN-2	504	2.46	53	0.09	0.1
InGaN-3	579	2.14	59	0.14	0.3
InN	1540	0.81	114	0.96	1

Table 2-8: Micro-PL results for the InGaN monolayer samples

The values are slightly inferior compared to the results extracted from XRD characterization, suggesting that the InGaN layers are not fully relaxed, at least until a certain depth. Sample InGaN-1 exhibits a broad and weak peak between 500 nm and 600 nm, which has been commonly reported for n-GaN in literature [19,35]. The origin of this yellow emission is still under debate, with hypothesis including complexes of extended defects and point defects or impurities [36-38], edge dislocations [39] and N vacancies [40].

The fringe appearance of the PL emission spectra of samples InGaN-2 and InGaN-3 is caused by interferences of the multiple reflections of light between the reflecting surfaces (InGaN, GaN and sapphire) known as Fabry-Pérot [41]. These resonant reflections are related to the film thickness by:

$$d = \frac{\lambda_1 \cdot \lambda_2}{2 \cdot [\lambda_2 \cdot n(\lambda_1) - \lambda_1 \cdot n(\lambda_2)]} \tag{2.6}$$

where λ_1 and λ_2 correspond to the wavelengths of two successive interference peaks and $n(\lambda)$ is the refractive index calculated using the first order Sellmeier dispersion equation given by:

$$n(\lambda) = A^2 + \frac{B^2}{\lambda^2 - C^2} \tag{2.7}$$

with A, B and C being fitting parameters. As these factors have not been determined for InGaN yet and as the GaN/InGaN film acts as one single interference layer, we use the fitting values for GaN [42,43]. We determine thicknesses around 2.5 µm for both samples InGaN-2 and InGaN-3. These values determined from the Fabry-Pérot interference patterns are in good agreement with the thicknesses determined by SEM and TEM measurements.

Additionally, the peak width (FWHM) increases with the indium mole fraction, providing further evidence that the homogeneity of the samples decreases with increasing indium fraction.

2.2.1.4. Secondary ion-mass spectrometry

To validate our results, we conduct a series of time-of-flight secondary ion mass spectroscopy (ToF-SIMS) measurements. ToF-SIMS allows determination of chemical composition of materials and the distribution of chemical species through the depth of the sample using a pulsed primary ion beam to desorb and ionise atoms and molecules from the surface of the sample. The resulting secondary ions are accelerated into a mass spectrometer, which measures their “time-of-flight” from the sample surface to the detector to determine the mass of the ions. Due to the different masses of each element, analysis of the mass spectrum allows us to determine what elements are in the sample. Depth profiles are obtained when the sample is gradually sputtered and mass spectra are measured from deeper and deeper layers.

As we do not have InGaN reference samples to calibrate the SIMS equipment, two samples (InGaN-3 and InGaN-2-ML) were first sent out to Evans Analytical Group (EAG) Labs for analysis. These data are used as reference for the rest of our own measurements. Figures 2.13 and 2.14 present the SIMS data for InGaN and InN samples, respectively.

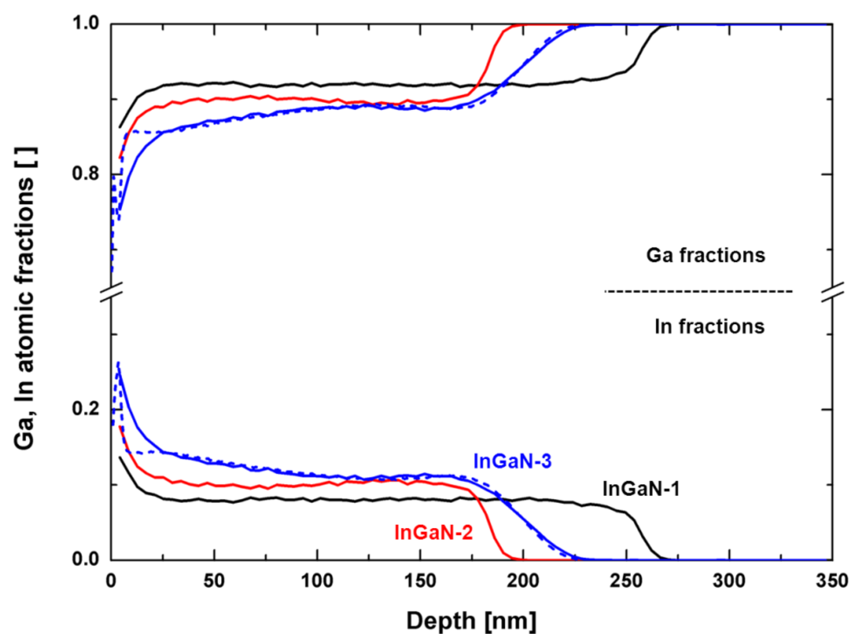

Figure 2.13: SIMS profiles of samples InGaN-1 (black), InGaN-2 (red) and InGaN-3 (blue)

In Figure 2.13, gallium fractions are in the top half of the graph and indium fractions in the bottom half. The dashed line represents the data provided by EAG and according to which we calibrate our measurements (solid lines). The samples InGaN-1 and InGaN-2 present flat profiles, which confirms the steady, homogeneous incorporation of indium in the InGaN layer. The indium fraction for sample InGaN-3 is not constant and varies between 0.109 and 0.144, meaning that the incorporation of In was more efficient in the later part of the growth process and that the upper part of the InGaN layer is richer in indium than the lower one. The SIMS study also provides indication on the depth of the layers, which confirms the observation that were initially carried out through SEM and TEM (section 2.2.1.1)

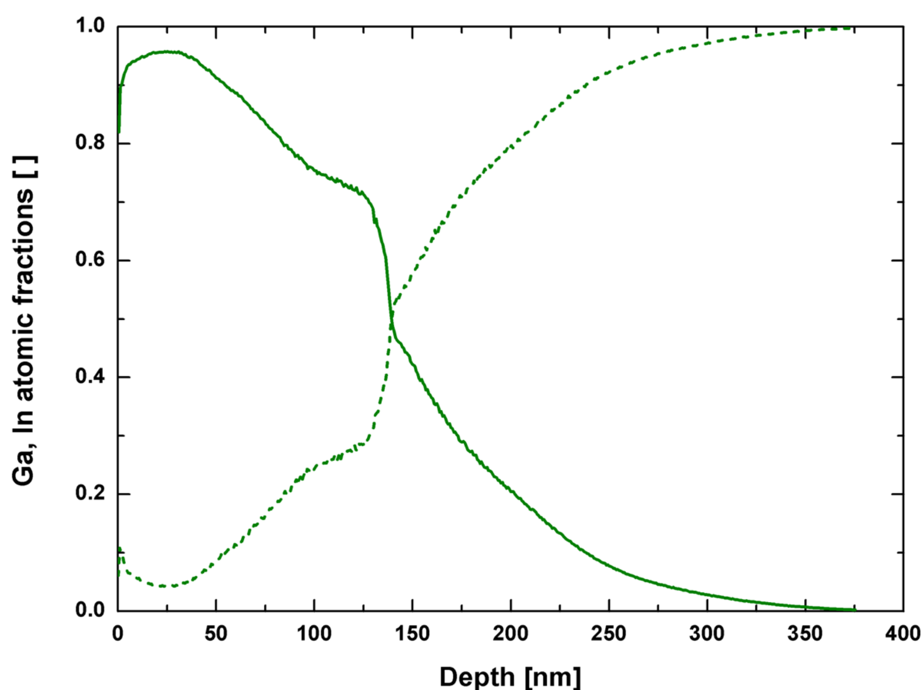

Figure 2.14: SIMS profile of the InN sample for In (solid) and Ga (dashed)

Figure 2.14 reveals that the InN sample is in fact an InGaN sample with a high In content. Only the top-50 nm of the thin film possesses an indium fraction superior to 0.9, which is in good agreement with the values we obtained from the micro-PL. The fraction then diminishes to 0.75 then brutally drops to 0.5 and slowly decreases until it reaches 0, showing the difficulty to grow InN.

Table 2-9 regroups the information we could gather from the SIMS study:

Sample name	Top layer thickness [nm]	SIMS In fraction [ ]	Intended In fraction [ ]
InGaN-1	250	0.07	0.01
InGaN-2	180	0.10	0.1
InGaN-3	180	0.11-0.14	0.3
InN	130	0.70-0.96	1

Table 2-9: SIMS results for the InGaN monolayer samples

2.2.1.5 Summary

Tables2-10 and 2-11 regroups the conclusions on the InGaN layers characteristics from each method that we used:

Sample name	Intended		SEM/TEM		Micro-PL	SIMS
	GaN layer thickness [µm]	Top-layer thickness [nm]	GaN layer thickness [µm]	Top-layer thickness [nm]	GaN + top-layer thickness [µm]	Top-layer thickness [nm]
InGaN-1	2.0	200-300	2.4	180	-	250
InGaN-2	2.0	200-300	2.2	190	2.5	180
InGaN-3	2.0	200-300	2.2	250	2.5	180
InN	2.0	300	1.6	350	-	130

Table 2-10: Structures of the InGaN monolayer samples summary

Sample name	Intended In fraction [ ]	XRD In fraction [ ]	Micro-PL In fraction [ ]	SIMS In fraction [ ]
InGaN-1	0.01	0.077	0.03	0.07
InGaN-2	0.1	0.121	0.09	0.10
InGaN-3	0.3	0.165	0.14	0.11-0.14
InN	1	0.969	0.96	0.70-0.96

Table 2-11: Composition of the InGaN monolayer samples summary

The values on film thicknesses are reasonably consistent in a range between SEM, TEM, SIMS and micro-PL interference patterns. Composition values differ slightly from a study to another but form a coherent set, although far from the expected indium fractions we hoped to achieve in the first place.

We've already established and can verify that anisotropic strain associated with lattice mismatch and pseudomorphic growth of the films on the GaN-on-sapphire template leads to an overestimation in the composition obtained from XRD (0002) scans. The values calculated from room-temperature micro-PL are similar to the ones we determined through SIMS in the top 50 nm and will be used as reference for the rest of the study.

2.2.2 InGaN multilayer thin films characterization

Incorporating high indium fractions in InGaN monolayers is a difficult task. We mentioned in section 1.2.4.4 how strained InGaN films were able to accommodate higher indium content at lower temperatures compared to their relaxed counterparts, so we use the MOCVD capability to grow heterostructures in a sequenced single deposition operation to reach compositions with more indium and better crystal quality. A study covering SEM, TEM, XRD, micro-PL and SIMS is conducted on the multilayer samples InGaN-1-ML, InGaN-2-ML and InGaN-3-ML.

2.2.2.1 Microscopy

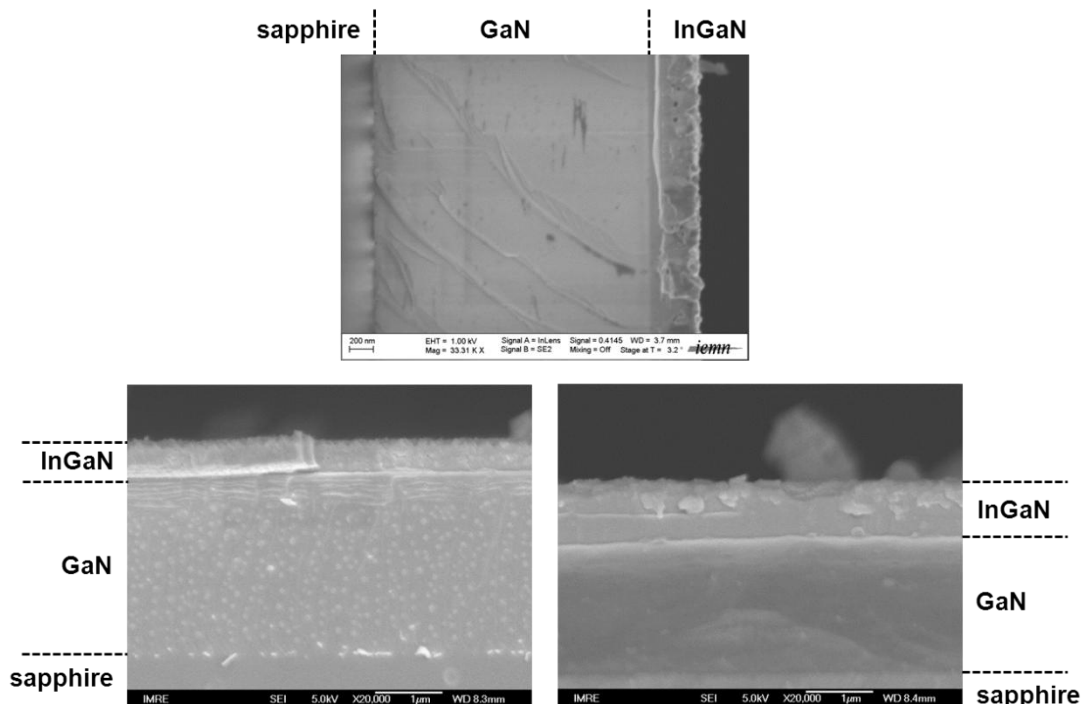

Figure 2.15: SEM images of samples InGaN-1-ML (top center), InGaN-2-ML (bottom left) and InGaN-3-ML (bottom right)

Figure 2.15 shows SEM images of the three samples. The multilayer structure cannot be observed but the total layer thickness of the InGaN layer appears to be consistent with the cumulated thicknesses of the multiple layers of the structures.

The multilayer character of the samples only appears in the case of InGaN-3-ML under TEM observation. We can count the 6 periods on Figure 2.16 and measure their average size to 65 nm. A v-pit and its associated threading dislocation are clearly displayed. The v-pit goes through the top three InGaN layers and the dislocation through the bottom three ones.

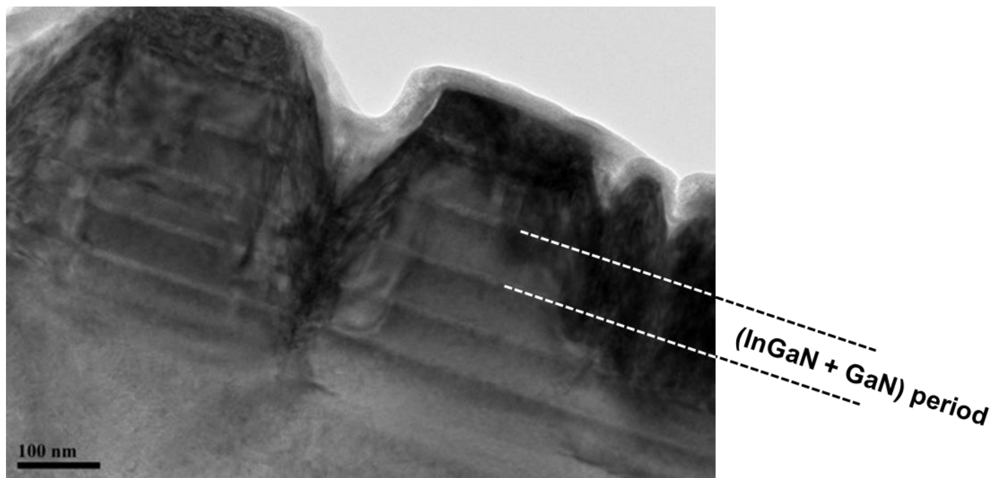

Figure 2.16: TEM image of sample InGaN-3-ML

Table 2-12 presents the information we could extract from SEM and TEM study:

Sample name	GaN layer thickness [µm]	Multilayer structure thickness [nm]
InGaN-1-ML	2.3	410
InGaN-2-ML	2.5	420
InGaN-3-ML	2.0	390

Table 2-12: Layer thicknesses of the InGaN multilayer samples

2.2.2.2 X-ray diffraction

Similarly to what is done with mono-lay samples, (0002) XRD reflection spectra are examined to determine the composition of the InGaN layers. The curves plotted in Figure 2.17 are used to estimate the In fraction.

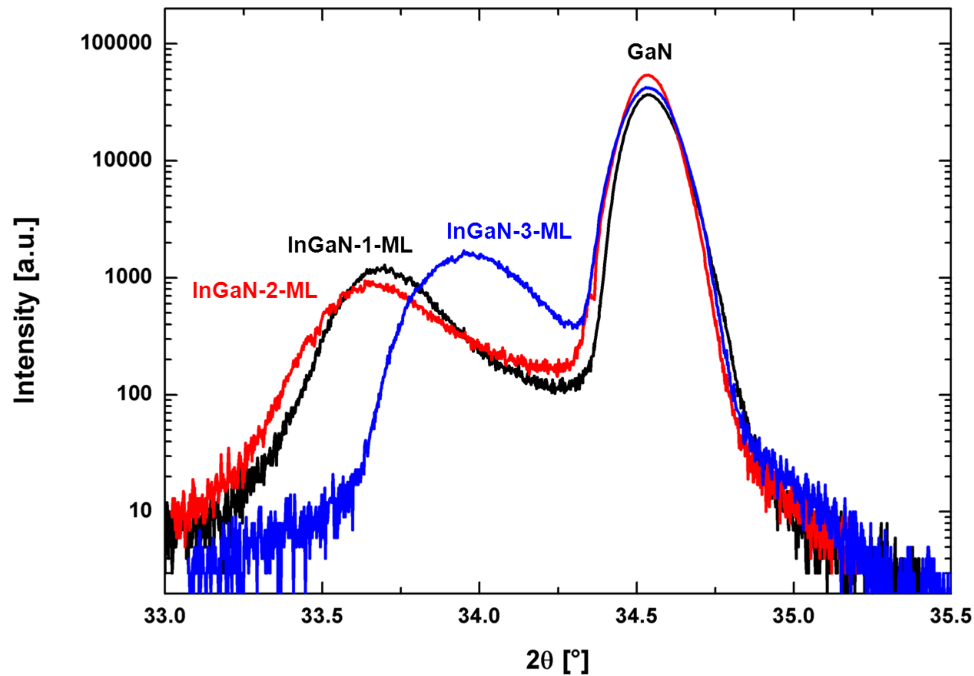

Figure 2.17: (0002) XRD scans of samples InGaN-1-ML (black), InGaN-2-ML (red) and InGaN-3-ML (blue)

Two approximations are made for the calculations related to determining the indium content of the InGaN layers from the position of the XRD peaks:

- as we already mentioned, the strain inside the InGaN layers, still undetermined as we only access to symmetric XRD measurements, results in an overestimation of the In content. In the case of monolayer samples, this may only play a small role, but its importance grows with structures closer to the critical layer thickness.
- the multilayer $In_xGa_{1-x}N$/GaN structure in each sample is considered as a single layer of similar composition x. This means that we should obtain compositions slightly less In-rich than they really are.

Table 2-13 presents the results from the calculations done with these assumptions. The measured indium fractions indeed seem to be higher than in the case of the monolayer samples, but further investigation is necessary to make sure that this is not related to the

internal strain shifting the position of the peaks. FWHM is consistently higher than for monolayer samples, which can be explained by higher In content and by strain, distorting the lattice over a broader range.

Sample name	Layer structure	Peak position [°]	FWHM [°]	XRD In fraction []	Intended In fraction []
InGaN-1-ML	3 * 130 nm	33.692	0.292	0.256	0.3
InGaN-2-ML	6 * 60 nm	33.664	0.352	0.264	0.3
InGaN-3-ML	6 * 60 nm	33.966	0.354	0.171	0.2

Table 2-13: XRD results for the InGaN multilayer samples

2.2.2.3 Photoluminescence

Micro-PL measurements are reported on Figure 2.18 and Table 2-14.

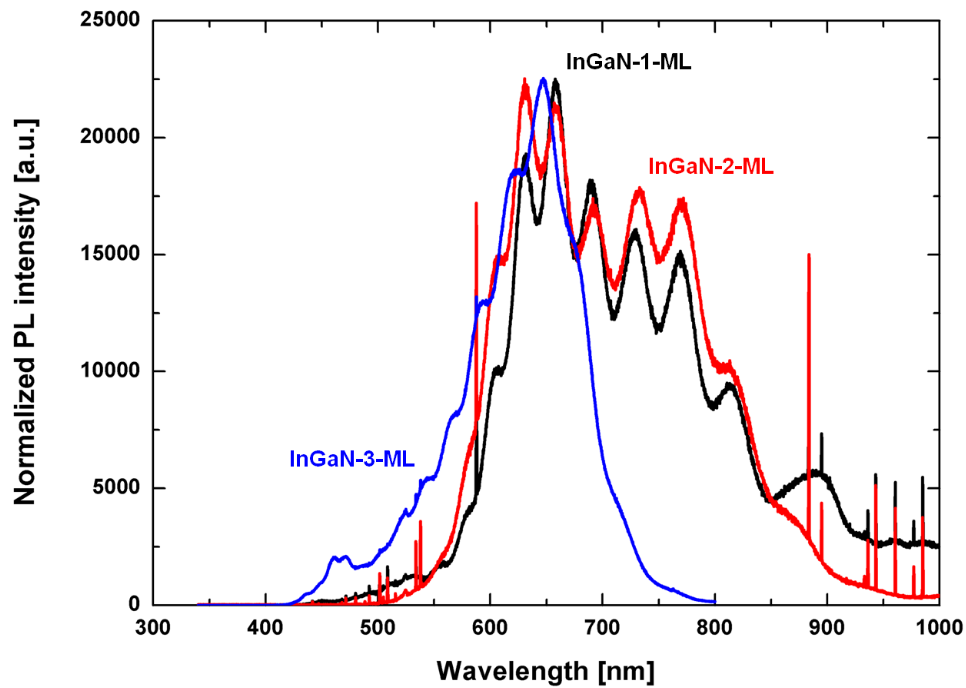

Figure 2.18: Normalized room-temperature micro-PL emission spectra for samples InGaN-1-ML (black), InGaN-2-ML (red) and InGaN-3-ML (blue)

Sample name	Peak position [nm]	Peak position [eV]	FWHM [nm]	Micro-PL In fraction []	Intended In fraction []
InGaN-1-ML	669	1.85	167	0.23	0.3
InGaN-2-ML	655	1.88	199	0.21	0.3
InGaN-3-ML	647	1.92	104	0.18	0.2

Table 2-14: Micro-PL results for the InGaN multilayer samples

The compositions given by micro-PL are inferior to the ones provided by XRD except for sample InGaN-3-ML. This discrepancy can be explained by the fact that the micro-PL experiment only interacts with the surface of the samples. We don't have any evidence of a multilayer structure for samples InGaN-1-ML and InGaN-2-ML so we can expect similar comparisons as with monolayer samples. For the InGaN-3-ML sample however, clear InGaN multiple layers can be observed in TEM images (see Figure 2.16). A possible explanation is that micro-PL measures the indium fraction in the top InGaN layer, while XRD accounts for the GaN interlayers too.

If we try to use the interference fringes and Equations (2.6) and (2.7) to measure the size of the Fabry-Pérot cavity, we obtain thicknesses of 2.7 µm, 2.8 µm and 2.6 µm for sample InGaN-1-ML, InGaN-2-ML and InGaN-3-ML respectively. These values are in agreement with the added GaN and InGaN thicknesses determined by SEM and TEM.

2.2.2.4 Secondary ion-mass spectrometry

As for monolayer samples, a sample (InGaN-2-ML) was first characterized through SIMS by EAG labs to provide a benchmark and a reference point for the rest of our analysis. The samples are all analyzed at IMRE and results are displayed in Figure 2.19. Gallium fractions are reported in the upper half, indium ones in the lower half. Table 2-15 gives tabulated results of the study.

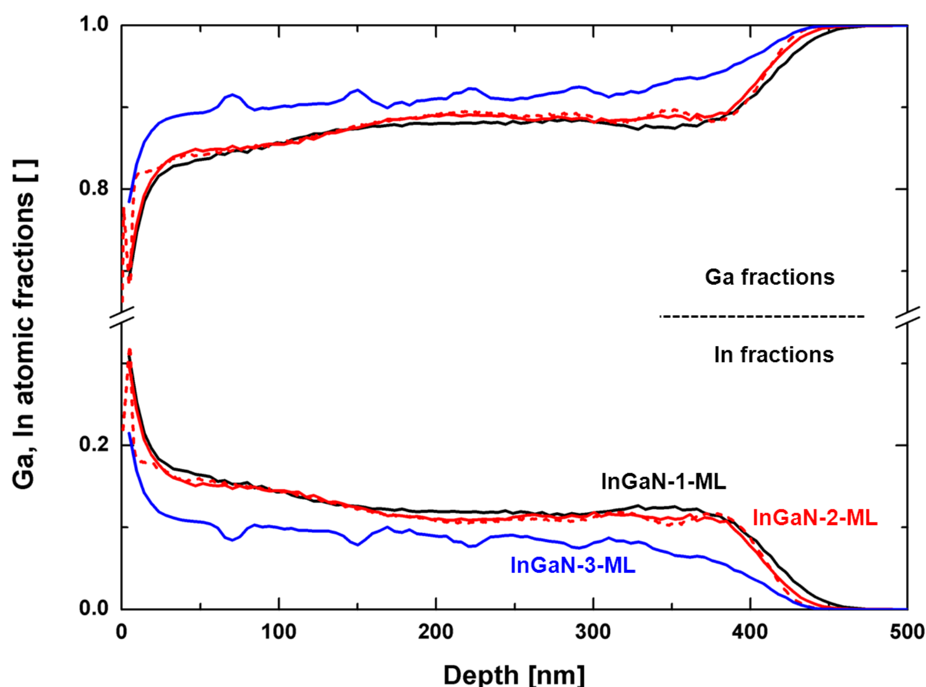

Figure 2.19: SIMS profiles of samples InGaN-1-ML (black), InGaN-2-ML (red) and InGaN-3-ML (blue)

Sample name	Top layer thickness [nm]	SIMS In fraction [ ]	Intended In fraction [ ]
InGaN-1-ML	400	0.12-0.17	0.3
InGaN-2-ML	400	0.11-0.17	0.3
InGaN-3-ML	370	0.09-0.12	0.2

Table 2-15: SIMS results for the InGaN multilayer samples

The obtained indium contents are once again much lower than the expected ones, by a factor around 2, as we could already observe for sample InGaN-3 in the monolayer samples' study. The multilayer structure doesn't improve the stability of the composition with depth as well compared to the InGaN-3 sample. Sample InGaN-2-ML shows a more flat profile, due to its lower indium fraction.

As seen in SEM and TEM images and suggested by XRD and micro-PL studies, no sign of multilayer structure is found for samples InGaN-1-ML and InGaN-2-ML. The depth precision of the SIMS measurements is 3 nm so even a 10 nm-interlayer should show up on the depth profiles if it existed, as it does for sample InGaN-3-ML. It's not surprising that the

GaN interlayers are not displayed as only containing Ga in the SIMS profile: the growth process has already shown how difficult abrupt transitions are to realize for the InN sample, on top of which the ToF-SIMS adds its own special resolution issues. The average period of the structure is around 80 nm, slightly more than the expected value of 70 nm.

2.2.2.5 Summary

Tables 2-16 and 2-17 gather the results we obtained for the InGaN multilayer samples from the different studies for layer structure and composition respectively:

Sample name	Intended		SEM/TEM		Micro-PL	SIMS
	GaN layer thickness [µm]	**Multilayer thickness [nm]**	**GaN layer thickness [µm]**	**Multilayer thickness [nm]**	**GaN + multilayer thickness [µm]**	**multilayer thickness [nm]**
InGaN-1-ML	2.0	430	2.3	410	2.7	400
InGaN-2-ML	2.0	430	2.5	420	2.8	400
InGaN-3-ML	2.0	430	2.0	390	2.6	370

Table 2-16: Structures of the InGaN multilayer samples summary

Sample name	Intended In fraction [ ]	XRD In fraction [ ]	Micro-PL In fraction [ ]	SIMS In fraction [ ]
InGaN-1-ML	0.3	0.256	0.23	0.12-0.17
InGaN-2-ML	0.3	0.264	0.21	0.11-0.17
InGaN-3-ML	0.2	0.171	0.18	0.09-0.12

Table 2-17: Composition of the InGaN multilayer samples summary

While we can only observe the size of each layer in the multistructure with TEM or SIMS, we can still observe total size of the InGaN/GaN heterostructures. Measured values form a coherent group and are in good agreement with the intended numbers, except for the double GaN layer that was grown in the template of sample InGaN-1-ML.

Observations reveal that a multilayer structure was only clearly achieved in the case of sample InGaN-3-ML. Samples InGaN-1-ML and InGaN-2-ML look to be only composed of a single InGaN layer with indium content fluctuations similar to a monolayer sample having the same intended composition. Broader XRD and micro-PL peaks reveal the presence of

internal stress that is also the reason for the overestimation in indium contents obtained through these indirect methods compared to SIMS study [44].

2.2.3 Structures and compositions summary

We've lead in this second chapter the characterization of InGaN single layers and multilayer structures grown by MOCVD. SEM, TEM, AFM, XRD, micro-PL and SIMS were used to determine the structures and composition of the samples. This step is decisive as we must know precisely how the studied samples are structured and how much indium the InGaN layers contain for the following optical parameter characterization. Ultimately, we decide to only work with the monolayer set of samples with the following values:

Sample name	**GaN layer thickness [nm]**	**Top layer thickness [nm]**	**In fraction [ ]**
InGaN-1	2.4	250	0.07
InGaN-2	2.2	180	0.10
InGaN-3	2.2	180	0.14
InN	1.6	130	0.96

Table 2-18: Structure and composition of the samples used for the rest of this study

These samples will be optically characterized in the visible and terahertz frequency domains in Chapters 3 and 4 respectively.

References

[1] H.M. Manasevit, “Single-crystal gallium arsenide on insulating substrates”, *Appl. Phys. Lett.* **12**, 156-159 (1968)

[2] R.F. Karlicek, M. Schurman, C. Tran, T. Salagaj, Y. Li and R.A. Stall, “Growth of GaN blue LEDs with in situ growth monitoring”, *III-Vs Review* **10**, 20-24 (1997)

[3] W.G. Breiland and K.P. Killeen, “A virtual interface method for extracting growth rates and high temperature optical constants from thin semiconductor films using *in situ* normal incidence reflectance”, *J. Appl. Phys.* **78**, 6726-6736 (1995)

[4] R.F. Davis, S.M. Bishop, S. Mita, R. Collazo, Z.J. Reitmeier and Z. Sitar, “Epitaxial growth of gallium nitride”, *AIP Conf. Proc.* **916**, 520-540 (2007)

[5] T. Matsuoka, N. Yoshimoto, T. Sasaki and A. Katsui, “Wide-gap semiconductor InGaN and InGaAlN grown by MOVPE”, *J. Electron. Mater.* **21**, 157-163 (1992)

[6] H.C. Lin, C.K. Shu, J. Ou, Y.C. Pan, W.K. Chen, W.H. Chen and M.C. Lee, “Growth temperature effects on $In_xGa_{1-x}N$ films studied by X-ray and photoluminescence”, *J. Cryst. Growth* **189/190**, 57-60 (1999)

[7] S.M. Bedair, F.G. McIntosh, J.C. Roberts, E.L. Piner, K.S. Boutros, N.A. El-Masry, “Growth and characterization of In-based nitride compounds”, *J. Cryst. Growth* **178**, 32-44 (1997)

[8] E.L. Piner, M.K. Behbehani, N.A. El-Masry, F.G. McIntosh, J.C. Roberts, K.S. Boutros and S.M. Bedair, “Effect of hydrogen on the indium incorporation in InGaN epitaxial films”, *Appl. Phys. Lett.* **70**, 461-463 (1997)

[9] A. Kadir, T. Ganguli, M.R. Gokhale, A.P. Shah and A. Bhattacharya1, “The role of InGaN interlayers on the microstructure of InN epilayers grown via metal organic vapour phase epitaxy”, *Phys. Stat. Sol. (a)* **207**, 1070-1073 (2010)

[10] A.D. Bykhovski, B.L. Gelmont, and M.S. Shur, “Elastic strain relaxation and piezoeffect in GaN-AlN, GaN-AlGaN and GaN-InGaN superlattices”, *J. Appl. Phys.* **81**, 6332-6338 (1997)

[11] Y. Ono, Y. Iyechika, T. Takada, K. Inui and T. Matsue, “Reduction of etch pit density on GaN by InGaN-strained SQW”, *J. Cryst. Growth* **189/190**, 133-137 (1999)

[12] K. Li, A.T.S. Wee, J. Lin, Z.C. Feng and E.W.P. Lau, “Compositional and morphological analysis of $In_xGa_{1-x}N$/GaN epilayers”, *Surf. And Int. Analysis* **28**, 181-185 (1999)

[13] S. Keller, B.P Keller, M.S. Minsky, J.E. Bowers, U.K. Mishra, S.P. DenBaars and W. Seifert, “Growth and properties of InGaN nanoscale islands on GaN”, *J. Cryst. Growth* **189/190**, 29-32 (1999)

[14] S. Nakamura and T. Mukai, “High-Quality InGaN Films Grown on GaN Films”, *Jpn. J. Appl. Phys.* **31**, L1457-L1459 (1992)

[15] H.P.D. Schenk, P. de Mierry, M. Laügt, F. Omnès, M. Leroux, B. Beaumont and P. Gibart, “Indium incorporation above 800°C during metalorganic vapor phase epitaxy of InGaN”, *Appl. Phys. Lett.* **75**, 2587-2589 (1999)

[16] S. Keller, B.P. Keller, D. Kapolnek, A.C. Abare, H. Masui, L.A. Coldren, U.K. Mishra and S.P. DenBaars, “Growth and characterization of bulk InGaN films and quantum wells”, *Appl. Phys. Lett.* **68**, 3147-3149 (1996)

[17] S. Keller, B.P. Keller, D. Kapolnek, U.K. Mishra, S.P. DenBaars, I.K. Shmagin, R.M. Kolbas and S. Krishnankutty, “Growth of bulk InGaN films and quantum wells by atmospheric pressure metalorganic chemical vapour deposition”, *J. Cryst. Growth* **170**, 349-352 (1997)

[18] M.A. Moram and M.E. Vickers, “X-ray diffraction of III-nitrides”, *Rep. Prog. Phys.* **72**, 036502 (2009)

[19] P. Barletta, *Study of GaN-Based Materials for Light-Emitting Devices*, PhD thesis, North Carolina State University (2006)

[20] M. Shimizu, Y. Kawaguchi, K. Hiramatsu and N. Sawaki, “Metalorganic vapor phase epitaxy of thick InGaN on sapphire substrate”, *Jpn. J. Appl. Phys.* **36**, 3381-3384 (1997)

[21] C.H. Kuo, C.C. Lin, S.J. Chang, Y.P. Hsu, J.M. Tsai, W.C. Lai and P.T. Wang, "Nitride-based light-emitting diodes with p-AlInGaN surface layers", *IEEE Trans. Electron Devices* **52**, 2346-2349 (2005)

[22] X.H. Wu, C.R. Elsass, A. Abare, M. Mack, S. Keller, P.M. Petroff, S.P. DenBaars, J.S. Speck and S.J. Rosner, "Structural origin of V-defects and correlation with localized excitonic centers in InGaN/GaN multiple quantum wells", *Appl. Phys. Lett.* **72**, 692-694 (1998)

[23] S. Mahanty, M. Hao, T. Sugahara, R.S.Q. Fareed, Y. Morishima, Y. Naoi, T. Wang and S. Sakai, "V-shaped defects in InGaN/GaN multiquantum wells", *Mat. Lett.* **41**, 67-71 (1999)

[24] Z. Liliental-Weber, Y. Chen, S. Ruvimov and J. Washburn, "Formation Mechanism of Nanotubes in GaN", *Phys. Rev. Lett.* **79**, 2835–2838 (1997)

[25] F. Lin, N. Xiang, P. Chen, S. Y. Chow and S. J. Chua, "Investigation of the V-pit related morphological and optical properties of InGaN/GaN multiple quantum wells", *J. Appl. Phys.* **103**, 043508 (2008)

[26] K. Uchida, M. Kawata, T. Yang, A. Miwa and J. Gotoh, "Increased size of open hexagonally shaped pits due to growth interruption and its influence on InGaN/GaN quantum-well structures grown by metalorganic vapor phase epitaxy", *Jpn. J. Appl. Phys.* **37**, L571-L573 (1998)

[27] B. Jahnen, M. Albrecht, W. Dorsch, S. Christiansen, H.P. Strunk, D. Hanser and R.F. Davis, "Pinholes, dislocations and strain relaxation in InGaN", *MRS Internet J. Nitride Semicond. Res.* **3**, 1-12 (1998)

[28] A.M. Sánchez, M. Gass, A.J. Papworth, P.J. Goodhew, P. Singh, P. Ruterana, H.K. Cho, R.J. Choi and H.J. Lee, "V-defects and dislocations in InGaN/GaN heterostructures", *Thin Solid Films* **479**, 316-320 (2005)

[29] J.E. Northrup, L.T. Romano and J. Neugebauer, "Surface energetics, pit formation, and chemical ordering in InGaN alloys", *Appl. Phys. Lett.* **74**, 2319-2321 (1999)

[30] Y. Chen, T. Takeuchi, H. Amano, I. Akasaki, N. Yamada, Y. Kaneko and S.Y. Wang, "Pit formation in GaInN quantum wells", *Appl. Phys. Lett.* **72**, 710-712 (1998)

[31] B.D. Cullity, S.R. Stock, *Elements of X-ray Diffraction, 3rd Edition*, Ch. 3-3, Addison Wesley Publishing Company Inc., Reading (2001)

[32] G.K. Williamson and W.H. Hall, "X-ray line broadening from filed aluminum and wolfram", *Acta Mettal.* **1**, 22-31 (1953)

[33] L.T. Romano, B.S. Krusor, M.D. McCluskey, D.P. Bour and K. Nauka, "Structural and optical properties of pseudomorphic $In_xGa_{1-x}N$ alloys", *Appl. Phys. Lett.* **73**, 1757-1759 (1998)

[34] J.-M. Wagner and F. Bechstedt, "Properties of strained wurtzite GaN and AlN: *ab initio* studies", *Phys. Rev. B* **66**, 115202 (2002)

[35] C. Kim, S. Kim, Y. Choi and S.J. Leem, "Correlation between the type of threading dislocations and photoluminescence characteristics at different doping concentrations of Si in GaN films", *J. Appl. Phys.* **92**, 6343-6345 (2002)

[36] F.A. Ponce, D.P. Bour, W. Götz and P.J. Wright, "Spatial distribution of the luminescence in GaN thin films", *Appl. Phys. Lett.* **68**, 57-59 (1996)

[37] I.H. Lee, I.H. Choi, C.R. Lee and S. K. Noh, "Evolution of stress relaxation and yellow luminescence in GaN/sapphire by Si incorporation", *Appl. Phys. Lett.* **71**, 1359-1361 (1997)

[38] J. Oila, J. Kivioja, V. Ranki, K. Saarinen, D.C. Look, R.J. Molnar, S.S. Park, S.K. Lee and J.Y. Han, "Ga vacancies as dominant intrinsic acceptors in GaN grown by hydride vapor phase epitaxy", *Appl. Phys. Lett.* **82**, 3433-3435 (2003)

[39] D.G. Zhao, D.S. Jiang, H. Yang, J.J. Zhu, Z.S. Liu, S.M. Zhang, J.W. Liang, X. Li, X.Y. Li and H.M. Gong, "Role of edge dislocations in enhancing the yellow luminescence of *n*-type GaN", *Appl. Phys. Lett.* **88**, 241917 (2006)

[40] A.E. Yunovich, *Proceedings of the Second Symposium on III–V Nitride Materials and Processes*, Electrochemical Society **98-02**, 258, Electrochemical Society, Pennington (1998)

[41] T. Weber, H. Stolz, W. von der Osten, M. Heuken and K. Heime, "Fabry-Pérot oscillations in epitaxial ZnSe layers", *Semicond. Sci. Technol.* **10**, 1113 (1995)

[42] G. Yu, G. Wang, H. Ishikawa, M. Umeno, T. Soga, T. Egawa, J. Watanabe and T. Jimbo, "Optical properties of wurtzite structure GaN on sapphire around fundamental

absorption edge (0.78–4.77 eV) by spectroscopic ellipsometry and the optical transmission method", *Appl. Phys. Lett.* **70**, 3209-3211 (1997)

[43] C.X. Lian, X.Y. Li and J. Liu, "Optical anisotropy of wurtzite GaN on sapphire characterized by spectroscopic ellipsometry", *Semicond. Sci. Technol.* **19**, 417 (2004)

[44] J. Bai, T. Wang and S. Sakai, "Study of the strain relaxation in InGaN/GaN multiple quantum well structures", *J. Appl. Phys.* **90**, 1740 (2001)

Chapter 3
Optical characterization of InGaN thin films in the visible domain

3. CHAPTER 3 OPTICAL CHARACTERIZATION OF INGAN THIN FILMS IN THE VISIBLE DOMAIN 57

3.1 THE ELLIPSOMETRY OPTICAL CHARACTERIZATION METHOD 60

3.1.1 Interaction of an electromagnetic wave with a medium 60

3.1.1.1 Propagation of an electromagnetic wave through a medium 60

3.1.1.2 Propagation of a polarized electromagnetic wave 63

3.1.1.3 Interaction of an electromagnetic wave with a sample 64

3.1.2 Modeling the optical response of a thin film on a substrate 66

3.1.2.1 Physical principle 67

3.1.2.2 Ideal thin films 67

3.1.2.3 Non-ideal thin films 73

3.1.3 Measures analysis methodology 77

3.1.3.1 Definition and determination of the parameters of the model 77

3.1.3.2 Regularization 78

3.2 EXPERIMENTAL STUDY OF INGAN THIN FILMS 79

3.2.1 Experimental study of a GaN thin film 80

3.2.2 Experimental study of InGaN thin films 82

REFERENCES 85

As a key-parameter describing the interaction of light with a material, the optical index in the visible range (350 nm to 750 nm) is at the heart of the optical characterization. From InGaN-based high-performance device application point of view, a detailed knowledge of this property is crucial. In literature, *Anani et al.* theoretically determined the index dispersion from bandgap calculation [1], showing a hyperbola tendency for wide indium content. *Sanford et al.* reported the refractive index evolution for $In_xGa_{1-x}N$ samples for a narrow range of In content x=0 to 0.07 [2]. *Goldham et al.* used a parametric dielectric function model to obtain refractive indices and extinction coefficients for two cubic $In_xGa_{1-x}N$ samples with x=0.02 and 0.07 [3]. Due to the difficulty to grow thin films with higher indium fractions, very little to no experimental information exist for In compositions above 0.07, a void this chapter hopes to narrow.

There are a number of direct and indirect methods to determine the refractive index of a material, and our initial effort was focused on prism coupling, a method well-known and established within IEMN. This technique observes the evanescent coupling of light through a prism to excite one by one the different guided modes of the incident beam in a wave-guide formed by the film we want to characterize [4]. Figure 3.1 shows the principle of this experiment.

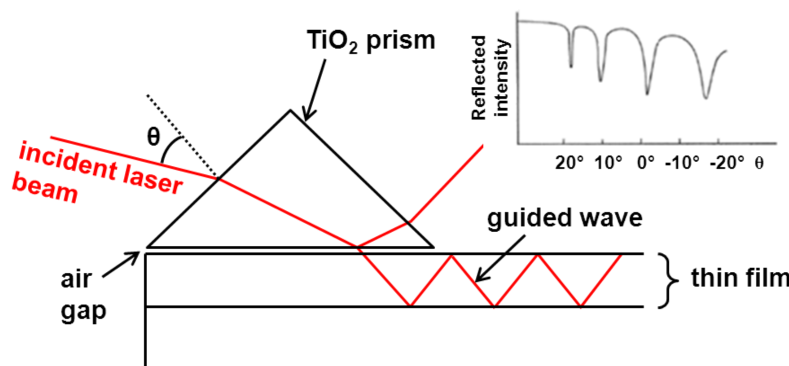

Figure 3.1: Principle diagram of the prism coupling technique

By measuring the reflected intensity versus the angle of incidence θ, we draw the guided-mode spectrum of the material. The reflectivity dips observed at certain angles correspond to the excitation of guided modes in the film structure. Sharp and distinguishable mode lines are detected and indicated the optical quality of this film. From the knowledge of the θ angle for modes along different polarization, we can compute the corresponding effective mode indices N_m, according to:

$$N_m = n_p \cdot sin\left[A_p + arcsin\left(\frac{sin\,\theta}{n_p}\right)\right] \tag{3.1}$$

where n_p is the refractive index of the prism, θ is the angle of incidence and A_p is the prism angle with respect to the normal. From the experimental values of effective indices N_m and using the calculation procedure reported by *Ulrich et al.* [5], the refractive indices of the films and the thickness have been determined simultaneously.

Figure 3.2 displays the reflection spectra for an incident beam along different polarization axes with a wavelength of 1.539 µm for the GaN-on-sapphire template we introduced in the previous chapter [6]. We can observe the different guided modes of the thin film and, by reproducing this experiment at multiple wavelength, we obtain a good idea of the dispersion of the refraction index of the material. Correlation with literature [7,8] proves that our values are accurate and that the template crystal quality is good.

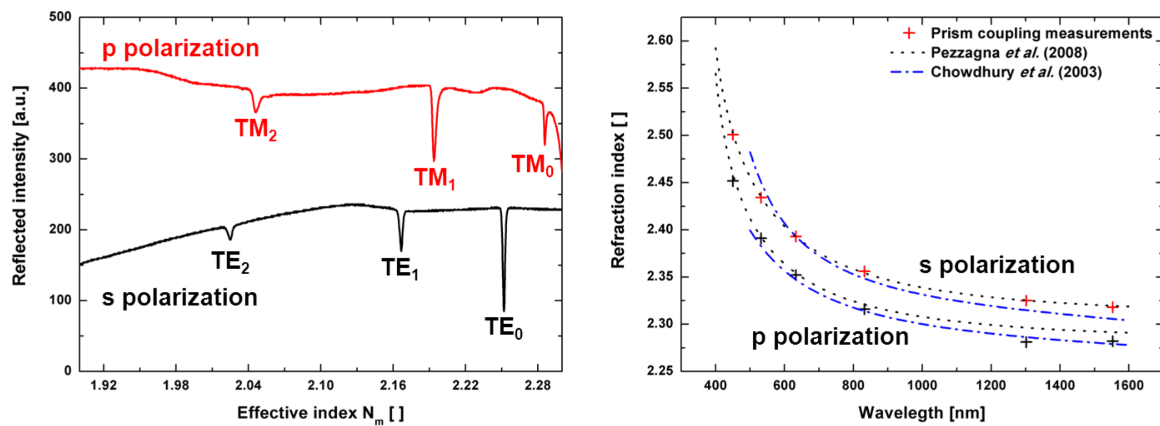

Figure 3.2: Reflection spectra at 1539 nm for polatizations s and p (left); dispersion of the refraction index as a function of wavelength measured by prism coupling and comparison to literature (right)

A major caveat of prism coupling is that it can only characterize thin films whose thickness is larger than the longest wavelength used for measurement. While this is the case for the GaN-on-sapphire template that is 2 µm-thick, it is not for our InGaN samples whose top layer measure only between 130 nm and 250 nm. Existing models also limit the use of this technique to samples with a single or dual layer structure. It's for these reasons that we further focused our investigations on ellipsometry.

3.1 The ellipsometry optical characterization method

Ellipsometry is a technique based on measuring the modification of the polarization state of a polarized light beam after its reflection on a plane surface, as described on the diagram of Figure 3.3.

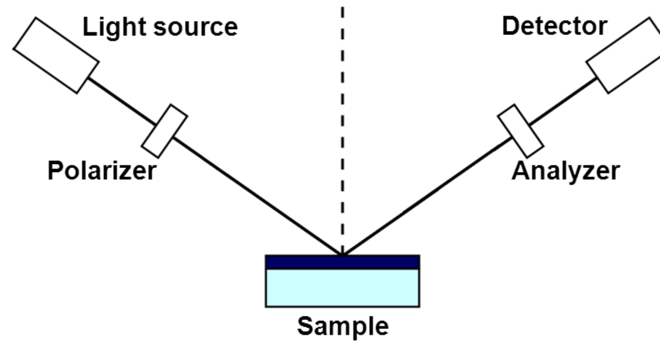

Figure 3.3: Principle diagram of the ellipsometry technique

It is not a direct method that allows to determine the optical index of a material. Instead, a numerical model is used to try and simulate the same experiment to make the result fit the experimental values.

3.1.1 Interaction of an electromagnetic wave with a medium

3.1.1.1 Propagation of an electromagnetic wave through a medium [9,10]

Light is an electromagnetic wave that is described by four vector fields: the electric field $\vec{E}$, the electric displacement field $\vec{D}$, the magnetic field $\vec{H}$ and the magnetic induction $\vec{B}$. These four vectors are related to each other by the Maxwell's equations. For a non-magnetic and electrically neutral material, these equations are:

$$div\,\vec{D} = 0 \tag{3.2}$$

$$rot\,\vec{E} = -\frac{\partial \vec{B}}{\partial t} \tag{3.3}$$

$$div\,\vec{B} = 0 \tag{3.4}$$

$$rot\vec{H} = \vec{j} + \frac{\partial \vec{D}}{\partial t} \tag{3.5}$$

$\vec{J}$ represents the current density in the medium (including free and bound current). The $\vec{D}$ and $\vec{B}$ vectors are linked to the other fields by:

$$\vec{D} = \varepsilon \cdot \vec{E} = \varepsilon_0 \cdot \vec{E} + \vec{P} \tag{3.6}$$

$$\vec{B} = \mu_0 \cdot \vec{H} \tag{3.7}$$

with ε being the dielectric constant of the medium, ε_0 the permittivity of free space, μ_0 the permeability of free space and $\vec{P}$ the polarization density of the medium.

By applying the rotational operator to Equation (3.3) and introducing Equation (3.5), we obtain the propagation equation of the electric field in a non-magnetic and electrically neutral medium. If there is no current in the material ($\vec{J} = 0$), this equation becomes:

$$grad\ div\ \vec{E} - \nabla^2\vec{E} + \mu_0 \cdot \varepsilon_0 \cdot \frac{\partial^2\vec{E}}{\partial t^2} = -\mu_0 \cdot \frac{\partial^2\vec{P}}{\partial t^2} \tag{3.8}$$

For an isotropic and homogeneous medium, the dielectric constant ε is a constant and:

$$div\ \vec{D} = 0 \Rightarrow \varepsilon \cdot div\vec{E} = 0 \Rightarrow div\vec{E} = 0 \tag{3.9}$$

And Equation (3.8) provides:

$$\nabla^2\vec{E} = \mu_0 \cdot \varepsilon_0 \cdot \frac{\partial^2\vec{E}}{\partial t^2} + \mu_0 \cdot \frac{\partial^2\vec{P}}{\partial t^2} \tag{3.10}$$

A solution to Equation (3.10) for a plane electromagnetic wave can be expressed as:

$$\vec{E} = \vec{E}_0 \cdot e^{i(\omega \cdot t - \vec{k} \cdot \vec{z})} \tag{3.11}$$

where $\vec{E}_0$ is the amplitude of the $\vec{E}$ field, ω the angular frequency, $\vec{k}$ the wave vector and $\vec{z}$ the direction of propagation of the plane wave in an orthonormal basis.

The propagation equation can then be written as:

$$\nabla^2\vec{E} = -\mu_0 \cdot \omega^2 \cdot \varepsilon_T(\omega) \cdot \vec{E} \tag{3.12}$$

with the total dielectric or dielectric function of the medium being $\varepsilon(\omega) = \varepsilon_0 - i \cdot \sigma(\omega)/\omega$, where σ(ω) is the conductivity of the medium.

This Equation (3.12) is the propagation equation of an electromagnetic wave $\vec{E} = \vec{E}_0 \cdot e^{i(\omega \cdot t - \vec{k} \cdot \vec{z})}$ in a non-magnetic, electrically neutral, homogeneous, isotropic medium in the absence of current circulation.

We define the propagation speed v of the electromagnetic wave in this medium as:

$$v = \frac{1}{\sqrt{\mu_0 \cdot \varepsilon}} = \frac{\omega}{k} \tag{3.13}$$

It can also be written as:

$$v = \frac{1}{\sqrt{\mu_0 \cdot \varepsilon(\omega)}} = \frac{1}{\sqrt{\mu_0 \cdot \varepsilon_0} \cdot \sqrt{\frac{\varepsilon(\omega)}{\varepsilon_0}}} = \frac{c}{N(\omega)} \tag{3.14}$$

introducing the complex optical index of the medium N(ω):

$$N(\omega) = n_r(\omega) - i \cdot n_i(\omega) = \sqrt{\frac{\varepsilon(\omega)}{\varepsilon_0}} \tag{3.15}$$

n_r and n_i are the real and imaginary optical indices of the medium respectively.

The complex optical index compares the propagation speed of the wave in a medium v with the one of a wave in free space c. Due to the interactions of the wave with the medium, its propagation speed in lower than in free space. This complex optical index is the square root of the relative permittivity $\varepsilon_r(\omega)$ of the medium.

The general solution to Equation (3.12) can be expressed as function of the complex optical index as:

$$\vec{E} = \vec{E}_0 \cdot e^{-i \cdot \vec{k} \cdot \vec{z}} \cdot e^{i\omega t} = \vec{E}_0 \cdot e^{i(\omega \cdot t - \frac{\omega}{c} \cdot n_r \cdot z)} \cdot e^{-\frac{\omega}{c} \cdot n_i \cdot z} \tag{3.16}$$

The first exponential term represents the propagation of a wave at a c/n_r speed in the direction z. The second exponential term expresses the wave attenuation due to interactions with the medium.

The propagation of an electromagnetic wave in a medium can therefore be fully described by the complex optical index N(ω) of this medium.

By solving Equation (3.10) for the vector field $\vec{E}$ and its equivalent for $\vec{H}$ and with Maxwell's equations (3.2) to (3.5), we can conclude that:

- The $\vec{E}$ and $\vec{H}$ vectors are perpendicular to the propagation direction z, i.e. in the (x,y) plane
- The amplitudes of these two fields display a constant ratio, such as:

$$H_x = -\sqrt{\frac{\varepsilon_r}{\mu_0}} E_y \tag{3.17}$$

$$H_y = -\sqrt{\frac{\varepsilon_r}{\mu_0}} E_x \qquad (3.18)$$

As we have already explained that there is a constant relation between $\vec{E}$and $\vec{D}$ (Equation (3.6)) and $\vec{B}$and $\vec{H}$ (Equation (3.7)), we can fully describe an electromagnetic wave with its electric field $\vec{E}$ alone.

3.1.1.2 Propagation of a polarized electromagnetic wave [9,11]

An electromagnetic wave is modified by interacting with a medium. If we only consider the intensity I of $\vec{E}$ field, which is proportional to $|\vec{E}_0|$, these modifications only appear in the variations of the intensity. Considering the amplitude of the $\vec{E}$ field on the other hand displays much more complex modifications that require complex modeling, because of the polarization properties of the electromagnetic waves.

A light wave is said to be unpolarized when the temporal observation of its $\vec{E}$ field in a fixed point reveals a random behavior. If it's not random and the wave can be regarded as a monochromatic plane wave, it's called a totally polarized.

The electric field of a plane wave propagating along the z direction can be decomposed following the x and y axes:

$$\vec{E}(z,t) = E_x(z,t) \cdot \vec{x} + E_y(z,t) \cdot \vec{y} \qquad (3.19)$$

For a monochromatic wave, the components are given by:

$$E_x(z,t) = E_{0x}(z) \cdot cos(\omega \cdot t + \delta_x) \qquad (3.20)$$

$$E_y(z,t) = E_{0y}(z) \cdot cos(\omega \cdot t + \delta_y) \qquad (3.21)$$

where $E_{0x}(z)$ and $E_{0y}(z)$, δ_x and δ_y are the amplitudes and the phases of the electric field vector along the x and y axes, respectively.

The most generic polarization type of a wave is the elliptic polarization represented in Figure 3.4. If we omit the z and t variables for more clarity, the components are written:

$$E_x = E_{0x} \cdot cos(\omega \cdot t + \delta_x) \qquad (3.22)$$

$$E_y = E_{0y} \cdot cos(\omega \cdot t + \delta_x + \epsilon) \qquad (3.23)$$

ϵ is the phase difference between the two components.

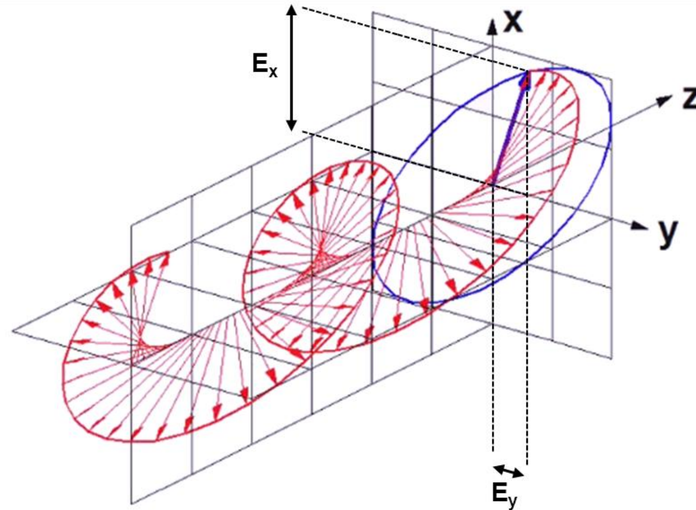

Figure 3.4: Elliptical polarization diagram

The trajectory of the extremity of the $\vec{E}$ vector is obtained by combining Equations (3.22) and (3.23) to eliminate the t parameter:

$$\left(\frac{E_x}{E_{0x}}\right)^2 + \left(\frac{E_y}{E_{0y}}\right)^2 - 2 \cdot \frac{E_x}{E_{0x}} \cdot \frac{E_y}{E_{0y}} \cdot \cos\epsilon = \sin^2\epsilon \qquad (3.24)$$

This is the equation of an ellipse, which means that at a fixed point, the extremity of the E vector describes during the time an ellipse in the plan perpendicular to the propagation direction of the light wave. This is the polarization state of a polarized light wave after reflecting on a sample.

3.1.1.3 Interaction of an electromagnetic wave with a sample [12]

When an electromagnetic wave is sent on a sample, a part of the wave is reflected and another part can be transmitted. Analyzing the modifications of the incident wave through reflection of transmission allows us to determine properties of the said sample. As we saw in section 3.1.1.1, these are fully described by the sample's complex optical index. This means that the observation of the modifications of an incident electromagnetic wave can provide us with a full characterization of the sample. In the case of ellipsometry, we focus our attention on the amplitude of the incident wave.

We consider an electromagnetic wave on a sample. It can be fully described by its electrical field $\vec{E}$(z,t) where t is the time variable and $\vec{z}$ the propagation direction of the incident wave. We decompose the electric field into a $\vec{p}$ component (parallel to the incident plane formed by

$\vec{z}$ and the normal direction of the sample's surface) and $\vec{s}$ component (perpendicular to the incident plane), as showed on Figure 3.5:

$$\vec{E}(z,t) = E_p(z,t) \cdot \vec{p} + E_s(z,t) \cdot \vec{s} \tag{3.25}$$

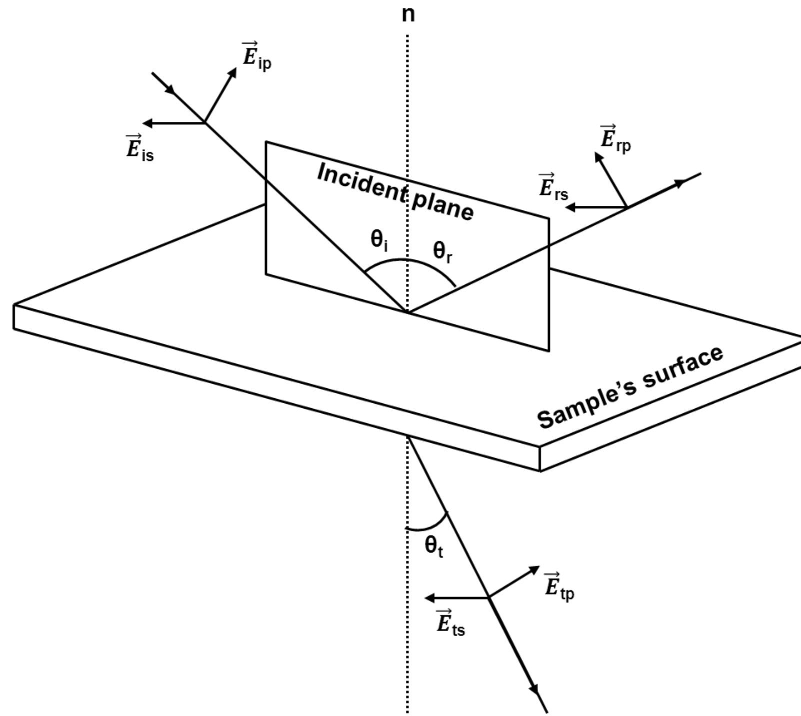

Figure 3.5: Definition of the reflected and transmitted electric fields for a sample

For a plane sinusoidal monochromatic wave, the E_p and E_s components are written:

$$E_p = |E_p| e^{i(\omega \cdot t + \varphi_p)} \tag{3.26}$$

$$E_s = |E_s| e^{i(\omega \cdot t + \varphi_s)} \tag{3.27}$$

where $|E_p|$, φ_p, $|E_s|$, φ_s are the amplitudes and phases of the p and s components respectively and ω is the angular frequency of the wave.

When considering the electric fields of the incident, reflected and transmitted waves $\vec{E}_i$, $\vec{E}_r$ and $\vec{E}_t$, we can similarly write:

$$\vec{E}_i(z,t) = E_{ip}(z,t) \cdot \vec{p} + E_{is}(z,t) \cdot \vec{s} \tag{3.28}$$

$$\vec{E}_r(z,t) = E_{rp}(z,t) \cdot \vec{p} + E_{rs}(z,t) \cdot \vec{s} \tag{3.29}$$

$$\vec{E}_t(z,t) = E_{tp}(z,t) \cdot \vec{p} + E_{ts}(z,t) \cdot \vec{s} \tag{3.30}$$

The components of each electric field are described by its amplitude and its phase. We define r_p and r_s as the complex reflection coefficients for the $\vec{p}$ and $\vec{s}$ components:

$$r_p = \frac{E_{rp}}{E_{ip}} = \frac{|E_{rp}|}{|E_{ip}|} \cdot e^{i(\varphi_{rp}-\varphi_{ip})} = |r_p| \cdot e^{i\delta_{rp}} \quad (3.31)$$

$$r_s = \frac{E_{rs}}{E_{is}} = \frac{|E_{rs}|}{|E_{is}|} \cdot e^{i(\varphi_{rs}-\varphi_{is})} = |r_s| \cdot e^{i\delta_{rs}} \quad (3.32)$$

with $|r_p|$ and $|r_s|$ the amplitude attenuations and δ_{rp} and δ_{rs} the phase differences due to reflection. We similarly define the complex transmission coefficients for the $\vec{p}$ and $\vec{s}$ components t_p and t_s:

$$t_p = \frac{E_{tp}}{E_{ip}} = \frac{|E_{tp}|}{|E_{ip}|} \cdot e^{i(\varphi_{tp}-\varphi_{ip})} = |t_p| \cdot e^{i\delta_{tp}} \quad (3.33)$$

$$t_s = \frac{E_{ts}}{E_{is}} = \frac{|E_{ts}|}{|E_{is}|} \cdot e^{i(\varphi_{ts}-\varphi_{is})} = |t_s| \cdot e^{i\delta_{ts}} \quad (3.34)$$

$|t_p|$ and $|t_s|$ are the amplitude attenuations and δ_{tp} and δ_{ts} the phase differences due to transmission.

While it's impossible to obtain the absolute phase of the electric fields, we can measure their phase difference; we can therefore define the complex reflection factor ρ:

$$\rho = \frac{r_p}{r_s} = \frac{|r_p|}{|r_s|} \cdot e^{i(\delta_{rp}-\delta_{rs})} = tan\,\Psi \cdot e^{i\Delta} \quad (3.35)$$

where $\tan\Psi$ represents the attenuation ratio of the two components of the electric field due to the reflection and Δ is the phase difference between the two components due to the reflection.

To obtain homogeneous values and as the phase difference Δ is an angle, we express the amplitudes attenuation ratio as the tangent of another angle, Ψ. The angles (Δ,Ψ) are measured by ellipsometry.

3.1.2 Modeling the optical response of a thin film on a substrate

We detailed in section 3.1.1.3 the phenomenological aspect of the interaction of an electromagnetic wave with a medium. We now present the model used to predict the optical behavior of a thin film deposited on a substrate that allows us to calculate theoretical values of (Δ,Ψ) from the physical properties of the thin film. We proved in paragraph 3.1.1.1 that these properties are contained within the complex optical index N for a homogeneous and isotropic medium. Said index can still vary within the sample due to the composition (related

to the indium incorporation in the GaN material) as well as the microstructure of the layer (thickness, roughness, interface).

3.1.2.1 Physical principle

In the optical domain, the interaction between an electromagnetic wave and a medium is generally considered from a macroscopic standpoint, without taking into account the discrete nature of matter. This interaction is calculated by solving the Maxwell's equations, as exposed in section 3.1.1.1. In the case of a homogeneous and smooth material, this resolution leads to the Fresnel theory of light reflection and transmission [13].

Physically, the interaction is interpreted as the diffraction of the incident wave by the electrons of each atom of the material, i.e. an interaction at the microscopic level. This calculation, although simple for an atom, becomes extremely complex when it comes to determining the global effect of the diffraction of all the electrons of all the atoms of a sample. This approach can only be solved in the case of periodically disposed atoms for the material [14] (i.e. crystals) and the reflection and transmission represent the collective result of the diffraction of the wave by the atoms of the sample.

The equivalence between the microscopic (diffraction) and macroscopic (Fresnel's theory) approaches has been demonstrated [15-17] and studies show that both methods give similar results [18].

We've established (Equation (3.16)) that the only macroscopic parameter characterizing the behavior of an electromagnetic wave in a medium is the evolution of its complex optical index as a function of the wavelength $(\omega) = n(\omega) - i \cdot k(\omega)$:

$$\vec{E} = \vec{E}_0 \cdot e^{i(\omega \cdot t - \frac{\omega}{c} \cdot n(\omega) \cdot z)} \cdot e^{-\frac{\omega}{c} \cdot k(\omega) \cdot z} \qquad (3.36)$$

3.1.2.2 Ideal thin films

a) Interface between two mediums [12]

We consider the propagation of an electromagnetic wave through a plane interface between two homogeneous and isotropic mediums, as shown in Figure 3.6.

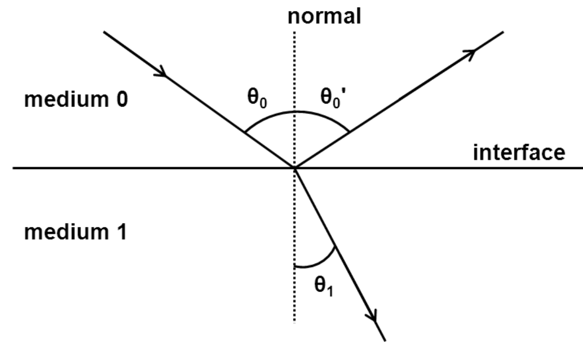

Figure 3.6: Reflection and transmission at an interface

The upper medium, noted 0, is characterized by a complex optical index $N_0 = n_0 - i \cdot k_0$ and the lower one, noted 1, by an index $N_1 = n_1 - i \cdot k_1$. The index change is supposed discontinuous at the interface.

At this interface, a part of the electromagnetic wave is being reflected and another part is transmitted. The boundary conditions at the interface for the components of the electric field $\vec{E}$ and the magnetic field $\vec{H}$ that are parallel to this interface require them to vary continuously on either of its sides. These conditions make the resolution of the Maxwell's equations possible in the mediums 0 and 1 and lead us to several conclusions [9-11]:

- The incident, reflected and transmitted beams are all in the same plane, called the incident plane. It also contains the normal to the surface.
- θ_0, θ_0' and θ_1 are the respective angles of incidence, reflection and transmission of the electromagnetic wave and are measured from the normal to the interface. These angles are related with each other through Snell-Descartes law:

$$\theta_0 = \theta_0' \quad (3.37)$$

$$N_0 \cdot sin\,\theta_0 = N_1 \cdot sin\,\theta_1 \quad (3.38)$$

- If the electric field of the incident beam is linearly polarized along the parallel (or perpendicular) direction to the plane of incidence, the reflected and transmitted fields will stay polarized along the same direction. It's because of this property that we decompose fields into the $\vec{p}$ and $\vec{s}$ components, as we can then work on either of these independently later on.
- We call (E_{ip}, E_{is}), (E_{rp},E_{rs}) and (E_{tp},E_{ts}) the complex amplitudes of the electric fields of the incident, reflected and transmitted waves. The boundary conditions lead to the

following values for the amplitude ratios of the different components of the beams (Equations (3.30) to (3.33)):

$$r_p = \frac{E_{rp}}{E_{ip}} = \frac{N_1 \cdot cos\,\theta_0 - N_0 \cdot cos\,\theta_1}{N_1 \cdot cos\,\theta_0 + N_0 \cdot cos\,\theta_1} \tag{3.39}$$

$$r_s = \frac{E_{rs}}{E_{is}} = \frac{N_0 \cdot cos\,\theta_0 - N_1 \cdot cos\,\theta_1}{N_0 \cdot cos\,\theta_0 + N_1 \cdot cos\,\theta_1} \tag{3.40}$$

$$t_p = \frac{E_{tp}}{E_{ip}} = \frac{2 \cdot N_0 \cdot cos\,\theta_0}{N_1 \cdot cos\,\theta_0 + N_0 \cdot cos\,\theta_1} \tag{3.41}$$

$$t_s = \frac{E_{ts}}{E_{is}} = \frac{2 \cdot N_0 \cdot cos\,\theta_0}{N_0 \cdot cos\,\theta_0 + N_1 \cdot cos\,\theta_1} \tag{3.42}$$

The complex reflection (r_p, r_s) and transmission (t_p, t_s) coefficients for polarizations p and s are also called Fresnel's coefficients.

b) Thin film on a semi-infinite substrate [12]

We consider now the case of the reflection and transmission of polarized light on a substrate covered with a thin film, as represented in Figure 3.7. The three mediums (ambiance, film and substrate) are homogeneous, isotropic and separated by smooth interfaces that are parallel with each other.

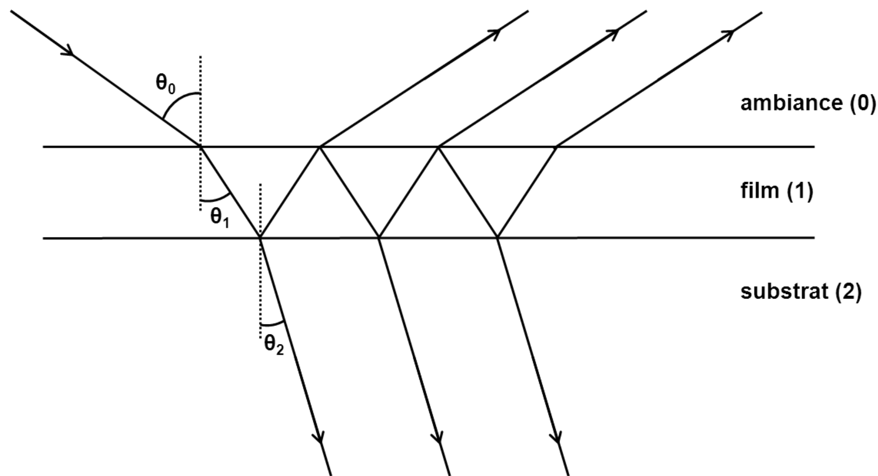

Figure 3.7: Reflection and transmission in a thin film on a substrate

We can observe that the incident light goes through a succession of reflections and transmissions at the different interfaces. The global reflection and transmission is the infinite sum of these elementary reflections and transmissions. We define for the p component the complex reflection and transmission coefficients as follows:

- r_{01p} is the complex reflection coefficient from the ambiance (0) to the film (1)
- r_{10p} is the complex reflection coefficient from the film (1) to the ambiance (0)
- r_{12p} is the complex reflection coefficient from the film (1) to the substrate (2)
- r_{21p} is the complex reflection coefficient from the substrate (2) to the film (1)
- t_{01p} is the complex transmission coefficient from the ambiance (0) to the film (1)
- t_{10p} is the complex transmission coefficient from the film (1) to the ambiance (0)
- t_{12p} is the complex transmission coefficient from the film (1) to the substrate (2)
- t_{21p} is the complex transmission coefficient from the substrate (2) to the film (1)

Each of these coefficients is calculated using Equations (3.39) to (3.42) at the relevant interface.

Each time a beam goes through the film, its phase is shifted of β, with:

$$\beta = 2 \cdot \pi \cdot \frac{d_1}{\lambda} \cdot N_1 \cdot \cos\theta_1 \qquad (3.43)$$

where d_1 is the film thickness.

With N_0, N_1 and N_2 the complex optical indices of the ambiance, the film and the substrate, we use the Snell-Descartes law to obtain the angles of incidence:

$$N_0 \cdot \sin\theta_0 = N_1 \cdot \sin\theta_1 = N_2 \cdot \sin\theta_2 \qquad (3.44)$$

The global reflection coefficient can be written as:

$$r_{pg} = r_{01} + t_{01} \cdot t_{10} \cdot r_{12} \cdot e^{-i \cdot 2 \cdot \beta} + t_{01} \cdot t_{10} \cdot r_{10} \cdot r_{12}^2 \cdot e^{-i \cdot 4 \cdot \beta} + \cdots$$

$$r_{pg} = \frac{r_{01p} + r_{12p} \cdot e^{-i \cdot 2 \cdot \beta}}{1 + r_{01p} \cdot r_{12p} \cdot e^{-i \cdot 2 \cdot \beta}} \qquad (3.45)$$

The global transmission coefficient is obtained similarly:

$$t_{pg} = t_{01} \cdot t_{12} \cdot e^{-i \cdot \beta} + t_{01} \cdot t_{12} \cdot r_{10} \cdot r_{12} \cdot e^{-i \cdot 3 \cdot \beta} + \cdots$$

$$t_{pg} = \frac{t_{01p} + t_{12p} \cdot e^{-i \cdot \beta}}{1 + r_{01p} \cdot r_{12p} \cdot e^{-i \cdot 2 \cdot \beta}} \qquad (3.46)$$

Equations (3.45) and (3.46) can be transposed to the s polarization case, and:

$$r_{sg} = \frac{r_{01s} + r_{12s} \cdot e^{-i \cdot 2 \cdot \beta}}{1 + r_{01s} \cdot r_{12s} \cdot e^{-i \cdot 2 \cdot \beta}} \qquad (3.47)$$

$$t_{sg} = \frac{t_{01s} + t_{12s} \cdot e^{-i \cdot \beta}}{1 + r_{01s} \cdot r_{12s} \cdot e^{-i \cdot 2 \cdot \beta}} \qquad (3.48)$$

The (r_{pg}, r_{sg}, t_{pg}, t_{sg}) coefficients are the global complex reflection and transmission coefficients for the ambiance-film-substrate system.

c) Stack of thin films on a semi-infinite substrate [12]

Adding multiple reflections inside a film quickly becomes impossible if the number of layers in the system increases. In this case, we have to use a matrix method.

A stack of m thin films is represented in Figure 3.8. The films are indexed from 1 to m, 0 is assigned to the ambiance and m+1 to the substrate. We still suppose that all the interfaces are smooth and parallel with discrete index changes, that the ambiance and the substrate are semi-infinite.

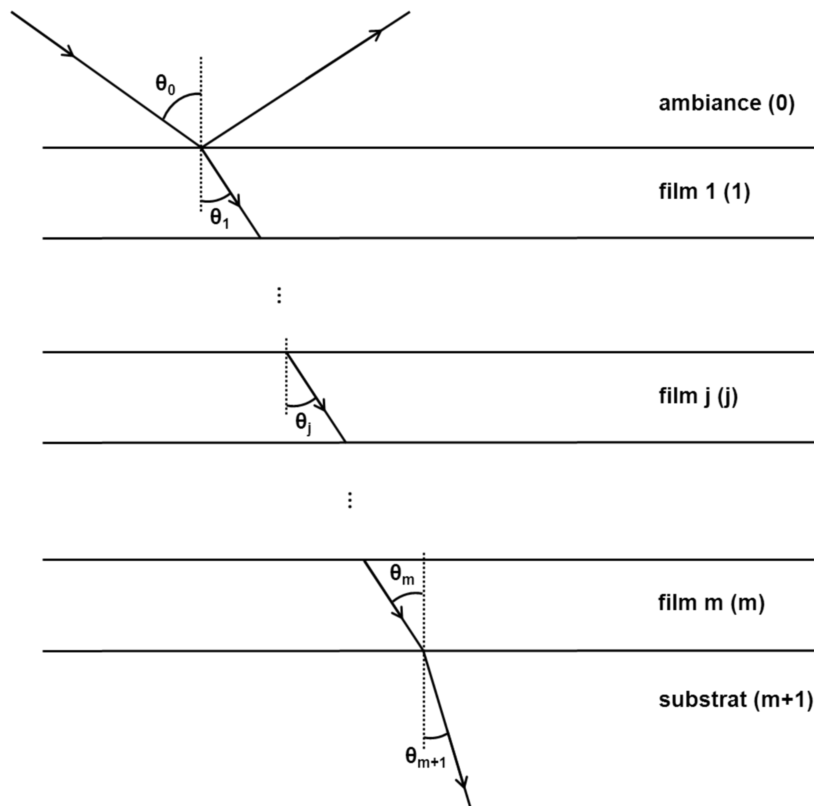

Figure 3.8: Reflection and transmission in a stack of thin films

This method is based on the principle that the interactions at an interface and inside a film are independent. We will lead the calculations for the p component but they are applicable to the s component as well, as we saw in the previous cases.

At each interface, the light wave is subject to reflection and transmission phenomena. We've already established that the relations between the electric fields on either side of the interface only depend on the complex reflection and transmission coefficients according to Equations (3.39) to (3.42). This can be translated into the matrix form:

$$\begin{bmatrix} E_{ip} \\ E_{rp} \end{bmatrix} = \begin{bmatrix} \frac{1}{t_p} & \frac{r_p}{t_p} \\ \frac{r_p}{t_p} & \frac{1}{t_p} \end{bmatrix} \cdot \begin{bmatrix} E_{tp} \\ 0 \end{bmatrix} \tag{3.49}$$

This matrix is called interface matrix I. In the general scenario from a film i to a film j, it's written:

$$I_{ijp} = \begin{bmatrix} \frac{1}{t_{ijp}} & \frac{r_{ijp}}{t_{ijp}} \\ \frac{r_{ijp}}{t_{ijp}} & \frac{1}{t_{ijp}} \end{bmatrix} \tag{3.50}$$

where the r_{ij} and t_{ij} coefficients are defined using Equations (3.39) to (3.42).

Snell-Descartes law is still used to link the relevant angles:

$$N_0 \cdot sin\,\theta_0 = N_1 \cdot sin\,\theta_1 = \cdots = N_j \cdot sin\,\theta_j = \cdots = N_m \cdot sin\,\theta_m = N_{m+1} \cdot sin\,\theta_{m+1} \tag{3.51}$$

While going through a film, the wave is also shifted with a phase difference β as defined in Equation (3.42), which leads to the definition of a layer matrix L. For the film j:

$$L_j = \begin{bmatrix} e^{i \cdot \beta_j} & 0 \\ 0 & e^{-i \cdot \beta_j} \end{bmatrix} \tag{3.52}$$

To obtain the global complex reflection and transmission coefficients, we now need to link the electric fields in the ambiance and in the substrate. We define the diffusion matrix S of the system:

$$\begin{bmatrix} E_{ip} \\ E_{rp} \end{bmatrix} = S \cdot \begin{bmatrix} E_{tp} \\ 0 \end{bmatrix} = \begin{bmatrix} S_{11p} & S_{12p} \\ S_{21p} & S_{22p} \end{bmatrix} \cdot \begin{bmatrix} E_{tp} \\ 0 \end{bmatrix} \tag{3.53}$$

As the modifications of the electric field while going through the m films is only depending on the interface and in-layer phenomena describes by the interface and layer matrices, S can be written as the product of the I_{ij} and L_j in the order of the stack:

$$S = I_{01} \cdot L_1 \cdot I_{12} \cdot L_2 \cdot \cdots \cdot I_{(j-1)j} \cdot L_j \cdot I_{j(j+1)} \cdot L_{(j+1)} \cdot \cdots \cdot I_{m(m+1)} \cdot L_{(m+1)} \tag{3.54}$$

The global complex reflection and transmission coefficients for a structure of m films are a function of only the diffusion matrix S and are determined by:

$$r_{pg} = \frac{E_{rp}}{E_{ip}} = \frac{S_{21p}}{S_{11p}} \qquad (3\ 55)$$

$$t_{pg} = \frac{E_{tp}}{E_{ip}} = \frac{1}{S_{11p}} \qquad (3.56)$$

Equations (3.55) and (3.56) are also applicable for the s component of the electric field, *mutatis mutandis*.

The global complex reflection and transmission coefficients are the fundamental quantities in the characterization of the optical behavior of a material. These parameters are the ones that are compared to experimental values measured by ellipsometry. The reflection factor defined in section 3.1.1 is simply the ratio of the global complex coefficients for the two polarization p and s:

$$\rho = \frac{r_{pg}}{r_{sg}} = tan\Psi \cdot e^{i \cdot \Delta} \qquad (3.57)$$

d) Stack of thin films on a finite substrate [20,21]

The model we presented in the previous paragraph for a structure of m layers is only applicable if the ambiance and the substrate are semi-infinite. It’s the case of the ambiance (generally air) but it doesn’t always hold true for the substrate. A substrate material that is sufficiently absorbing will ensure that there is no reflection on the back side of the substrate, but if the substrate is transparent or insufficiently absorbing, we need to consider the substrate as an extra layer that must be added to the structure.

As ellipsometry is a reflection technique, eliminating the reflection on the back side of the substrate also provides a solution to not have to take into account the effect of a reflection and consider the substrate semi-infinite.

3.1.2.3 Non-ideal thin films

Ideally, a thin film is modeled by a homogeneous film with a constant optical index at any point of the layer, separated from the ambiance and the substrate by discrete and parallel interfaces. In practice, the optical index can vary inside the film between the two interfaces that are not necessarily smooth and immediate. The physical causes are generally related to the growth process: variations in the crystal structure, variations of the composition, roughness, etc.

These non-ideal effects are separated into two categories, as depicted in Figure 3.9: non-homogeneity for small variations of the index inside the film and interface phenomena for the more important index variations due to the crossing from a medium to another.

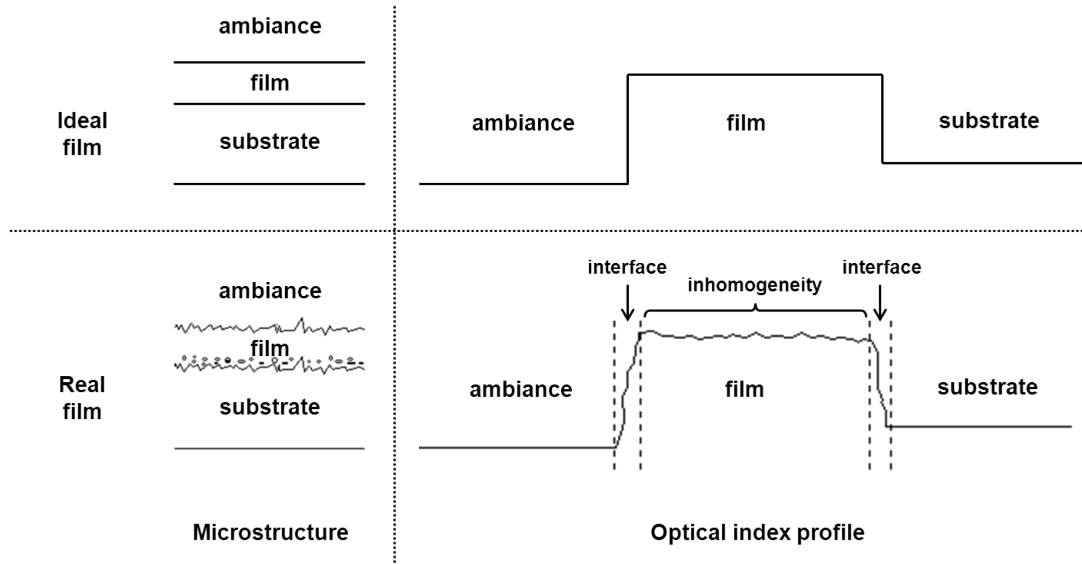

Figure 3.9: Microstructure and index profile for ideal and real films

a) Non-homogeneity

Non-homogeneity is a volumic phenomenon due to the variation of the film's optical index as a function of the depth. Solving propagation equations for a medium with a non-homogeneous index is not immediate and can be done using various approaches. Some studies solve the Maxwell's equations for a given index profile [13], others use the perturbation theory assuming small variations around a mean value [22-25]. We use a different method, decomposing the optical index profile into a stack of layers with constant indices whose values follow the real profile index, as presented in Figure 3.10.

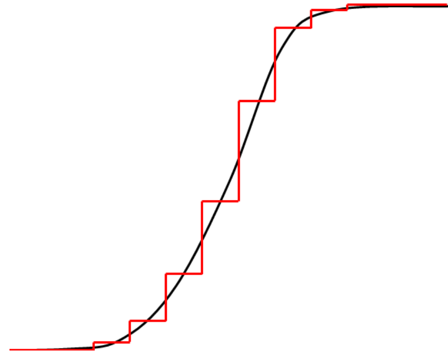

Figure 3.10: Decomposition of a non-homogeneous optical index profile into homogeneous films

The advantage of this method is that it transforms a single film with non-homogeneous index profile into a stack of films with homogeneous indices, which is the theoretical case we detailed in section 3.1.2.2 c).

This method is only applicable if the film is decomposed in a stack with a sufficient number of elementary layers. Studies find that decomposing a film in 0.8 nm-thick layers provides simulation results that are close enough to the real measurement to make the approximation stand.

b) Interface phenomena

There are two categories covered by non-ideal phenomena at the interfaces: roughness and interface diffusion.

Roughness designates the non-planarity of the separation between two mediums, which is characterized by the variation of the boundary between them around an average position (the median plane). At each point of the interface, the crossing from a medium to the other is discrete, only the position of the transition changes from a point of the surface to another. If the variation of the interface position is large compared to the wavelength of an incident light source, the beam is diffused in all the directions, not only in the specular direction of the median plane. For a beam with a sufficient size, the reflection depends on the mean positions of the illuminated surface, transforming the discrete index at the interface into a gradient of index.

Interface diffusion on the other hand is related to two materials inter-diffusing in each other at their interface, causing an index gradient along the normal direction [14,28]. We observe

that, although these two phenomena are fundamentally different, they are equivalent from an optical point of view, as displayed in Figure 3.11.

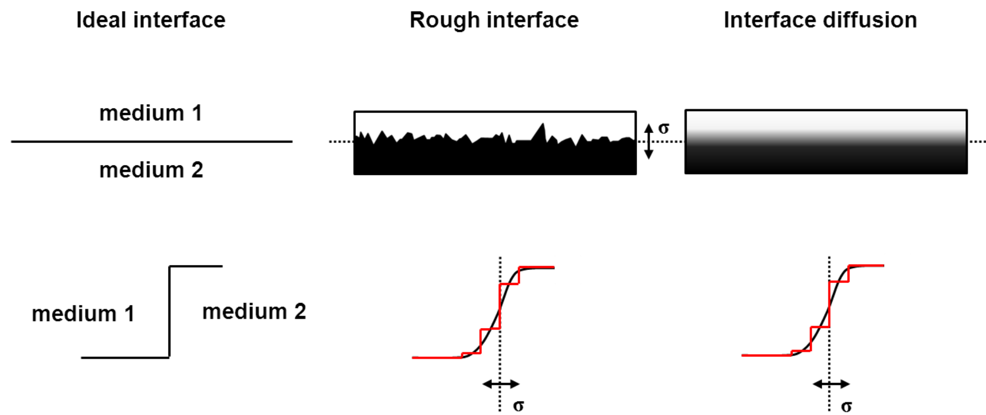

Figure 3.11: Profile indices of a smooth and a rough interface; equivalence with interface diffusion

Roughness is quantified by the RMS roughness σ defined as the square root of the average of the squared distance z_i of each point to the median plane along the normal direction [29]:

$$\sigma = \sqrt{\frac{\sum_{i=0}^{n} z_i^2}{n}} \tag{3.58}$$

As the distinction is not necessary, we will designate both phenomena as “roughness” in the rest of this study. For ellipsometry, roughness is usually modeled by introducing inter-layers composed of various compositions of the two mediums at the interface and using equations from paragraph 3.1.2.2 c).

As a conclusion, Figure 3.12 presents the typical shape of an index profile used for modeling the behavior of a thin film, considering the unique properties of InGaN materials, like rough surface and diffusion, as well as In composition gradient inside the layer.

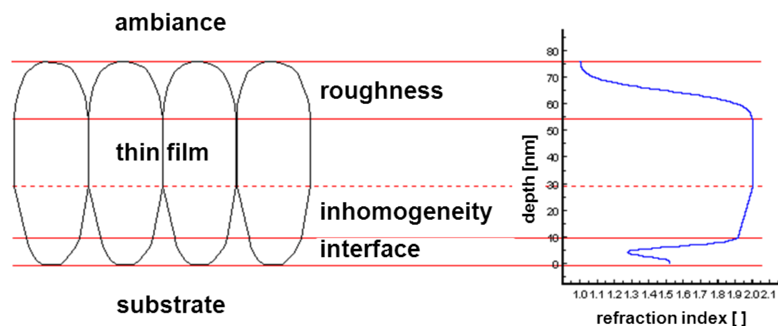

Figure 3.12: Schematic representation and profile index of a non-ideal thin film on a substrate

3.1.3 Measures analysis methodology

Realizing ellipsometry measurements for a sample provides experimental values of (Δ,Ψ), noted Δ_{exp} and Ψ_{exp}, as a function of the wavelength. Using the formalism introduced in section 3.1.2, it is possible to define a numerical model of the structure expressing theoretical values of (Δ,Ψ), noted Δ_{th} and Ψ_{th} as a function of the physical properties of the material and of the experimental conditions.

3.1.3.1 Definition and determination of the parameters of the model

For a thin film deposited on a substrate, we can classify the parameters in three categories:

- Parameters depending on the experimental conditions, who are fixed during the measuring operation:
  - the wavelength of the light beam λ
  - the incidence angle of the light beam AI
- Parameters related to the properties of the sample:
  - the ambiance complex optical index $N_A(\lambda) = n_A(\lambda) - i \cdot k_A(\lambda)$
  - the substrate complex optical index $N_S(\lambda) = n_S(\lambda) - i \cdot k_S(\lambda)$
  - the complex optical index of each elementary sub-layer i used in the model $N_i(\lambda) = n_i(\lambda) - i \cdot k_i(\lambda)$

$N_A(\lambda)$ and $N_S(\lambda)$ are usually known or can be independently determined. The $N_i(\lambda)$ are unknown.

- Parameters defining the structure of the sample:
  - the substrate thickness d_S
  - the thickness of the elementary sub-layers d_i
  - a number of other parameters p_k for the different sub-layers of the model, such as roughness, porosity, interface diffusion, etc.

The model we chose defines (f_1,f_2), the relations between (Δ,Ψ) and these parameters:

$$\Delta_{th}(\lambda, AI) = f_1(\lambda, AI, N_A(\lambda), N_S(\lambda), d_S, N_i(\lambda), d_i, p_k) \quad (3.59)$$

$$\Psi_{th}(\lambda, AI) = f_2(\lambda, AI, N_A(\lambda), N_S(\lambda), d_S, N_i(\lambda), d_i, p_k) \quad (3.60)$$

It is technically always possible to obtain at least as many parameters as independent measurements, so that there is always a solution to this system. We can then solve the inverse

problem to find out the parameters that lead to desired values of (Δ,Ψ). It is desirable to be in the case of an overdetermined equation system to reduce the statistical error on measurements.

Fitting (Δ_{th},Ψ_{th}) to $(\Delta_{exp},\Psi_{exp})$ is accomplished by minimizing the following mean-square deviation:

$$\chi^2 = \frac{1}{2\cdot N-P}\cdot\left[\sum_{i=1}^{N}\left(\frac{\cos\Delta_{exp\,i}-\cos\Delta_{th\,i}}{\varepsilon\cos\Delta_{exp\,i}}\right)^2+\sum_{i=1}^{N}\left(\frac{\tan\Psi_{exp\,i}-\tan\Psi_{th\,i}}{\varepsilon\tan\Psi_{exp\,i}}\right)^2\right] \quad (3.61)$$

where N is the number of data points, P is the number of model parameters to be determined, $\cos\Delta_{\exp i}$ and $\tan\Psi_{\exp i}$ are the measured $\cos\Delta$ and $\tan\Psi$ values while $\cos\Delta_{\text{th}\,i}$ and $\tan\Psi_{\text{th}\,i}$ are their calculated values from the model. $\varepsilon\Delta_i$ and $\varepsilon\Psi_i$ are the experimental errors in $\Delta_{exp\ i}$ and $\Psi_{exp\ i}$.

Minimization is performed using a modified version of the Levenberg-Marquardt algorithm [29]. The closer χ^2 is to 1, the better the theoretical values of (Δ,Ψ), and with them the parameters of the model, explain the measurements.

3.1.3.2 Regularization

The method for determining the different parameters of the model we introduced in the previous paragraph is a typical mathematical inverse problem, which consists in determining experimentally inaccessible causes from the observation and modeling of their effects. While mathematically correct, this approach doesn't account for the fact that several causes may produce similar results. The current model we use defines n and k as the fitting parameters for each wavelength, which results in a system with 2 × (number of wavelengths) variables for each elementary sub-layer and solving the problem by minimizing the χ^2 provides noisy results that sometimes don't have a physical sense. For this reason we use a mathematical technique called regularization that consists in adding constrains on our material so that we can reduce the overall number of variables in our equation system [30,31]. In our case, we work on the dielectric function model.

$$\varepsilon = \varepsilon_1 - i\cdot\varepsilon_2 \quad (3.62)$$

There are many dielectric function models, and we need to select an appropriate model according to the optical properties of the sample. For dielectric function modeling in a transparent region ($\varepsilon_2 \approx 0$), the Sellmeier or Cauchy models are used [32,33]. When there is

free-carrier absorption, the data analysis is generally performed using the Drude model [34]. To express the electric polarization in the visible/UV region, various models have been used, including the Tauc–Lorentz dispersion law detailed by *Jellison et al.* in 1996 and widely accepted and used since then [35]. It defines the imaginary part of the dielectric function for photon energy above the band edge as:

$$\varepsilon_2(E) = 2 \cdot n(E) \cdot k(E) = \frac{A \cdot E_0 \cdot \Gamma \cdot (E - E_g)^2}{E \cdot \left[(E^2 - E_g^2)^2 + \Gamma^2 \cdot E^2 \right]} \cdot \Theta(E - E_g) \qquad (3.63)$$

where A and Γ represent the amplitude and broadening of the ε_2, E_0 is the peak transition energy and E_g is the bandgap energy. $\Theta(E-E_g)$ is the Heavyside function ($\Theta(E) = 1$ for $E \geq 0$ and $\Theta(E) = 0$ for $E < 0$). The real part of the Tauc-Lorentz dielectric function is obtained by performing a Kramers-Kronig integration of $\varepsilon_2(E)$:

$$\varepsilon_1(E) = \varepsilon_1(\infty) + \frac{2}{\pi} \cdot \mathcal{P} \int_{E_g}^{\infty} \frac{\zeta \cdot \varepsilon_2(\zeta)}{\zeta^2 - E^2} d\zeta \qquad (3.64)$$

$\mathcal{P}$ stands for the Cauchy principal part of the integral and an additional parameter $\varepsilon_1(\infty)$ has been included. Normally, $\varepsilon_1(\infty) = 1$, but it can be greater if there is a significant optical transition at an energy greater than is sampled by the ellipsometer. The integral is exactly evaluated by Jellison.

We can now reduce 2 × (number of wavelengths) variables with the parameterization to 4 fitting terms: A, Γ, E_0 and E_g. As any parametric law, it also provides much smoother index dispersion.

3.2 Experimental study of InGaN thin films

The ellipsometry measurements are realized at IEMN on a HORIBA JOBIN YVON UVISEL spectroscopic ellipsometer. It's an automated ellipsometer that provides us with values of (Δ,Ψ) in the visible and near-infrared domains, namely between 4.55 eV (~ 270 nm) and 0.75 eV (~ 1650 nm). The measurements are performed at an angle of incidence of 60°. The model used to extract the optical indices, described in the previous paragraph, is developed by Eric Dumont [29,36] in the framework of a collaboration with the University of Mons, Belgium and is based on Jellison's work [35,37].

We first examine the GaN-on-sapphire template to compare the values with the ones we obtained previously through prism coupling, and then measure the InGaN monolayer samples we described in Chapter 2.

3.2.1 Experimental study of a GaN thin film

We start our analysis with a GaN sample to compare ellipsometric results with the ones we obtained through prism coupling in Figure 3.2. The sample is composed of a 2 µm-thick GaN layer on top of the GaN-on-sapphire template we described earlier.

Figure 3.13 shows the values of cos(Δ) and tan(Ψ) measured by spectroscopic ellipsometry and their best numerical fit through simulation. The agreement is excellent, suggesting that the model provides an accurate representation of the GaN thin film.

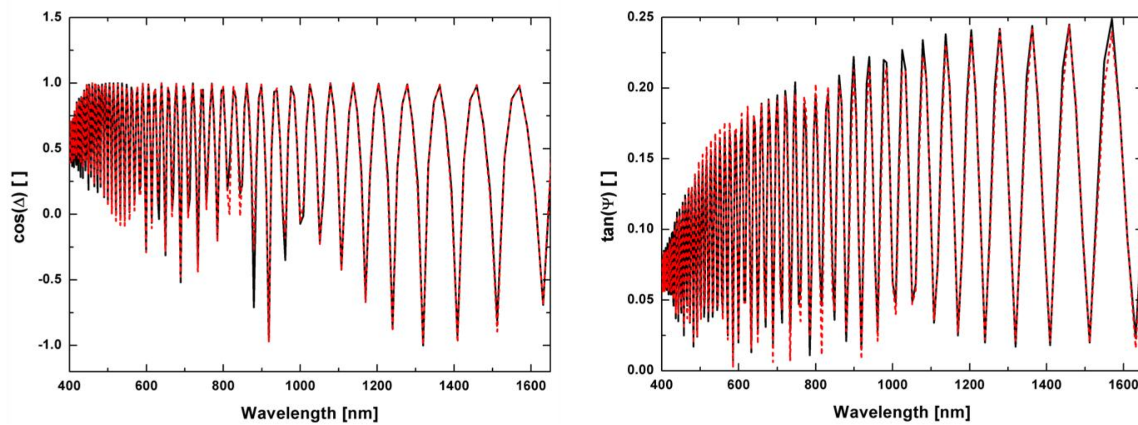

Figure 3.13: Spectroscopic ellipsometry cos(Δ) (left) and tan(Ψ) (right) results showing the experimental data (black plain lines) and the best numerical fit (red dotted line) for GaN

The corresponding values of the parameters and the Tauc-Lorentz model detailed in paragraph 3.1.3.2 lead to the reconstruction of the refractive index n and extinction coefficient k presented in Figures 3.14.

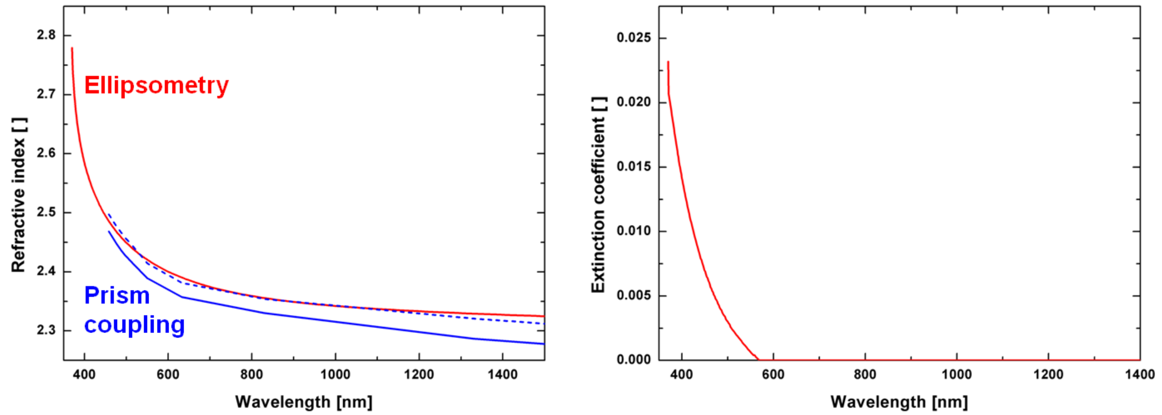

Figure 3.14: Extracted values (red) of refractive index (left) and extinction coefficient (right) for GaN with comparative results from prism coupling (blue) along s (plain) and p (dotted) polarizations

The values measured by prism coupling are slightly lower than the ellipsometry ones due the void that exists in the structure. As the index of air is lower than the one of gallium nitride, the average measurements are underestimated. Similarly, the difference between the values measured along the $\vec{p}$ and $\vec{s}$ polarizations can be explained by the anisotropy of the material structure. We made the approximation for ellipsometry that the layers were isotropic. The refractive index difference between the ordinary and extraordinary values is around ±0.03, very close to the margin of error of ellipsometry for GaN, ±0.02

If we compare these values with the ones reported in the literature and presented in Figure 3.2, the agreement is good, validating the model and method used. The low extinction coefficient suggests the quasi-transparency of the sample, which can be observed *de visu* in the visible range. Due to the Heavyside function in the Tauc-Lorentz model, k = 0 for wavelengths above 568 nm.

The index profile that was used in the best numerical fit is shown on Figure 3.15 for wavelengths of 458 nm and 633 nm. As we could expect from the index dispersion from Figure 3.14, the index decreases with the wavelength. The roughness is represented using a single elementary sub-layer while the interface diffusions can be observed at depth around 4.5 µm. Voids and interface defects also appear at the junction of the GaN layer and the GaN-on-sapphire template at 2.3 µm, as shown by the decreased index in the interfacial regions.

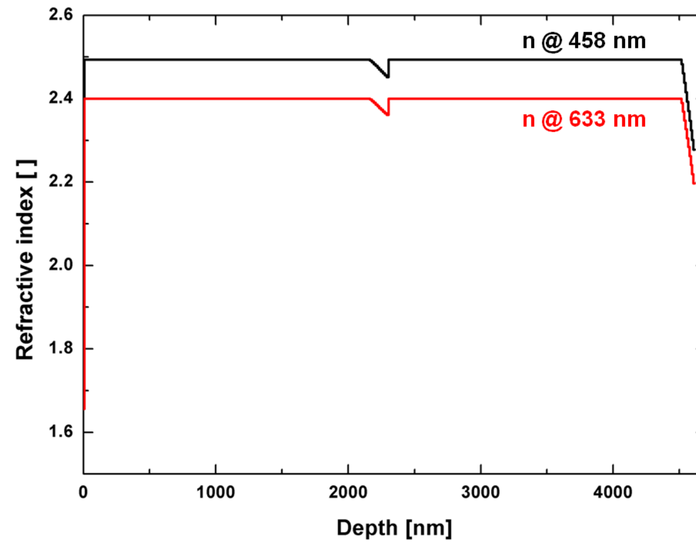

Figure 3.15: Index profiles for the best numerical fits for GaN at 458 nm (black) and 633 nm (red)

3.2.2 Experimental study of InGaN thin films

Similar experiments were carried out for the InGaN-1, InGaN-2 and InGaN-3 samples (see descriptions in chapter 2). We were not able to characterize the InN sample, which presents too weak oscillations of (cos(Δ),tan(Ψ)) and a structure that proves too difficult to model (due to the uncertainty of the composition of the $In_{0.3}Ga_{0.7}N$ interlayer) to obtain reliable results.

The values of the ellipsometry measurements and the best numerical fit are displayed in Figure 3.16 for sample InGaN-2.

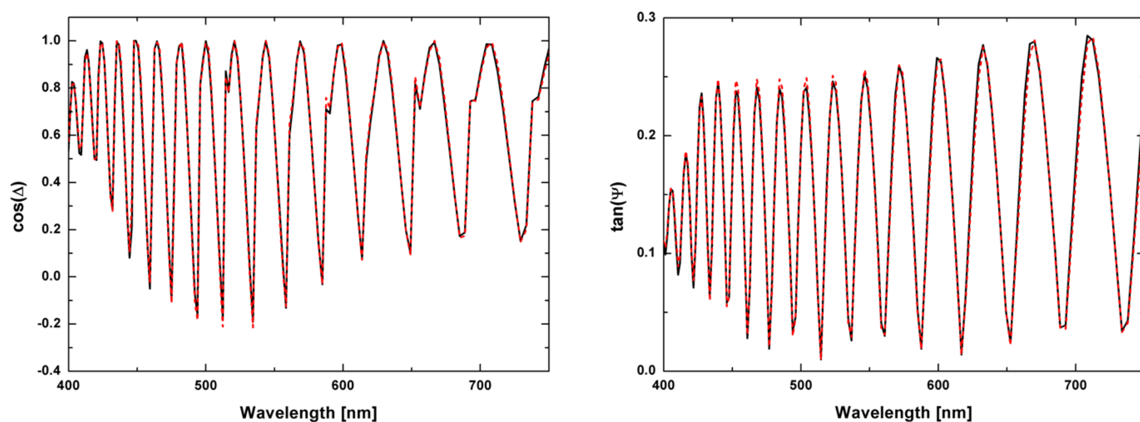

Figure 3.16: Spectroscopic ellipsometry cos(Δ) (left) and tan(Ψ) (right) results showing the experimental data (black plain lines) and the best numerical fit (red dotted line) for InGaN

The best fit is obtained for sample InGaN-1 with χ^2 = 4.23 and the errors in the values for the $In_xGa_{1-x}N$ samples is ±0.05 and ±0.01 for the refractive index and extinction coefficient, respectively. These optical indices are reported on Figure 3.17:

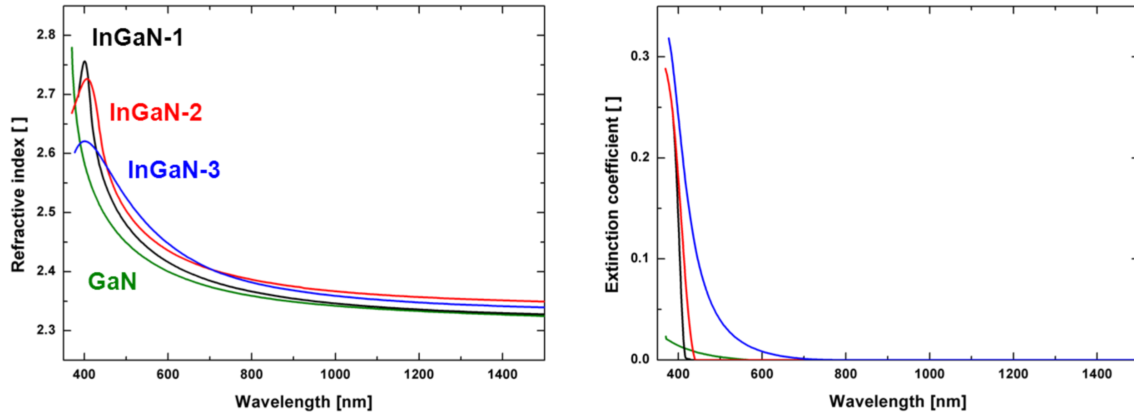

Figure 3.17: Extracted values of refractive index (left) and extinction coefficient (right) for samples InGaN-1 (black), InGaN-2 (red), InGaN-3 (blue) and GaN (green)

The refractive indices of $In_xGa_{1-x}N$ are larger than GaN over the frequency range between 400 nm and 1500 nm. Bandgap-related feature at ~ 400 nm (3 eV) is strongly pronounced in all the $In_xGa_{1-x}N$ samples and is shifted to higher frequencies as compared to GaN, in accordance with the micro-PL observations we made in paragraph 2.2.1.3.

The gap structure is broader in case of InGaN-3, possibly due to the increased alloy scattering and small compositional fluctuations as explained earlier and also reported by *Goldhahn et al.* [3] for cubic $In_{0.02}Ga_{0.98}N$ and $In_{0.07}Ga_{0.93}N$ samples. The inhomogeneity in the InGaN-3 sample is also seen as a reason for the decrease in the refractive index as compared to InGaN-1 and InGaN-2 as a higher In composition leads to higher v-pits density (as seen in the TEM images from section 2.2.1.1). It's also responsible for the Urbach tail observed in the extinction coefficient spectra of InGaN-3, resulting in a lower refractive index value [38]. The Urbach tail can be attributed to a number of mechanisms including the presence of point defects, disordered structure, excitonic transitions, or the presence of inhomogeneous strain in the semiconductor [39].

The band gap values can also be determined in all the samples from the extinction coefficient curve. The curves of $In_xGa_{1-x}N$ samples shift to the higher frequency (i.e. lower energy) side as the indium composition increases, resulting in lower bandgap energy, in agreement with the theoretical Equations of paragraph 1.1 and measurements of section 2.2.1.3.

InGaN-1 and InGaN-2 show sharp turning points at 416 nm and 441 nm in the extinction curve respectively while InGaN-3 sample has the broadest damping stretched to around 650 nm (Urbach tail). There is a slight discrepancy with the room temperature micro-PL spectra reported in chapter 2, but values are pretty consistent and we can observe in both cases the broad emission from 400 nm to 600 nm of the InGaN-3 sample.

The index profile, such as the InGaN-2 one displayed in Figure 3.18, provides further information on the structure used in the numerical model. We deduce an InGaN layer thickness of 175 nm and a GaN layer thickness of 2.27 µm, to compare with 180 nm and 2.2 µm respectively, otherwise reported in chapter 2.

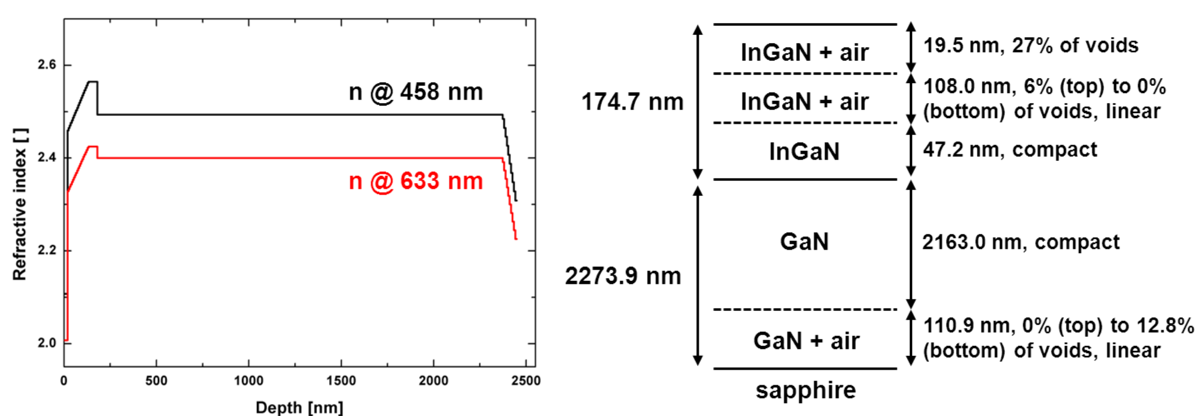

Figure 3.18: Index profiles for the best numerical fits (left) at 458 nm (black) and 633 nm (red) and layer structure (right) for sample InGaN-2

In summary, the model developed to simulate the interaction of polarized light with a medium has led us to determine the structural and optical properties of a set of GaN and InGaN thin films. The results are coherent with the other characterization experiments reported in chapter 2 and provide very valuable information as we extract the refractive index and extinction coefficient by obtaining a best fit for the ellipsometric measurements. It is also the first time that optical index is reported for $In_xGa_{1-x}N$ with $x > 0.07$, which constitutes a significant progress in the development on the InGaN growth and characterization front. The emergence of a line of InGaN-based optoelectronic components is still limited by the ability of researchers to grow high-indium InGaN layers, but the methodology has proven its reliability and can be used further on as new InGaN samples are fabricated.

References

[1] M. Anani, H. Abid, Z. Chama, C. Mathieu, A. Sayede and B. Khelifa, "$In_xGa_{1-x}N$ refractive index calculations", *Microelectron. J.* **38**, 262-266 (2007)

[2] N.A. Sanford, A. Munkholm, M. Krames, A. Shapiro, I. Levin, A. Davydov, S. Sayan, L. Wielunski and T. Madey, "Refractive index and birefringence of $In_xGa_{1-x}N$ films grown by MOCVD", *Phys. Stat. Sol. C* **2**, 2783-2786 (2005)

[3] R. Goldhahn, J. Scheiner, S. Shokhovets, T. Frey, U. Kohler, D.J. As and K. Lischka, "Refractive index and gap energy of cubic $In_xGa_{1-x}N$", *Appl. Phys. Lett.* **76**, 291-293 (2000)

[4] P.K. Tien, R. Ulrich and R.J. Martin "Modes of propagating light waves in thin deposited semiconductor films", *Appl. Phys. Lett.* **14**, 291-294 (1969)

[5] R. Ulrich and R. Torge. "Measurement of thin film parameters with a prism coupler", *Appl. Opt.* **12**, 2901-2908 (1973)

[6] A. Stolz, E. Cho, E. Dogheche, Y. Androussi, D. Troadec, D. Pavlidis and D. Decoster, "Optical waveguide loss minimized into gallium nitride based structures grown by metal organic vapor phase epitaxy", *Appl. Phys. Lett.* **98**, 161903 (2011)

[7] A. Chowdhury, H.M. Ng, M. Bhardwaj and N.G. Weimann. "Second-harmonic generation in periodically poled GaN", *Appl. Phys. Lett.* **83**, 1077-1079 (2003)

[8] S. Pezzagna, J. Brault, M. Leroux, J. Massies and M. de Micheli. "Refractive indices and elasto-optic coefficients of GaN studied by optical waveguiding", *J. Appl. Phys.* **103**, 123112 (2008)

[9] M. Born and E. Wolf, *Principles of Optics (7th Edition)*, Pergamon Press, Oxford (1999)

[10] A. Vasicek, *Optics of Thin Films*, North-Holland, Amsterdam (1960)

[11] E. Hecht and A. Zajac, *Optics (4th Edition)*, Addison-Wesley, Reading (2002)

[12] R.M. Azzam and N.M. Bashara, *Ellipsometry and Polarized Light (3rd Edition)*, North-Holland, Amsterdam (1987)

[13] J. Lekner, *Theory of Reflection*, Martinus Nijhoff, Dordrecht (1987)

[14] M.A. Omar, *Elementary Solid State Physics: Principles and Applications (4th Edition)*, Addison-Wesley, Reading (1994)

[15] S.K. Sinha, E.B. Sirota, S. Garoff and H.B. Stanley, "X-ray and neutron scattering from rough surfaces", *Phys. Rev. B* **38**, 2297-2311 (1988)

[16] D.G. Stearns, "X-ray scattering from interfacial roughness in multilayer structures", *J. Appl. Phys.* **71**, 4286-4299 (1992)

[17] W. Schommers, J. Als-Nielsen and P. Blanckenhagen, *Structure and Dynamics of Surfaces: Phenomena, Models, and Methods*, Springer, Berlin (1987)

[18] H. Fearn, D.F.V. James and P.W. Milonni, "Microscopic approach to reflection, transmission and Ewald-Oseen extinction theorem", *Am. J. Phys.* **64**, 986-995 (1996)

[19] H.M. Liddell and H.G. Jerrard, *Computer-aided Techniques for the Design of Multilayer Filters*, Institute of Physics Publishing, London (1981)

[20] P.H. Berning, "Theory and calculations of optical thin films", *Physics of Thin Films*, Vol. 1, Academic Press, New-York (1963)

[21] J.C. Charmet and P.G. de Gennes, "Ellipsometric formulas for an inhomogeneous layer with arbitrary refractive-index profile", *J. Opt. Soc. Am.* **73**, 1777-1784 (1983)

[22] B. Dugnoille and O. Virlet, "Optical profile of surface layers on a float glass determined by ellipsometry", *Appl. Opt.* **33**, 5853-5858 (1994)

[23] M. Kildemo, O. Hunderi and B. Drévillon, "Approximation of reflection coefficients for rapid real-time calculation of inhomogeneous films", *J. Opt. Soc. Am. A* **14**, 931-939 (1997)

[24] A.V. Tikhonravov, M.K. Trubetskov and A.V. Krasilnikova, "Spectroscopic ellipsometry of slightly inhomogeneous nonabsorbing thin films with arbitrary refractive-index profiles: theoretical study", *Appl. Opt.* **37**, 5902-5911 (1998)

[25] E. Toussaere and J. Zyss, "Ellipsometry and reflectance of inhomogeneous and anisotropic media: a new computationally efficient approach", *Thin Solid Films* **234**, 432-438 (1993)

[26] S.Y. Kim, “Numerical calculation of ellipsometric spectra of layers with arbitrary refractive index profiles”, *Opt. Eng.* **32**, 88-93 (1993)

[27] E. Chason and T.M. Mayer, “Thin film and surface characterization by specular X-ray reflectivity”, *Critical Reviews in Solid State and Materials Sciences* **22**, 1-67 (1997)

[28] J.M. Bennett and L. Mattsson, *Introduction to Surface Roughness and Scattering (2nd Edition)*, Optical Society of America, Washington D.C. (1999)

[29] E. Dumont, B. Dugnoille and S. Bienfait, “Simultaneous determination of the optical properties and of the structure of rf-sputtered ZnO thin films”, *Thin Solid Films* **353**, 93-99 (1999)

[30] H.D. Bui, *Inverse Problems in the Mechanics of Materials: An Introduction*, CRC Press, Boca Raton (1994)

[31] A.N. Tikhonov, V.Y. Arsenin, *Solutions of Ill-Posed Problems*, Winston, Washington D.C. (1977)

[32] W. Sellmeier, “Zur Erklärung der abnormen Farbenfolge im Spectrum einiger Substanzen”, *Ann. Phys.* **219**, 272-282 (1871)

[33] F.A. Jenkins and H.E. White, *Fundamentals of Optics (4th Edition)*, McGraw-Hill, Inc. New York City (1981)

[34] P. Drude, “Zur Elektronentheorie der Metalle”, *Ann. Phys.* **306**, 566-613 (1900)

[35] G.E. Jellison and F.A. Modine, “Parameterization of the optical functions of amorphous materials in the interband region”, *Appl. Phys. Lett.* **69**, 371-373 (1996); ibid. **69**, 2137 (1996)

[36] E. Dumont, *Caractérisation par Techniques Optiques de la Microstructure de Couches Minces d’Oxyde de Zinc non Homogènes Déposées dur Verre*, PhD thesis, University of Mons (2000)

[37] G.E. Jellison Jr., “Spectroscopic ellipsometry data analysis: measured versus calculated quantities”, *Thin Solid Films* **313–314**, 33 (1998)

[38] F. Natali, F. Semond, J. Massies, D. Byrne, S. Laügt, O. Tottereau, P. Vennéguès, E. Dogheche and E. Dumont, “Correlation between threading dislocation density and the

refractive index of AlN grown by molecular-beam epitaxy on Si(111)”, *Appl. Phys. Lett.* **82**, 1386-1388 (2003)

[39] A. Cremades, L. Görgens, O. Ambacher, M. Stutzmann and F. Scholz, “Structural and optical properties of Si-doped GaN”, *Phys. Rev. B* **61**, 2812–2818 (2000)

Chapter 4
Optical characterization of InGaN thin films in the terahertz domain

4. CHAPTER 4 OPTICAL CHARACTERIZATION OF INGAN THIN FILMS IN THE TERAHERTZ DOMAIN 89

4.1 THE TERAHERTZ TIME-DOMAIN SPECTROSCOPY 91

4.1.1 Single layer 93

4.1.1.1 For optically thick samples 94

4.1.1.2 For optically thin samples 94

4.1.2 Thin film on a substrate 95

4.2 EXPERIMENTAL STUDY OF INGAN THIN FILMS 97

4.2.1 Experimental study of a GaN thin films 98

4.2.2 Experimental study of InGaN thin films 100

REFERENCES 104

The terahertz (THz) frequency range lies from 0.3 THz to 10 THz, which corresponds to wavelengths between 1 mm and 30 µm. First known as the far infrared range, it is an exceptionally underused domain of the electromagnetic spectrum (also called the “THz gap”) as electronic and optic approaches are not able to reach it. The frequency performances of current transistors are limited by carrier transit times and capacitive effects while for lasers, sub-millimeter and millimeter waves remain a challenge due to the small difference in energy levels that are at play.

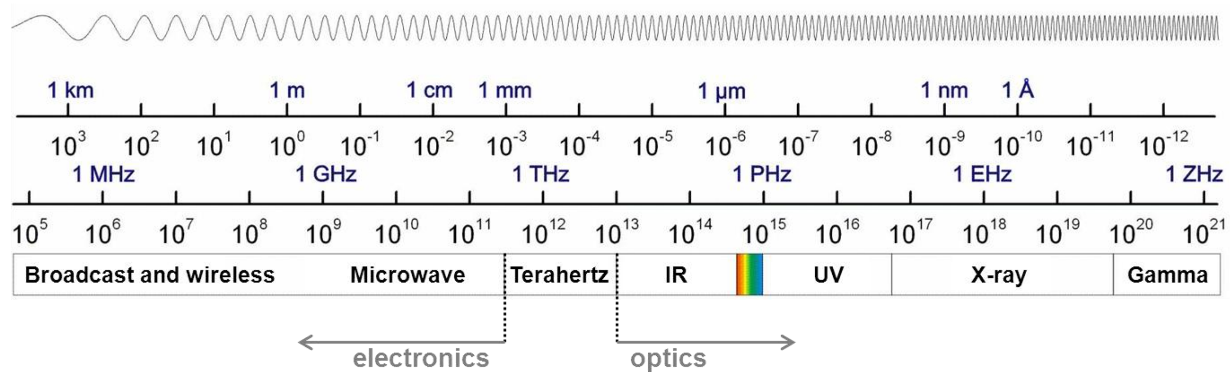

Figure 4.1: The "THz gap"

Nevertheless, THz radiations have a great number of potential applications in several domains: high-resolution spectroscopy in physics (for study of electron dynamics, interaction with phonons, impurities, etc.), in chemistry (gas detection, pollution and environment control, study of chemical reactions), in astronomy (detection of gas, atoms and ionized molecules), in telecommunications (wireless and broadband networks, short range networks, radars), in industrial imaging (materials, devices and systems controlling), in medicine (detection of caries, oncology), in biology (water detection, food industry) or in security (detection of weapons and dangerous materials). Therefore the realization of devices able to operate at these frequencies represents a great challenge. At present, the main bottleneck is the lack of efficient sources and detectors and there is a huge international effort to develop low-cost, reliable, compact and tunable sources, able to operate continuously at ambient (or near-ambient) temperature and compatible with the standard technologies to achieve easy integration in complex systems and circuits [1].

The III-nitride family is a very promising system, thanks to their many excellent electron transport properties, such as good mobility and high saturation drift velocity [2-4] that could

provide large amplitude of the transient current. In addition, the III-nitrides exhibit LO-phonon energies around 90 meV, which means that the onset of thermally-activated LO-phonon emission that leads to a breakdown in device performance in terahertz quantum cascade lasers would occur at much higher temperature than in current GaAs-based models and even suggest that room-temperature terahertz lasing may be feasible with III-nitrides structures. [5-9]

As in the visible domain, the knowledge of the fundamental optical and electrical properties of the material is a critical step. However, while there are some reports on the properties of GaN at such high frequencies [10-13], it's barely the case for InN [14] and literature on InGaN properties in the THz range is still inexistent.

Terahertz time-domain spectroscopy (THz-TDS) is a powerful and fast technique to measure the complex optical index of a material over a broad range of frequency.

4.1 The terahertz time-domain spectroscopy [15]

Terahertz time-domain spectroscopy is a non-destructive optoelectronic method for materials studies over a wide range of frequency which extends from a few tens of gigahertz to a few terahertz. It gives access to complex intrinsic parameters (refractive index, absorption, permittivity, conductivity), of a variety of materials such as dielectrics [16], semiconductors [17] and liquids [18]. It also allows following the dynamics of ultra-fast charge carriers in semiconductors and carrier-phonon interactions [19].

The THz-TDS technique is based on recording the time dependence of the electric field of a short electromagnetic pulse transmitted through a sample. Unlike common optical spectroscopy, which only measures the intensity of light at specific frequencies, the THz-TDS directly captures the electric field of the temporal THz wave and Fourier transformations of this time-domain data provides the amplitude and phase of the pulse. The ratio of the Fourier transforms of the signals collected with and without the sample yields the complex transmission coefficient of the sample in the frequency domain, therefore providing the real and imaginary parts of the optical index of the material, as well as its dielectric and conductivity functions, avoiding the uncertainty caused by the Kramers-Kronig analysis [20].

Figure 4.2 shows schematically the set-up for THz-TDS measurements; two temporal waves are measured (Figure 4.3) with and without the sample, their characteristic electric fields are noted $E_0(t)$ and $E_1(t)$ respectively.

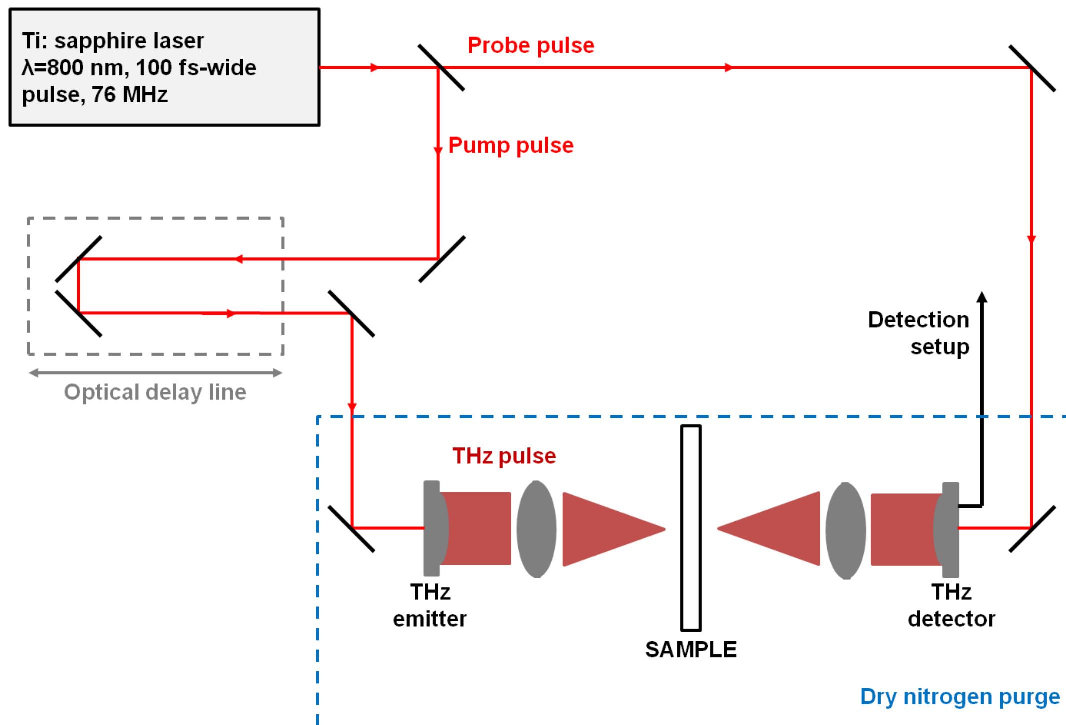

Figure 4.2: Schematic diagram of the THz-TDS set-up

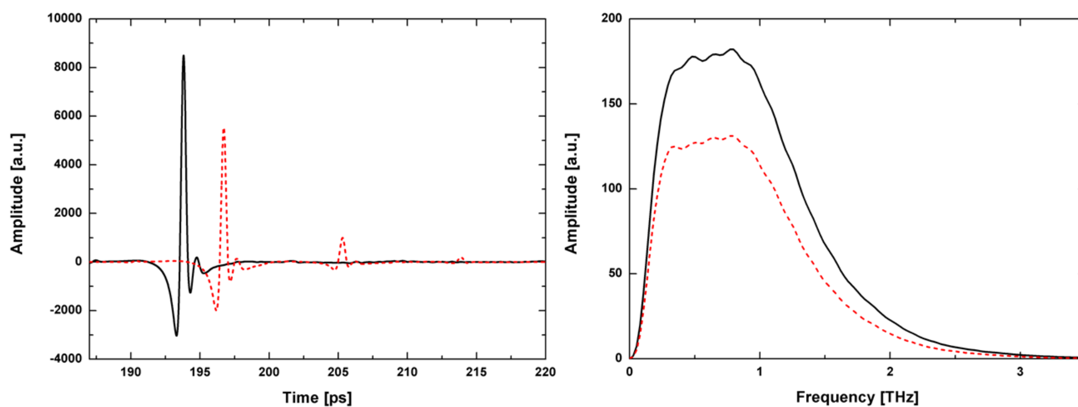

Figure 4.3: THz signals without (black) and with (red) sample in the time (left) and frequency (right) domains

The Fourier transformations of this time-domain data gives the amplitude and phase of the THz wave pulses; their ratio provides the complex transmission coefficient of the sample (Figure 4.4).

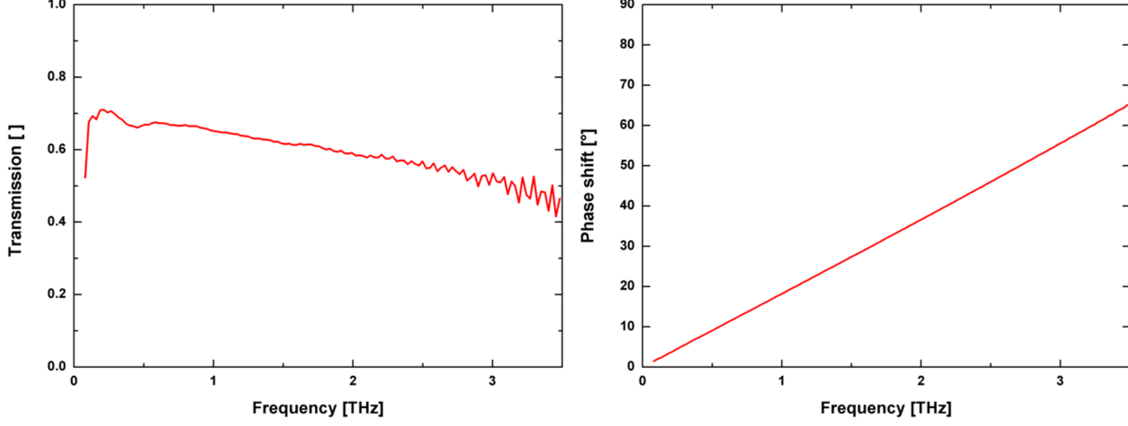

Figure 4.4: Transmission (left) and phase shift (right) of the complex transmission coefficient, ratio of the THz signals with and without a sample

4.1.1 Single layer

We have already defined the complex transmission and reflection coefficients in section 3.1.2.2 along with Huygens-Fresnel's Equations (3.39) to (3.42). If we label 0 and 1 the terms related to the ambiance and the sample respectively, we can write:

$$t_{01} = \frac{2 \cdot N_0}{N_0 + N_1} \tag{4.1}$$

$$t_{10} = \frac{2 \cdot N_1}{N_0 + N_1} \tag{4.2}$$

$$r_{10} = \frac{N_1 - N_0}{N_0 + N_1} \tag{4.3}$$

assuming a normal incidence, N_0 and N_1 being the respective complex optical indices of the ambiance and the sample.

For a d_1-thick sample, we can define the time shift β and express the global complex transmission coefficient t_g as:

$$\beta = 2 \cdot \pi \cdot \frac{d_1}{\lambda} \cdot N_1 = \frac{\omega \cdot d_1 \cdot N_1}{c} \tag{4.4}$$

$$t_g = \frac{E_1(\omega)}{E_0(\omega)} = t_{01} \cdot t_{10} \cdot e^{-i \cdot \frac{\omega \cdot d_1}{c} \cdot (N_1 - N_0)} + t_{01} \cdot t_{10} \cdot r_{10}^2 \cdot e^{-i \cdot \frac{\omega \cdot d_1}{c} \cdot (3 \cdot N_1 - N_0)} + \cdots$$

$$t_g = t_{01} \cdot t_{10} \cdot e^{-i \cdot \frac{\omega \cdot d_1}{c} \cdot (N_1 - N_0)} [1 + \sum_l r_{10}^{2 \cdot l} \cdot e^{-i \cdot 2 \cdot l \cdot \beta}] \tag{4.5}$$

$$t_g = \sqrt{T(\omega)} \cdot e^{-i\Phi(\omega)} \tag{4.6}$$

T(ω) and Φ(ω) are the power transmittance and relative phase shift that are measured through THz-TDS.

It is not possible to determine directly the general solution to Equation (4.5) and thus infer the optical index of the sample $N_1 = n_1 - i \cdot k_1$. Depending on the thickness of the sample though, there are some cases when we can neglect the echoes inside the sample.

4.1.1.1 For optically thick samples

For an optically thick sample, we can separate the echoes, so it is possible to ignore the Fabry-Perot effect. Equation (4.5) then becomes:

$$t_g = t_{01} \cdot t_{10} \cdot e^{-i \cdot \frac{\omega \cdot d_1}{c} \cdot (N_1 - N_0)} \qquad (4.7)$$

$$t_g = \sqrt{T(\omega)} \cdot e^{-i\Phi(\omega)} = \rho(\omega) \cdot e^{-i \cdot \Phi(\omega)} \qquad (4.8)$$

where ρ(ω) and Φ(ω) are the amplitude and phase shift of the ratio between the sample and the reference pulses. In the case of a material (such as sapphire [19]) with $k_1 << n_1$ and ambient conditions where $N_0 \approx 1$, we can further reduce these expressions and write:

$$t_g = \frac{4 \cdot n_1}{(n_1+1)^2} \cdot e^{-\frac{\omega \cdot d_1}{c} \cdot k_1} \cdot e^{-i \cdot \frac{\omega \cdot d_1}{c} \cdot (n_1 - 1)} \qquad (4.9)$$

so:

$$\rho(\omega) = \frac{4 \cdot n_1}{(n_1+1)^2} \cdot e^{-\frac{\omega \cdot d_1}{c} \cdot k_1} \qquad (4.10)$$

$$\Phi(\omega) = \frac{\omega \cdot d_1}{c} \cdot (n_1 - 1) \qquad (4.11)$$

These equations can be analytically inversed and we can conclude that

$$n_1 = 1 + \frac{\Phi(\omega) \cdot c}{\omega \cdot d_1} \qquad (4.12)$$

$$k_1 = \frac{c}{\omega \cdot d_1} \cdot ln \frac{4 \cdot n_1}{\rho(\omega) \cdot (n_1+1)^2} \qquad (4.13)$$

4.1.1.2 For optically thin samples

For optically thin samples, we must take the echoes into account and Equation (4.5) can only be written as

$$t_g = \frac{t_{01} \cdot t_{10} \cdot e^{-i \cdot \frac{\omega \cdot d_1}{c} \cdot (N_1 - N_0)}}{1 - r_{10}^2 \cdot e^{-i \cdot 2 \cdot \beta}} \qquad (4.14)$$

There is no analytical way to separate the amplitude and the phase shift of this expression and link directly Equation (4.14) to values of ρ(ω) and Φ(ω), we must use an approach similar to the one described in Chapter 3 for ellipsometry, numerically modeling $t_{g\ th}(\omega)$ as a function of N_1 and making it correlate with $t_{g\ exp}(\omega)$. The best fit will provide values for $n_1(\omega)$ and $k_1(\omega)$.

So long as we obtain the complex optical index of the sample, we can determine the complex dielectric and conductivity functions, ε(ω) and σ(ω) respectively:

$$\varepsilon(\omega) = N(\omega)^2 = \varepsilon_{dc} + i\frac{\sigma(\omega)}{\omega\varepsilon_0} \qquad (4.15)$$

with ε_{dc} being the dielectric constant.

4.1.2 Thin film on a substrate

In the case of a thin film deposited on a substrate, we define three waves and their associated electrical fields, as depicted in Figure 4.5: the reference signal $E_0(\omega)$ without the sample, the signal going through the substrate $E_1(\omega)$ and the signal through the whole sample $E_2(\omega)$ including the substrate and the film. They are represented in time and frequency domains in Figure 4.6.

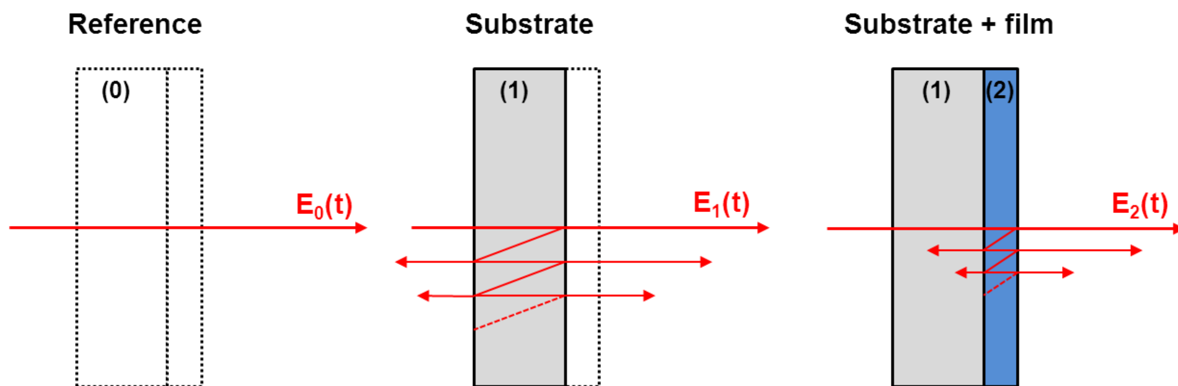

Figure 4.5: THz-TDS measurements necessary for the analysis of a thin film deposited on a substrate

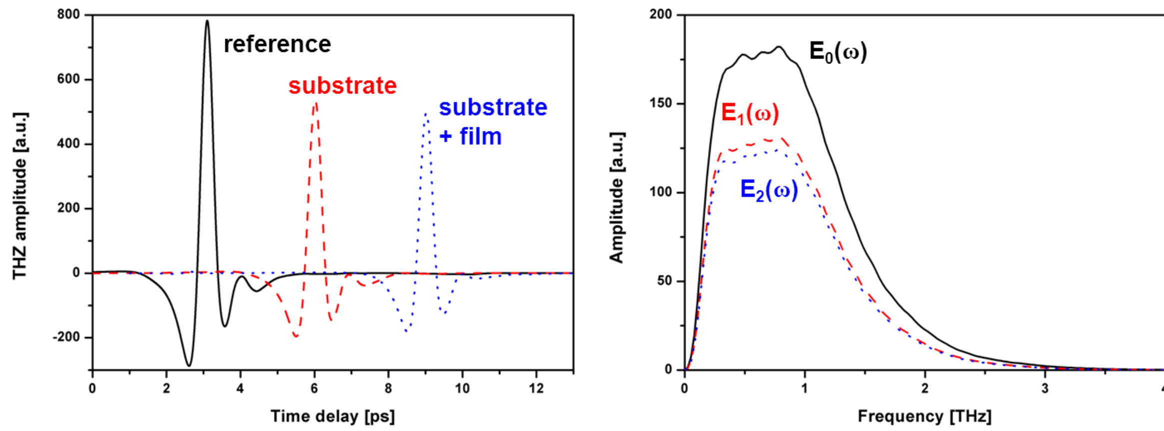

Figure 4.6: THz signals without any sample (black), with a substrate (red) and with a thin film on a substrate (blue) in the time (left) and frequency (right) domains

The parameters of the substrate can be calculated using the method described in section 4.1.1. We consider the substrate to be optically thick. We can write:

$$\beta_1 = 2 \cdot \pi \cdot \frac{d_1}{\lambda} \cdot N_1 = \frac{\omega \cdot d_1 \cdot N_1}{c} \tag{4.16}$$

$$\beta_2 = 2 \cdot \pi \cdot \frac{d_2}{\lambda} \cdot N_2 = \frac{\omega \cdot d_2 \cdot N_2}{c} \tag{4.17}$$

$$\frac{E_1(\omega)}{E_0(\omega)} = t_{01} \cdot t_{10} \cdot e^{-i \cdot (N_1 - N_0) \cdot \frac{\omega \cdot d_1}{c}} \tag{4.18}$$

$$\frac{E_2(\omega)}{E_0(\omega)} = t_{01} \cdot t_{12} \cdot t_{20} \cdot e^{-i \cdot \beta_1} \cdot e^{-i \cdot \beta_2} + t_{01} \cdot t_{12} \cdot t_{20} \cdot r_{20} \cdot r_{21} \cdot e^{-i \cdot \beta_1} \cdot e^{-i \cdot 3 \cdot \beta_2} + \cdots$$

$$\frac{E_2(\omega)}{E_0(\omega)} = t_{01} \cdot t_{12} \cdot t_{20} \cdot e^{-i \cdot \beta_1} \cdot e^{-i \cdot \beta_2} \cdot \sum_l {r_{20}}^l \cdot {r_{21}}^l \cdot e^{-i \cdot 2 \cdot l \cdot \beta_2}$$

$$\frac{E_2(\omega)}{E_0(\omega)} = \frac{t_{01} \cdot t_{12} \cdot t_{20} \cdot e^{-i \cdot \beta_1} \cdot e^{-i \cdot \beta_2}}{1 - r_{20} \cdot r_{21} \cdot e^{-i \cdot 2 \cdot \beta_2}} \tag{4.19}$$

From Equations (4.18) and (4.19), we can finally conclude that:

$$\frac{E_2(\omega)}{E_1(\omega)} = \frac{t_{12} \cdot t_{20} \cdot e^{-i \cdot \beta_2}}{t_{10} \cdot e^{-i \cdot \frac{\omega \cdot d_2}{c} \cdot N_0} \cdot (1 - r_{20} \cdot r_{21} \cdot e^{-i \cdot 2 \cdot \beta_2})} \tag{4.20}$$

If we re-introduce the complex indices of the three mediums, we obtain:

$$\frac{E_2(\omega)}{E_1(\omega)} = \frac{2 \cdot N_2 \cdot (N_0 + N_1) e^{-i \cdot \frac{\omega \cdot d_2}{c} \cdot (N_2 - N_0)}}{(N_1 + N_2)(N_0 + N_2) - (N_0 - N_2)(N_1 - N_2) e^{-i \cdot 2 \cdot \frac{\omega \cdot d_2}{c} \cdot N_2}} \tag{4.21}$$

This Equation (4.21) is used to fit the ratio of the Fourier transforms of the signals through the as-grown sample and through the sample, similarly to what is done in section 4.1.1.2. Equation (4.15) provides the dielectric and conductivity functions.

From the conductivity function, it is then possible to extract values of the free carrier concentration N and mobility μ. We will see in the experimental study that the real part of the conductivity is monotonically decreasing as the frequency increases while the imaginary part increases. This frequency dependence is characteristic of Drude-like materials below the plasma frequency [17,19]. The simple Drude model assumes that the velocity of the carriers is relaxed with a single, energy-independent relaxation time τ_0 and the carriers scattering is isotropic [20,21]. We thus fit the inferred conductivity using the simple Drude model that establishes:

$$\sigma(\omega) = \frac{\varepsilon_0 \cdot {\omega_p}^2 \cdot \tau_0}{1 - i \cdot \omega \cdot \tau_0} \qquad (4.22)$$

where ω_p is the plasma frequency ${\omega_p}^2 = \frac{N \cdot e^2}{\varepsilon_0 \cdot m^*}$ and the relaxation time $\tau_0 = \frac{\mu \cdot m^*}{e}$, m^* is the effective electron mass and e the elementary charge. The fitting allows the extraction of values for N and μ that can be compared to the ones measured by Hall effect.

4.2 Experimental study of InGaN thin films

The THz-TDS data are obtained using a TeraView Spectra 3000 system. It is commercial terahertz spectrometer based on two low-temperature-grown GaAs (LT-GaAs) photo-conductive dipole antennas that are used for generation and detection of THz pulses generated by a mode-locked amplified Ti:sapphire laser (λ = 800 nm) emitting ~ 100 fs-long pulses at a repetition rate of 76 MHz. The generated THz wave is collimated and focused on the samples by off-axis parabolic gold-coated mirrors and the set-up is placed in a chamber purged with dry nitrogen to minimize the water vapor absorption, as described in Figure 4.2.

All the studied samples are of the "thin film on a substrate" type introduced in paragraph 4.1.2, which means that we need to collect three signals as a reference, for the substrate alone and for the substrate and the as-grown thin film. In the case of InGaN samples, we consider the sapphire and GaN-on-sapphire template to form a single homogeneous effective substrate. This leads to non-usable substrate optical indices in the intermediary calculations, but does not influence the final results and the values of the extracted optical indices for the thin films.

To measure the $E_1(t)$ signal, the top layer is removed on half of the surface of the studied samples using inductively coupled plasma (ICP) etching with Cl_2 and BCl_3 gases. By focusing the THz beam on either half of the sample, we can therefore obtain data for the effective substrate ($E_1(t)$) or the full samples ($E_2(t)$), as pictured in the Figure 4.7. $E_0(t)$ is simply measured in the empty chamber.

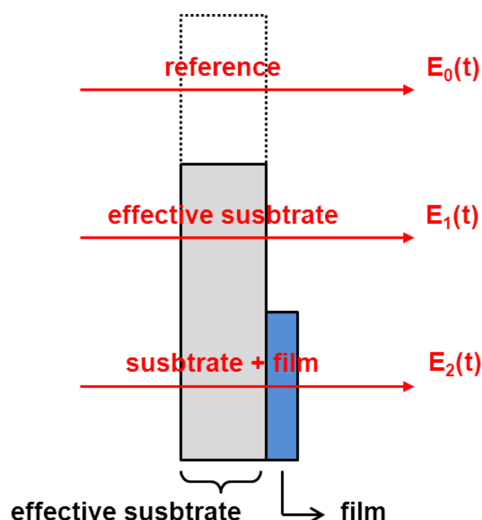

Figure 4.7: Etched sample and measured signals necessary to the THz-TDS analysis

4.2.1 Experimental study of a GaN thin films

As with spectroscopic ellipsometry, we start our analysis with GaN samples. This material is the most widely studied in the III-nitride family and there are several publications reporting THz-TDS [10-13]. We use the samples GaN-1, GaN-2 and GaN-3 defined in section 2.1.2.1. They cover a range of carrier concentration ($N=2.5\times10^{17}$ cm^{-3}, 1.8×10^{18} cm^{-3} and 3.3×10^{18} cm^{-3} respectively) that will help us to compare our experimental values with the optical indices reported by *Zhang et al.* [10] ($N=0.9\times10^{16}$ cm^{-3}), *Fang et al.* [13] ($N=1.0\times10^{18}$ cm^{-3}), *Tsai et al.* [11] ($N=1.5\times10^{18}$ cm^{-3}) and *Guo et al.* [12] ($N=6.1\times10^{17}$ cm^{-3} and $N=2.0\times10^{18}$ cm^{-3}).

The values of the dielectric constant and effective electron mass for GaN can be found in the literature and are chosen as $\varepsilon_{dc} = 9.4$ [23] and $m^* = 0.22m_0$ [24] with m_0 being the mass of the free electron.

Figure 4.8 presents the extracted refraction indices and extinction coefficient for our samples and the comparative values reported in literature.

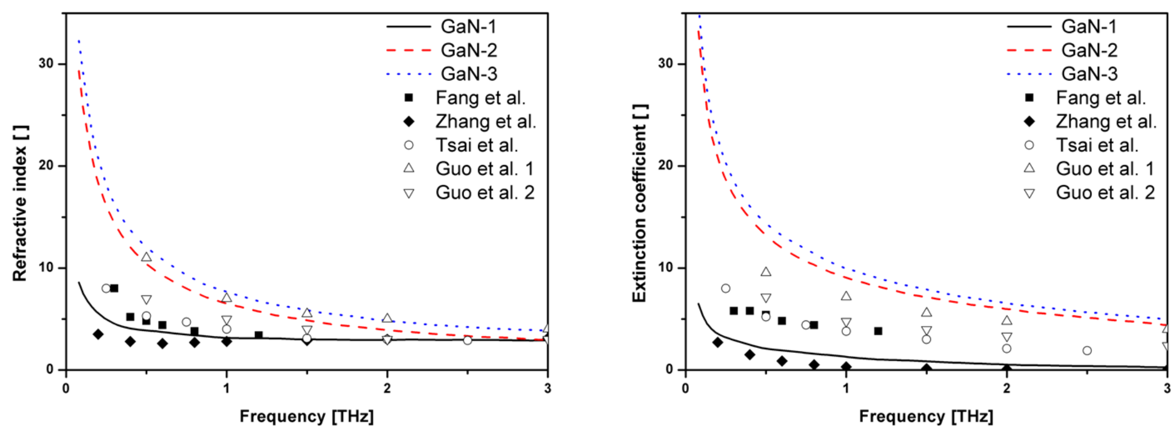

Figure 4.8: Refractive indices (left) and extinction coefficients (right) of samples GaN-1 (black plain line), GaN-2 (red dashed line) and GaN-3 (blue dotted line) and comparison with values provided in other works [10-13]

As suggested in the theoretical study by Equations (4.15) and (4.22), both the refractive index and extinction coefficient increase with a rise of the carrier concentration N. We saw in paragraph 4.1.2 that this correlation is also related to the mobility μ, but the relative variation of the carrier concentration (between 10^{16} cm^{-3} and 10^{18} cm^{-3}) compared to the one of the mobility (124 $cm^2.s^{-1}.V^{-1}$ to 337 $cm^2.s^{-1}.V^{-1}$, see Table 4-1) means that σ(ω), and by extension ε(ω) and N(ω) are influenced by the carrier concentration a lot more significantly than by the mobility.

The THz-TDS study provides values for the carrier concentration and mobility that can be compared with Hall effect measurements. They are tabulated in the Table 4-1:

Sample	**N TDS [cm^{-3}]**	**N Hall [cm^{-3}]**	**μ TDS [$cm^2.s^{-1}.V^{-1}$]**	**μ Hall [$cm^2.s^{-1}.V^{-1}$]**
GaN-1	1.10×10^{17}	2.50×10^{17}	245	124
GaN-2	1.10×10^{18}	1.80×10^{18}	436	337
GaN-3	1.90×10^{18}	3.30×10^{18}	300	260

Table 4-1: Carrier concentrations and mobilities from THz-TDS analysis and Hall effect measurements for GaN samples

The THz-TDS method gives underestimated values of N and overestimated values of μ compared to Hall measurement. This can be explained by the nature of both experiments: in-plane for the Hall measurements, normal to the layers for THz-TDS. For example, Hall

measurements are known to be affected by scattering from grain boundaries. On the contrary, the results derived from optical measurements are not influenced by the grain size in a semiconductor thin film when the frequency is high enough [25].

Still, if we compare the relative evolutions of the carrier concentrations and mobilities for THz-TDS on one hand and Hall measurements on the other, we find similar variations, which proves that each data set is coherent on its own.

4.2.2 Experimental study of InGaN thin films

A big issue for the $In_xGa_{1-x}N$ THz-TDS analysis is that there is no information on the topic in literature. Values for ε_{dc} and m^* for example are not available at any given value of x and would require a full carrier dynamics study to be determined. As an approximation, we use the values of GaN for the InGaN samples. Fortunately, InN is a better-known material and such constants have been clarified. In our measurements, we use ε_{dc} = 13.1 [26] and m^* = $0.14m_0$ [27] for InN. Figure 4.9 plots the refractive indices and extinction coefficients of sample GaN-1, InGaN-1, InGaN-2, InGaN-3 and InN.

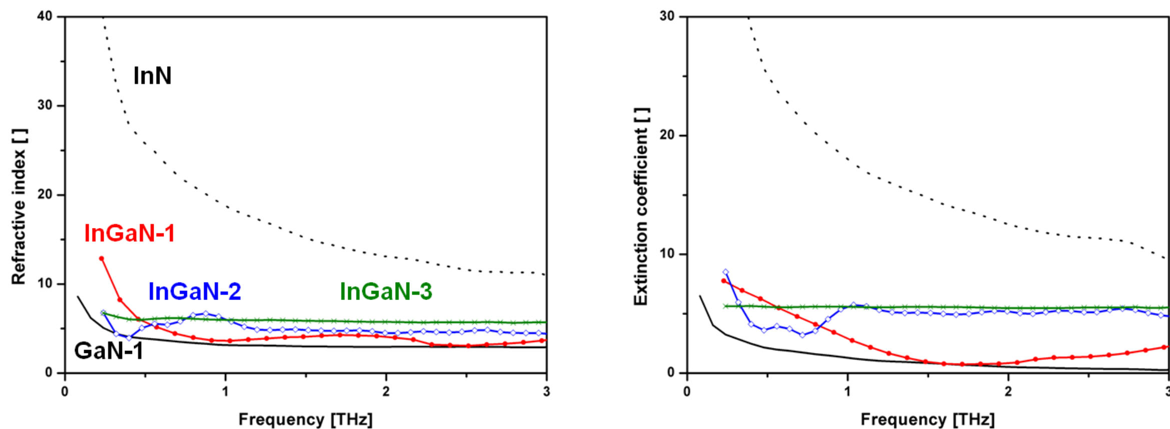

Figure 4.9: Refractive indices (left) and extinction coefficients (right) of samples GaN-1 (plain black), InGaN-1 (red), InGaN-2 (blue), InGaN-3 (green) and InN (dotted black)

We observe that the indices of InGaN samples are between the ones of GaN and InN and ordered by increasing indium fraction: the higher the indium content, the higher the refractive index and the extinction coefficient. While the values of GaN-1, InGaN-1 and InGaN-2 are clearly distinct from each other, InGaN-3 is very close to InGaN-2 as we already concluded in chapter 3 (Figure 3.17). This is believed to be due to the alloy scattering, inhomogeneity

and a growing number of defects with x, as showed by the higher v-pit density in the TEM images (see section 2.2.1.1). The higher indium concentration increases the internal strain, modifying the bandgap structure and resulting in a lower refractive index value [28].

The only other report on InN optical index in the THz domain by *Ahn et al.* [14] provides values 25% higher than ours at a similar range of carrier densities (~ 10^{18} cm^{-3}) but at a mobility of 1217 $cm^2.s^{-1}.V^{-1}$ against 580 $cm^2.s^{-1}.V^{-1}$ with our Hall measurement, which makes our measurements in good agreement overall. Carrier concentrations and mobilities are provided in Table 4-2.

Sample	**N TDS [cm^{-3}]**	**N Hall [cm^{-3}]**	**µ TDS [$cm^2.s^{-1}.V^{-1}$]**	**µ Hall [$cm^2.s^{-1}.V^{-1}$]**
GaN-1	1.10×10^{17}	2.50×10^{17}	245	124
InGaN-1	7.20×10^{17}	5.10×10^{17}	91	94.2
InGaN-2	7.60×10^{17}	6.40×10^{17}	83	92.5
InGaN-3	1.00×10^{18}	6.50×10^{17}	80	92.4
InN	2.60×10^{18}	4.40×10^{18}	718	580

Table 4-2: Carrier concentrations and mobilities from THz-TDS analysis and Hall effect measurements for GaN, InGaN and InN samples

The behaviour of InN is comparable to the one described for GaN: an underestimation of the carrier concentration and overestimation of the mobility by THz-TDS compared to Hall measurements. For InGaN samples though, the situations seems to be reversed and the agreement between the values from both method is much better. A possible cause for this phenomenon lies in the approximation we made for ε_{dc} and m^* as the discrepancy seems to increase for samples with higher indium fractions.

Another issue raised by InGaN sample lies in the low absorption of the thin films. InN has a high absorption coefficient and the low absorption is compensated in the case of GaN by thicker layers. In the case of InGaN, the signals from the effective substrate and the as-grown sample is very small, which leads to a lower precision of the measurements and noisier results, as can be seen in the conductivities drawn in Figure 4.10:

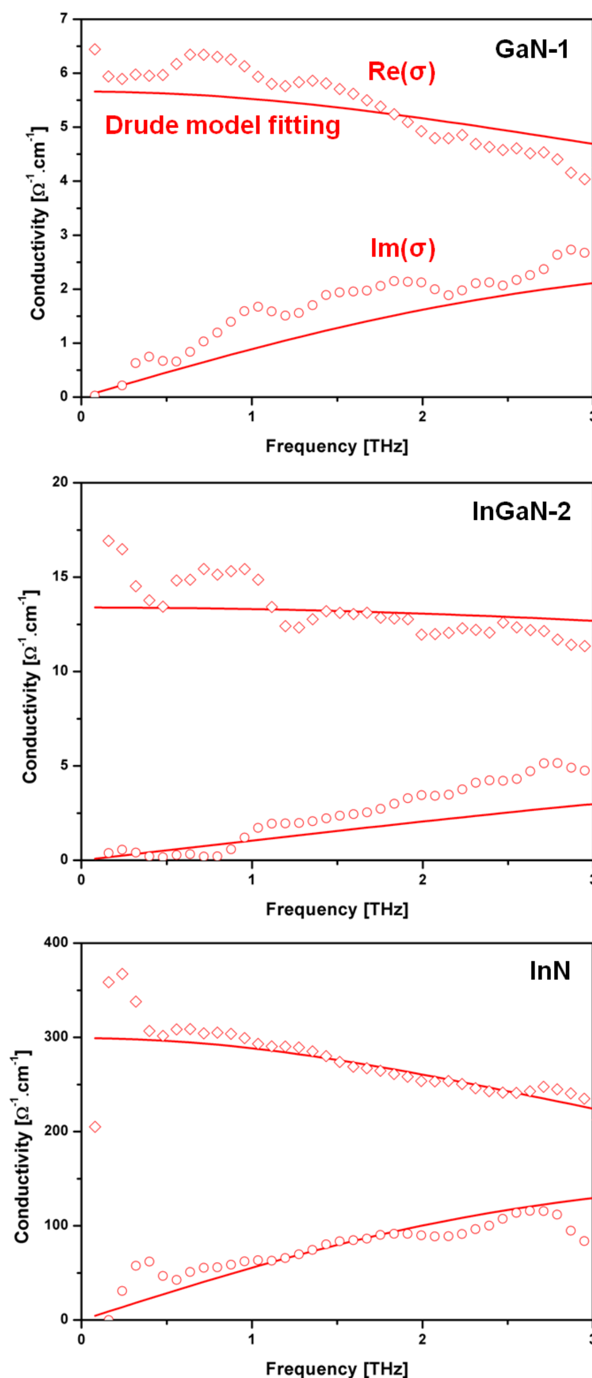

Figure 4.10: Conductivity functions for GaN-1 (top), InGaN-2 (middle) and InN (bottom) samples

These curves provide valuable information on the overall precision of our measurement as the comparison of the carrier concentration and mobility with Hall effect measurements only gives an element of comparison on the entire frequency range whereas the conductivity functions actually details the fit between the Drude model and the experimental measures for every frequency. In our case, we can observe that the numerical fitting is good for GaN and

InN but the values for InGaN are more irregular not as precise. This can also be correlated with the estimated precision of the optical indices determined by THz-TDS: 1-2% for InN, 4-5% for GaN and 5-10% for InGaN.

This is a limitation of the time-domain spectroscopy as it can only reliably extract optical index values under the condition of a thin film that absorbs enough of the THz wave. This calls for a series of measurements on a new set of InGaN samples, either with a higher thickness, an increased carrier concentration or a higher indium composition. Unfortunately, these are not yet available but the characterization technique has proven its relevance.

We have been able to determine and report the values of the refractive index, extinction coefficient, dielectric and conductivity functions for InGaN in the THz range for the first time and consolidated the current knowledge on GaN and InN. This opens the door to further characterization of InGaN as new samples will be made available and carrier dynamics knowledge will get more precise. Beyond the characterization, this brings the reality of III-nitride-based components operating in the THz domain closer, and with it, the possibility of efficient, compact and tunable sources and detectors, able to operate continuously at ambient temperature.

References

[1] M. Tonouchi, "Cutting-edge terahertz technology", *Nature Photon.* **1**, 97-105 (2007)

[2] B.E. Foutz, S.K. O'Leary, M.S. Shur and L.F. Eastman, "Transient electron transport in wurtzite GaN, InN, and AlN", *J. Appl. Phys.* **85**, 7727-7734 (1999)

[3] R. Gaska, J.W. Yang, A. Osinsky, Q. Chen, M. Asif Khan, A.O. Orlov, G.L. Snider and M.S. Shur, "Electron transport in AlGaN-GaN heterostructures grown on 6H-SiC substrates", *Appl. Phys. Lett.* **72**, 707-709 (1998)

[4] K.T. Tsen, C. Poweleit, D.K. Ferry, H. Lu and W.J. Schaff, "Observation of large electron drift velocities in InN by ultrafast Raman spectroscopy", *Appl. Phys. Lett.* **86**, 222103 (2005)

[5] V.D. Jovanović, D. Indjin, Z. Ikonić and P. Harrison, "Simulation and design of GaN/AlGaN far-infrared ($\lambda \sim 34$ μm) quantum-cascade laser", *Appl. Phys. Lett.* **84**, 2995-2997 (2004)

[6] Ricardo Ascázubi, I. Wilke, K. Denniston, H. Lu and W.J. Schaff, "Terahertz emission by InN", *Appl. Phys. Lett.* **84**, 4810-4812 (2004)

[7] G. Sun, R.A. Soref and J.B. Khurgin, "Active region design of a terahertz GaN/$Al_{0.15}Ga_{0.85}N$ quantum cascade laser", *Supperlattices Microstruct.* **37**, 107-113 (2005)

[8] T.V. Shubina, A.V. Andrianov, A.O. Zakhar'in, V.N. Jmerik, I.P. Soshnikov, T.A. Komissarova, A.A. Usikova, P.S. Kop'ev, S.V. Ivanov, V.A. Shalygin, A.N. Sofronov, D.A. Firsov, L.E. Vorob'ev, N.A. Gippius, J. Leymarie, X. Wang and A. Yoshikawa, "Terahertz electroluminescence of surface plasmons from nanostructured InN layers", *Appl. Phys. Lett.* **96**, 183106 (2010)

[9] G. Sun, G. Xu, Y.J. Ding, H. Zhao, G. Liu, J. Zhang and N. Tansu, "Efficient terahertz generation within InGaN/GaN multiple quantum wells", *IEEE J. Sel. Top. Quantum Electron.* **17**, 48-53 (2011)

[10] W. Zhang, A.K. Azad and D. Grischkowsky, "Terahertz studies of carrier dynamics and dielectric response of n-type, freestanding epitaxial GaN", *Appl. Phys. Lett.* **82**, 2841-2843 (2003)

[11] T.R. Tsai, S.J. Chen, C.F. Chang, S.H. Hsu, T.Y. Lin and C.C. Chi, "Terahertz response of GaN thin films", *Opt. Express* **14**, 4898-4907 (2006)

[12] H.C. Guo, X.H. Zhang, W. Liu, A.M. Yong and S.H. Tang, "Terahertz carrier dynamics and dielectric properties of GaN epilayers with different carrier concentrations", *J. Appl. Phys.* **106**, 063104 (2009)

[13] H.N. Fang, R. Zhang, B. Liu, H. Lu, J.P. Ding, Z.L. Xie, X.Q. Xiu, Y.D. Zheng, M.W. Xiao, C.H. Zhang, J. Chen and P.H. Wu, "Dielectric properties of GaN in THz frequencies", *Chin. Phys. Lett.* **27**, 017802 (2010)

[14] H. Ahn, C.L. Pan and S. Gwo, "Terahertz emission and spectroscopy on InN epilayer and nanostructure", *Proc. SPIE* **7216**, 72160T (2009)

[15] J.L. Coutaz, *Optoélectronique Térahertz*, EDP Sciences, Les Ulis (2008)

[16] L. Duvillaret, F. Garet, J.L. Coutaz, "A reliable method for extraction of material parameters in terahertz time-domain spectroscopy", *IEEE J. Sel. Top. Quantum Electron.* **2**, 739-746 (1996)

[17] M. van Exter and D. Grischkowsky, "Carrier dynamics of electrons and holes in moderately doped silicon", *Phys. Rev. B* **41**, 12140-12149 (1990)

[18] J.E. Pedersen and S.R. Keiding, "THz time-domain spectroscopy of nonpolar liquids", *IEEE J. Quantum Electron.* **28**, 2518-2522 (1992)

[19] D. Grischkowsky, S. Keiding, M. van Exter and C. Fattinger, "Far-infrared time-domain spectroscopy with terahertz beams of dielectrics and semiconductors", *J. Opt. Soc. Am. B* **7**, 2006-2015 (1990)

[20] K.E. Peiponen and J.J. Saarinen, "Generalized Kramers–Kronig relations in nonlinear optical- and THz-spectroscopy", *Rep. Prog. Phys.* **72**, 056401 (2009)

[21] P. Drude, "Zur Elektronentheorie der Metalle", *Ann. Phys.* **306**, 566-613 (1900)

[22] N. V. Smith, "Classical generalization of the Drude formula for the optical conductivity", *Phys. Rev. B* **64**, 155106 (2001)

[23] A.S. Barker, Jr. and M. Ilegems, "Infrared lattice vibrations and free-electron dispersion in GaN", *Phys. Rev. B* **7**, 743-750 (1973)

[24] W.J. Moore and J.A. Freitas, Jr., "Zeeman spectroscopy of shallow donors in GaN", *Phys. Rev. B* **56**, 12073-12076 (1997)

[25] J. Steinhauser, S. Faÿ, N. Oliveira, E. Vallat-Sauvain and C. Ballif, "Transition between grain boundary and intragrain scattering transport mechanisms in boron-doped zinc oxide thin films", *Appl. Phys. Lett.* **90**, 142107 (2007)

[26] V.Y. Davydov, V.V. Emtsev, I.N. Goncharuk, A.N. Smirnov, V.D. Petrikov, V.V. Mamutin, V.A. Vekshin, S.V. Ivanov, M.B. Smirnov and T. Inushima, "Experimental and theoretical studies of phonons in hexagonal InN", *Appl. Phys. Lett.* **75**, 3297-3299 (1999)

[27] A. Kasic, M. Schubert, Y. Saito, Y. Nanishi and G. Wagner, "Effective electron mass and phonon modes in n-type hexagonal InN", *Phys. Rev. B* **65**, 115206 (2002)

[28] F. Natali, F. Semond, J. Massies, D. Byrne, S. Laügt, O. Tottereau, P. Vennéguès, E. Dogheche and E. Dumont, "Correlation between threading dislocation density and the refractive index of AlN grown by molecular-beam epitaxy on Si(111)", *Appl. Phys. Lett.* **82**, 1386-1388 (2003)

Chapter 5
Application – Fabrication of an InGaN-based terahertz photodiode

5. CHAPTER 5 APPLICATION – FABRICATION OF AN INGAN-BASED TERAHERTZ PHOTODIODE 107

5.1 TERAHERTZ SOURCES 108

5.1.1 Electronics approach 109

5.1.1.1 Transistor-based oscillators 109

5.1.1.2 Resonant tunneling diodes........ 110

5.1.1.3 Frequency conversion 112

5.1.2 Optics approach 112

5.1.2.1 Gas lasers 112

5.1.2.2 Quantum cascade lasers 113

5.1.3 Optoelectronics approach 114

5.2 ULTRAFAST PHOTODIODE FOR TERAHERTZ GENERATION 115

5.2.1 Design of a terahertz photodiode........ 116

5.2.2 Fabrication of a terahertz photodiode 118

5.2.2.1 Growth of the structure 118

5.2.2.2 Technological steps for the fabrication of the photodiode 118

5.3 CONCLUSION AND PERSPECTIVES 124

REFERENCES 125

We have already described in chapter 4 the intrinsic advantages of the III-nitrides for THz waves emission. The goal of these characterization experiments we applied to GaN, InGaN and InN, is to provide information on the material that are essential for the design of devices. However reports on InGaN for THz sources and detectors are still scarce. We examine in this chapter the different ways to emit THz radiations and suggest a device structure design using GaN, InGaN and InN that can generate a continuous wave in the THz domain.

5.1 Terahertz sources

As explained in the introduction to chapter 4, the terahertz frequency range is situated in the electromagnetic spectrum space between the radio- and microwaves of the electronics spectrum and the infrared region in the optics domain. For this reason, two technology roadmaps exist for THz devices, as seen in Figure 5.1 [1]. From the lower side of terahertz frequencies, electronics-based devices, such as Gunn diodes, impact avalanche transit time (IMPATT) diodes, resonant tunneling diodes based on negative differential resistance, backward wave oscillators and field effect transistors (FETs) are extensively investigated for THz frequencies. From higher side, photonics-based devices such as gas lasers and quantum cascade lasers (QCLs) try and extend the emission wavelength from mid- and far-infrared to the THz spectral range.

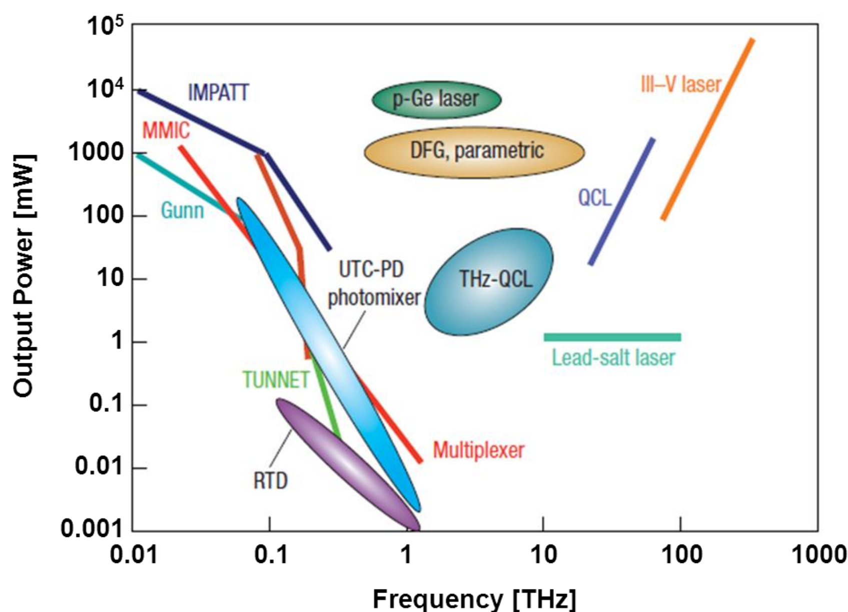

Figure 5.1: THz emission power as a function frequency. Ovals denote recent THz sources.

As a combination of both electronics and optics, the optoelectronics approach seems to be an ideal third way to reach the THz domain, as it can call for a number of effects like photoconduction, photomixing, surface effects or non-linear effects. In optoelectronics, III-nitrides have already proven their usefulness numerous times and could prove a very suitable candidate in THz range as well. We will detail in this section the most commonly used terahertz sources using the three different approaches.

5.1.1 Electronics approach

The challenge with the electronics approach is that the frequency limit of electronic devices is hindered by two concurrent physical phenomena: capacitive effects and carriers transit time. For example, limiting capacitive effects is possible through the increase of the thickness of depleted zones, but it also increases the transit time and lowers the work frequency.

5.1.1.1 Transistor-based oscillators

Recent investigations reveal that it is possible to realize some ultra-fast transistors able to generate frequencies above 100 GHz and up to the THz frequency domain. Two types of structures are preferred, high electron mobility transistors (HEMTs) and heterojunction bipolar transistors (HBTs).

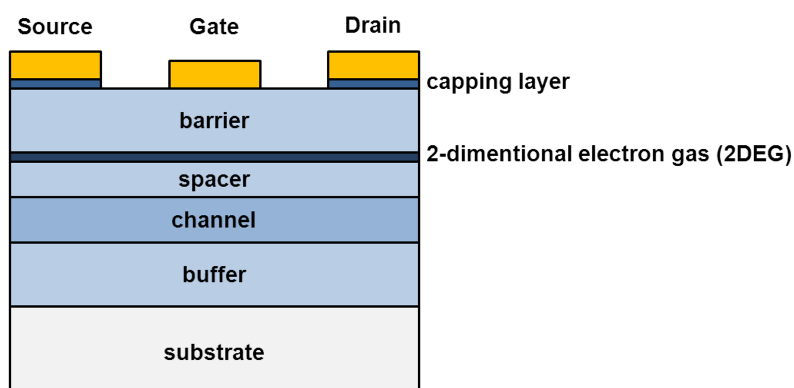

Figure 5.2: Typical layer structure of a HEMT

HEMTs are FETs in which the donor atoms are placed in the δ-doping layer (2DEG) separated from the channel by a spacer layer built to limit the far-interaction of the ionized impurities with carriers in the channel, as shown in the diagram of Figure 5.2. Combined with

a high-mobility material such as GaAs, InP or InN, this helps building a very fast carriers transit in the channel.

HBTs are an evolution of the bipolar transistors built to obtain higher frequencies. The principle of these devices is to add a heterojunction to limit the injection of holes in the emitter region, thus allowing the increase of the base doping and by consequence the reduction of the base resistance. HBTs have a vertical structure shown in figure 5.3.

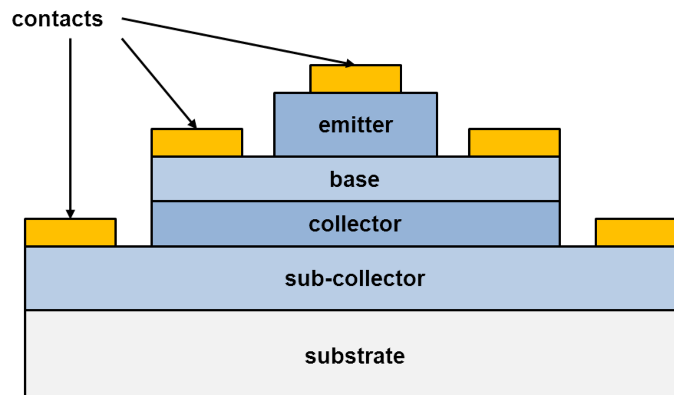

Figure 5.3: Typical layer structure of HBT

InP/InGaAs HBTs have reached unity gain cut-off (f_T) of at least 845 GHz at 220 K (745 GHz at room temperature) [2] while SiGe HBTs are being tested at an f_T of 510 GHz at 4.5 K (352 GHz at room temperature) [3].

As for HEMTs, InGaAs/InAlAs devices have been reported to yield 400 GHz to 1 THz radiations [4] and a AlGaN/GaN HEMT was reported to produce 1.5 THz radiation at room temperature [5].

5.1.1.2 Resonant tunneling diodes

Negative differential resistance (NDR)-based diodes have been used in high frequency regime for many years. Their high output powers as well as their manufacturing feasibility are strong advantages that promote their use in the THz regime.

Resonant tunneling diodes (RTDs) are a type of NDR-based device that presents a negative differential resistance under particular biases. This property is due to quantum effects during carriers displacement into the diode. A typical RTD is represented in the Figure 5.4; it is built

with two potential gates and a quantum well in the opposite direction of the electron displacement.

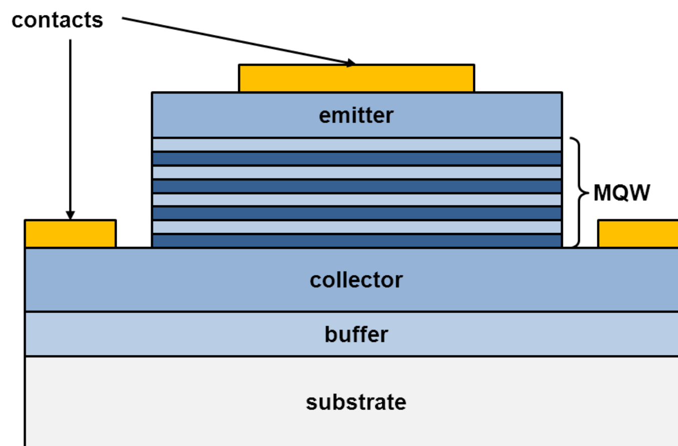

Figure 5.4: Typical layer structure of a resonant tunneling diode

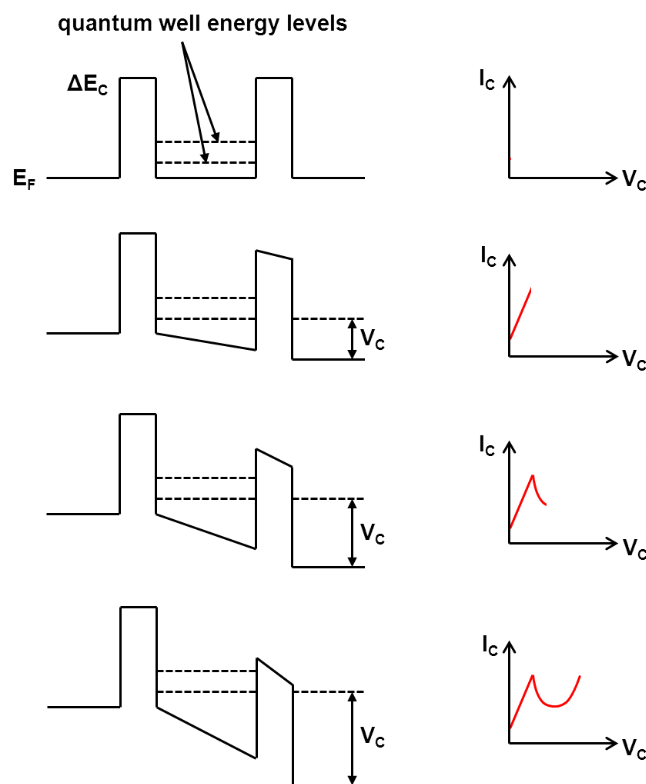

Figure 5.5: Step by step building of the current-voltage characteristics of a resonant tunneling diode

As we increase the bias of the diode, the electrons begin to cross the quantum well gates to reach the optimal bias corresponding to the alignment of the Fermi injection level with the first energy level inside the quantum well. If the bias voltage is increased, the number of electrons decreases in the channel, and so does the current. As a consequence, a negative differential resistance occurs in this domain of bias as shown in figure 5.5. This is then used to maintain oscillations in a device.

InAs/AlSb RTD have been reported to operate at 712 GHz for over a decade now, but with very low output power [6]. More recently, InGaAs/AlAs devices reached 587 GHz and, using harmonics, 1.02 THz [7]. AlGaN/GaN double-barrier RTDs have demonstrated excellent room-temperature operation and very high potential thanks to a peak-to-valley ration of 32 [8], but instabilities caused by traps due to crystal quality remains an issue [9].

5.1.1.3 Frequency conversion

Transistors and diodes, despite the attention they are getting, still hardly function above 500 GHz. An alternative method to obtain THz frequencies is to use an existing input source in the radio frequencies (RF) domain and use some non-linear devices which can multiply the frequency by harmonics generation until the THz range is reached. This can be achieved by using components such as the varactor and varistor modes of GaAs Schottky diodes. The latter technology is able to generate frequencies up to 2.7 THz [10]. There are many advantages of choosing this technology to generate THz waves such as the accuracy in term of frequency directly related to the accuracy of the RF source, but the efficiency of this system can be low, the first stages need to support high power and the system is usually complex and mechanically delicate.

5.1.2 Optics approach

A second possible approach is based on increasing the wavelength of a laser source, which already cover a wide range of domain, from infrared to visible to ultraviolet.

5.1.2.1 Gas lasers

Historically, gas lasers have been the first THz sources. Although the transitions between the different energy levels in the valence band of hydrogen cyanide (HCN) and methyl-fluorine (CH_3F) can be used to produce terahertz radiations, the much more benign CO_2 is more

popular and has been responsible for the development of optically pumped terahertz lasers. Germanium-based lasers are tunable from 1 THz to 4 THz and display high power output and narrow bandwidth, but require very strong electric and magnetic fields. Heating effect also prevents the continuous wave emission and operation is only possible under liquid helium cooling [11].

5.1.2.2 Quantum cascade lasers

One of the most popular optical devices adapted for the generation of THz frequencies is the quantum cascade laser (QCL). It is a heterostructure made of a succession of building blocks: each one is composed of an injection and an active region as illustrated in Figure 5.6. In the active region, the electron stimulates the generation of a photon by making a transition from upper to lower energy level while in the injection region they are injected from the lower level of the last block to the excited one of the next block active region.

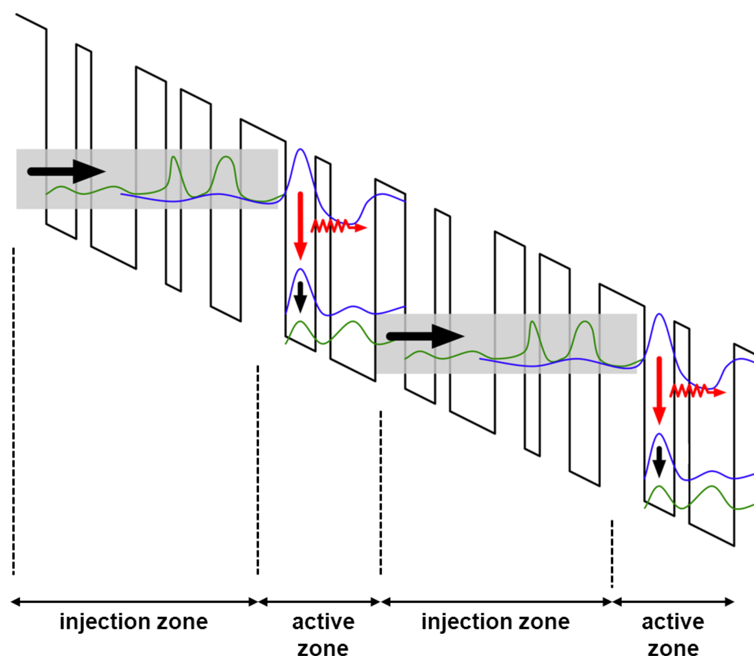

Figure 5.6: Schematic diagram of the conduction band in the active region of a QCL

The first MQWs QCL was realized in 1994 employing InGaAs/InAlAs [12]. From then on, a rapid progress has been shown in performance, leading to the first THz QCL based on AlGaAs/GaAs in 2002 [13]. QCL wavelengths vary from 3.5 µm (~ 0.4 eV ~ 80 THz) up to 160 µm (~ 8 meV ~ 2 THz) and beyond. Pushing to the lower (THz) end, there are a number of differences and complications since the intersubband transitions used to create the laser

radiation are much narrower (1-4 meV). Currently, the maximal output power of GaAs-based THz QCL has approached 250 mW at 10 K [14], the wavelength has extended to 1.39 THz [15] and operating temperatures of 164 K and 117 K were reported in pulsed and continuous mode respectively [16]. The design and Monte-Carlo simulation of AlGaN/GaN-based THz QCLs also demonstrate the good expected optical gain and operating temperature [17].

5.1.3 Optoelectronics approach

A third approach, capitalizing on the position of the THz domain in the electromagnetic spectrum, can a joint make use of both electronics and optics. Using the non-linearity of a photodetector in which the current or potential depends on the received optical power; that signal is then radiated by an antenna, as represented on Figure 5.7.

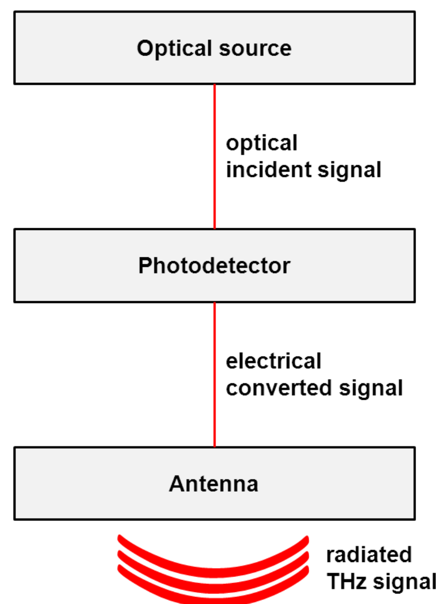

Figure 5.7: Principle diagram of a THz optoelectronic source

In the case of a pulsed mode system, the photodetector generates an electrical signal related to the envelope of an optical impulsion. Due to the response time of the photodetector, the envelope is broadened and allows creating an ultra-short electrical impulsion with a wide frequency spectrum. A wideband antenna finally radiates the signal. A typical system consists of a split antenna switch structure fabricated on a low temperature-grown GaAs as described in Figure 5.8. A DC potential difference is set up across a gap in the structure illuminated by pump near-infrared (NIR) laser pulses. Photo-generated charge carriers jump the gap with the

current burst producing terahertz electromagnetic waves. Optical collection, collimation and focusing of the radiation produce a THz beam. Such sources give the broadband short-pulse radiation necessary for time-domain spectroscopy and are used in the experimental TeraView set-up we used in the previous chapter [18].

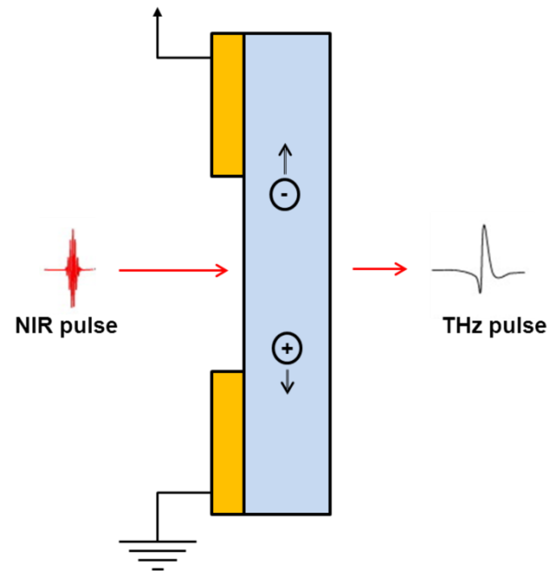

Figure 5.8: Laser-gated photoconductive semiconductor antenna

Continuous-wave mode consists in the generation of a monochromatic signal with a THz oscillation frequency obtained by the photomixing of two continuous-wave lasers of near wavelengths in a photodetector and detection of the oscillation corresponding to the frequency difference. The oscillation associated with the sum of the frequencies is too fast to play a role in this system (for two lasers with wavelengths of about 1.55 µm, it is around 400 THz). The photodetector needs to be ultra fast and stand high optical powers [19].

It is this last type of THz emitter that we try to design and build in the last part of this thesis. There is no report of such devices using the electrical and optical advantageous properties of the III-nitrides and the first step on this road is to prove that THz emission can be achieved with an InGaN-based THz photodetector.

5.2 Ultrafast photodiode for terahertz generation

Ultrafast photodiodes are realized using the heterojunction of semiconductors with different doping levels. Photodiodes are based on the rapid expulsion of the photo-generated charge

carriers by the electric field in the depleted zone. As with other electrical systems, the speed of the device depends mostly on two parameters: the carriers transit time and the time constant RC.

As the goal of our work is to only prove the feasibility of a photodiode emitting in the THz range, we will not detail the calculations leading to the dimensions used in our device.

5.2.1 Design of a terahertz photodiode

We base our work on the p-i-n and uni-travelling-carrier (UTC) photodiodes designed at IEMN, specifically the work of Alexandre Beck under the direction of Jean-François Lampin [20]. Adapting the models used for the InP/InGaAs to III-nitrides materials, we suggest the following design of a UTC 1.55 µm laser-based THz photodiode.

The band structure of a UTC photodiode is presented in Figure 5.9. The absorption of the photo-carriers and their expulsion are done in two separate zones to uncouple the need for a low junction capacity and the small carriers transit time. Electrons and holes are created in the absorption zone (AZ), a layer of n-doped InN. InN, because of its small bandgap energy (~ 0.7 eV), can be excited by a 1.55 µm laser, which is not the case for GaN or most InGaN compositions. The carriers diffuse through the AZ towards the InGaN-made collector as the electrical field is close to zero in the AZ. The choice of InGaN for the collector is also due to the need for a lattice adaptation layer. A material with a wider band gap (GaN) is used for the anode.

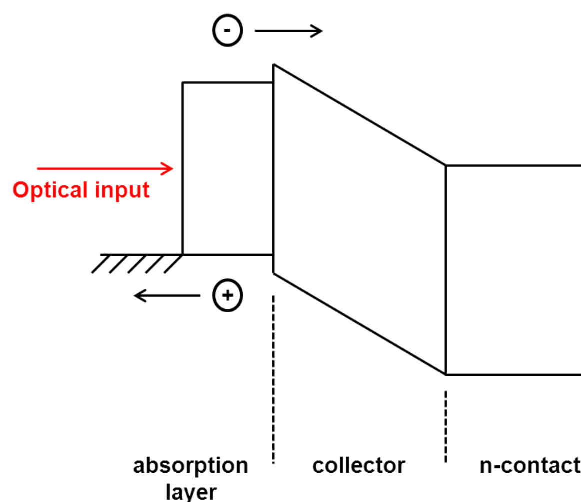

Figure 5.9: Band structure of a UTC photodiode

UTC photodiodes usually use a reverse band structure, with the AZ made of a p-type material and a n-type material-based diffusion barrier to use electrons (and their higher mobility) as the significant charge carriers. The photo-carriers are then generated in a zone where the holes are already in excess and the anode is providing a potential barrier that prevents the holes from circulating in the wrong direction [21]. However in our case, the difficulty to grow p-type InN is a constrain that forces us to switch to a device in which holes will be the significant carriers.

We use the small signal modelling to determine thicknesses of the AZ and of the collector. Considering the structure as a capacitor with a desired cut-off frequency of 1 THz and assuming a resistance of 50 Ω, we need the capacity of the structure to be around 3×10^{-15} F. For a capacitor surface of 1 μm × 1 μm, this leads to a thickness of 50 nm for the InGaN and InN layers together. We chose thicknesses of 30 nm and 20 nm for the AZ and the collector respectively. It is important to keep in mind that these are first values providing the dimension of a proof-of-concept and that a full analytical and numerical study will be necessary for the design of a more efficient device. The schematic view of the device is provided in Figure 5.10.

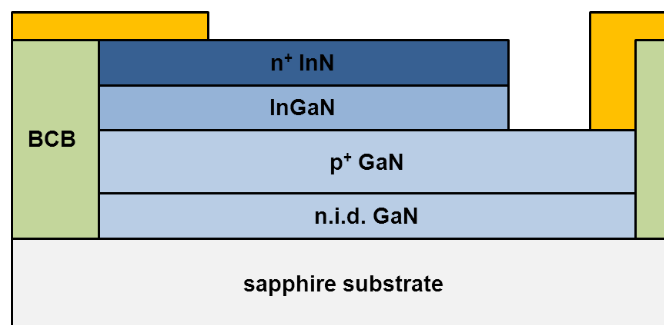

Figure 5.10: Suggested UTC photodiode design using an InN absorption layer and an InGaN collector

The device is connected to an equiangular spiral wideband antenna. The design of this planar antenna was proposed by Dyson in 1958 and has been extensively used since then for THz radiation [22].

5.2.2 Fabrication of a terahertz photodiode

5.2.2.1 Growth of the structure

The layer structure is grown by MOCVD at IMRE in accordance with what has already been discussed for thin films in chapter 2. The basic layer structure is described in Figure 5.11, where the n-type InN, undoped InGaN and n-type GaN layers are grown on a GaN-on-sapphire template:

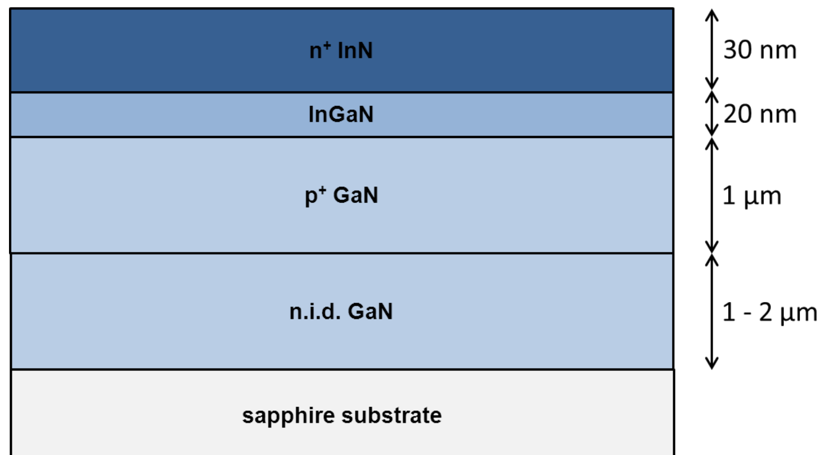

Figure 5.11: MOCVD-grown layer structure

5.2.2.2 Technological steps for the fabrication of the photodiode

We divide the technological processes to obtain the final device in three main steps: etching, planarization and metallization of the contacts and of the antenna.

a) Etching

There are two sub-tasks in this step: first, we need to free the InN absorption zone and InGaN collector and then isolate the device on the sapphire substrate. This is important as leaving some GaN on the substrate would create a capacitive effect when the antenna is added at the top of the structure in the final step.

Etching is done using Ar/Cl_2 inductively-coupled plasma (ICP) etching. Preliminary tests have been made to determine the etching speed through InN and GaN. The protected areas are covered using Microchemicals AZ n-LoF 2020 photoresist.

For fluxes of 10 sccm and 30 sccm for Cl_2 and Ar respectively with a reactive-ion etching power P_{RIE} = 40 W and an inductively-coupled plasma power P_{ICP} = 500 W, we obtain etching speeds of 16-17 nm.s^{-1} for GaN and 5-6 nm.s^{-1} for InN.

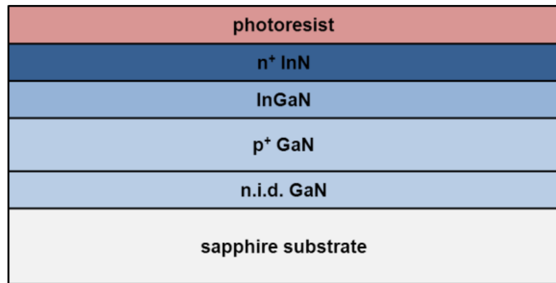

Photoresist deposit

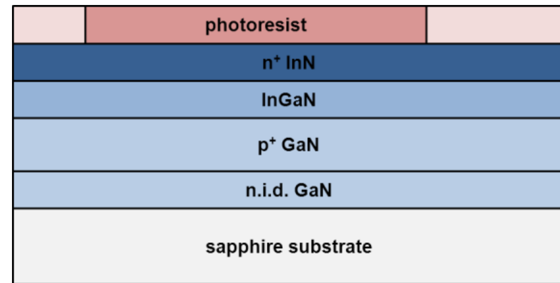

Photoresist exposure

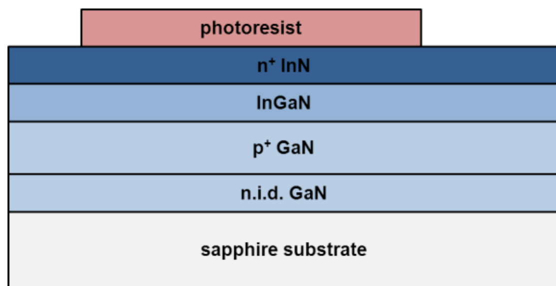

Photoresist development

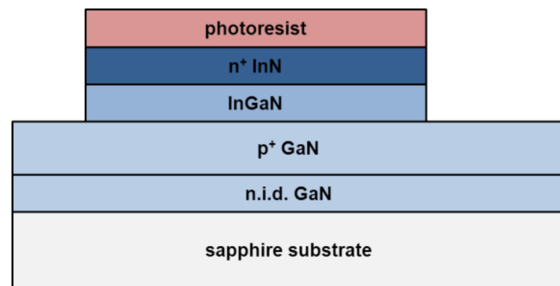

ICP etching of the InN and InGaN layers

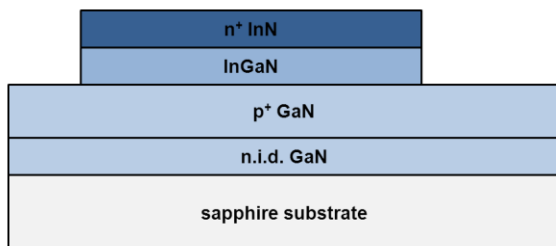

Photoresist removal

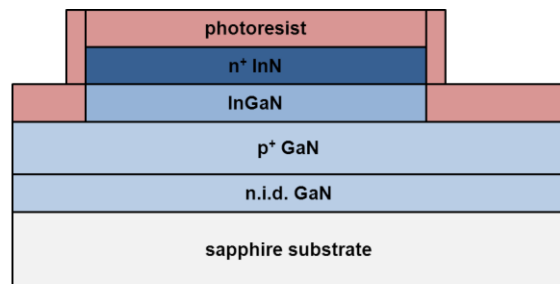

Photoresist deposit

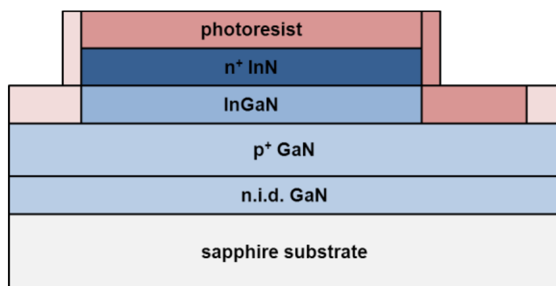

Photoresist exposure

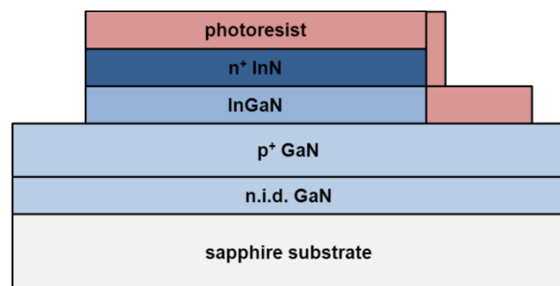

Photoresist development

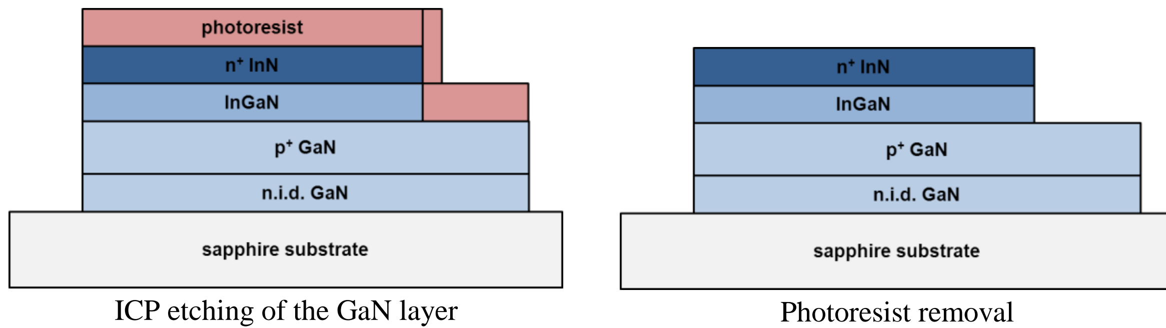

ICP etching of the GaN layer Photoresist removal

Figure 5.12: Step-by-step technological etching process

b) Planarization

Planarization, while simple in principle, is actually a challenging part of our technological process. We need to put the n and p metallic contacts in the same plane as the antenna, which requires us to handle 2 to 3 µm steps. If we were to put all our contacts directly on the sapphire, we would have to do the planarization in several steps, as current techniques only work with ~ 1 µm steps. Instead, we decide to bring all the contacts to a higher level and add a via to reach the GaN contact. Using photosensitive benzocyclobuten (BCB) photoresist, we can easily realize the operation. Wet etching enables us to access the photodiode.

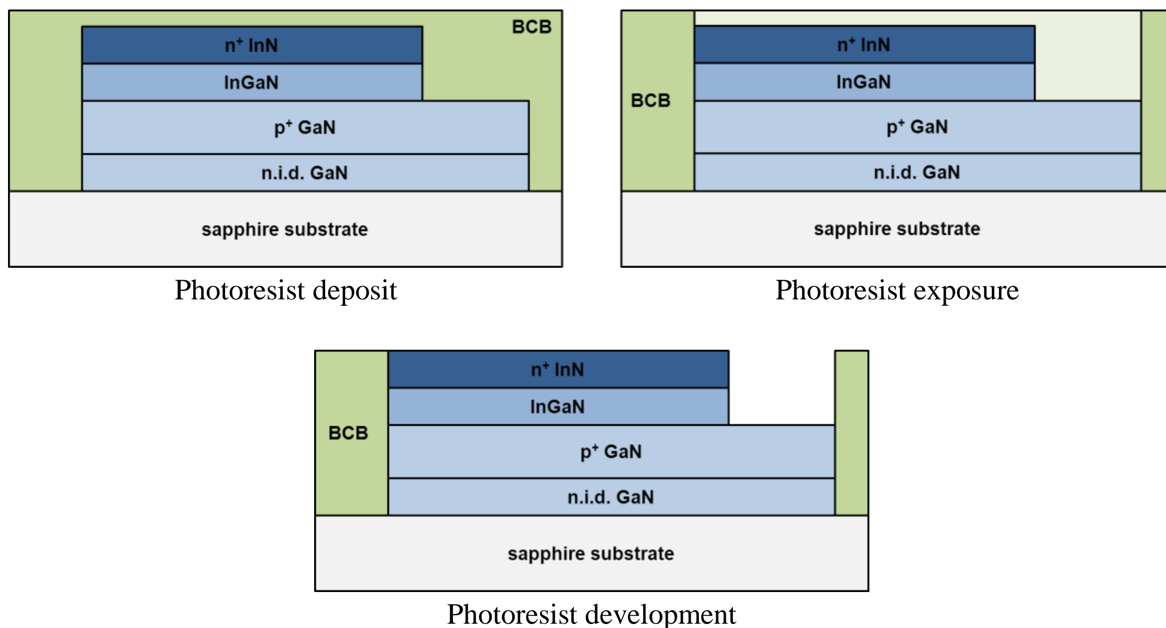

Photoresist deposit Photoresist exposure

Photoresist development

Figure 5.13: Step-by-step technological planarization process

c) Metallization

The final step of our process consists in adding the ohmic Ti/Al/Ni/Au contacts on GaN and InN [23] and deposit the antenna. A via is a prerequisite for the contact on GaN.

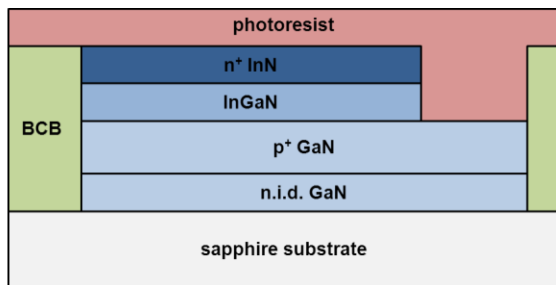

Photoresist deposit

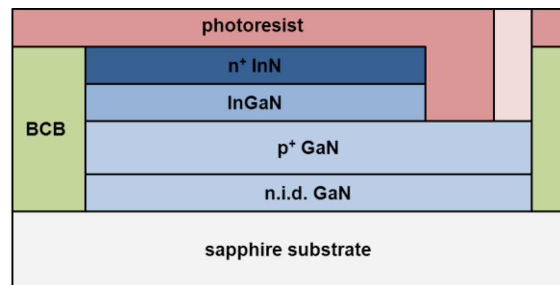

Photoresist exposure

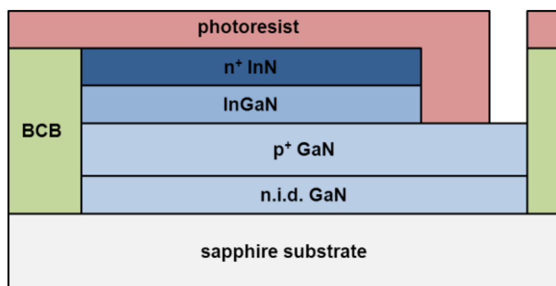

Photoresist development

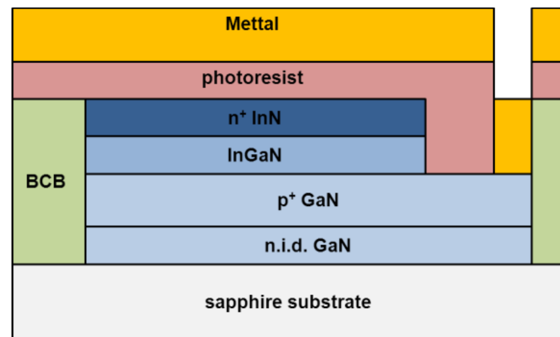

Via metallization

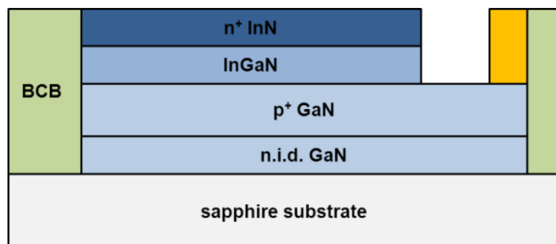

Lift-off

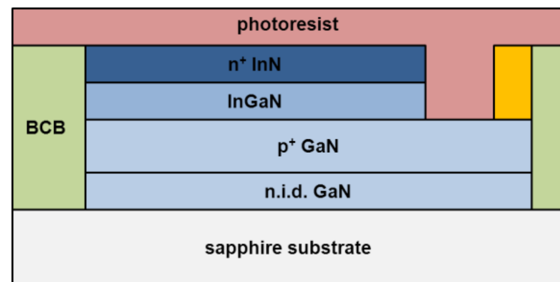

Photoresist deposit

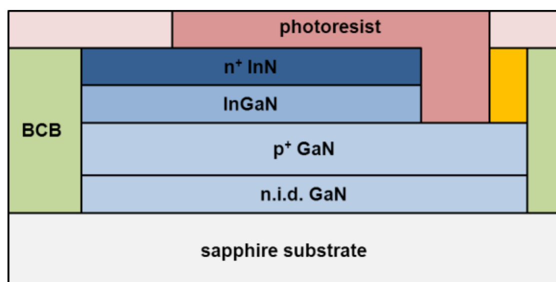

Photoresist exposure

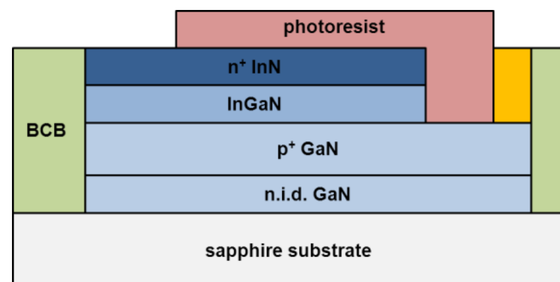

Photoresist development

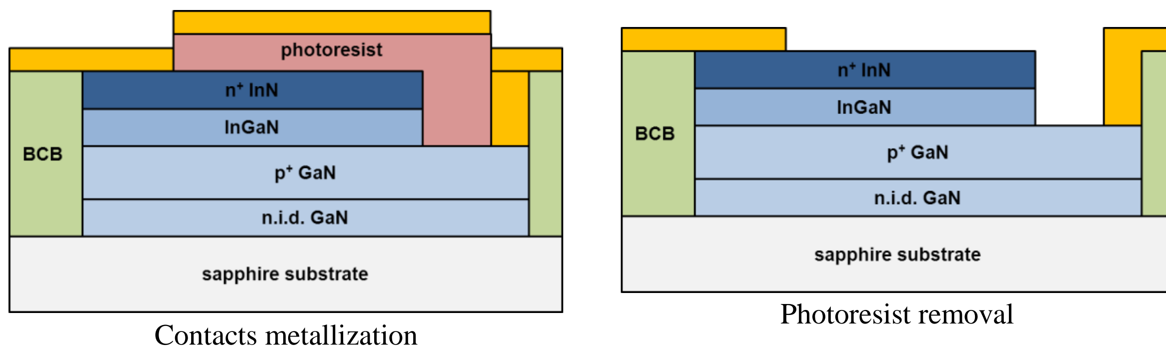

Figure 5.14: Step-by-step technological metallization process

We designed a series of masks to build the devices on 2-inch half-wafers. A number of photodiodes are drawn with different surfaces. For lower frequency (microwave) electrical testing purposes, a series of devices is also added without antennas but with coplanar lines for electrical interconnections. Figure 5.15 presents several top views of the masks designed using LayoutEditor: a view of the entire half-wafer, the detail of one device with and antenna, the photodiode at the center of an antenna (with an photodiode surface of 1 µm × 1 µm, but other devices exist with surfaces from 0.5 µm × 0.5 µm to 2.5 µm × 2.5 µm) and a view of a 1 µm × 1 µm device with coplanar lines (other dimensions vary from 0.5 µm × 0.5 µm to 100 µm × 100 µm). Resistance scales are also integrated to measure the p^+ GaN and n^+ InN conductivities.

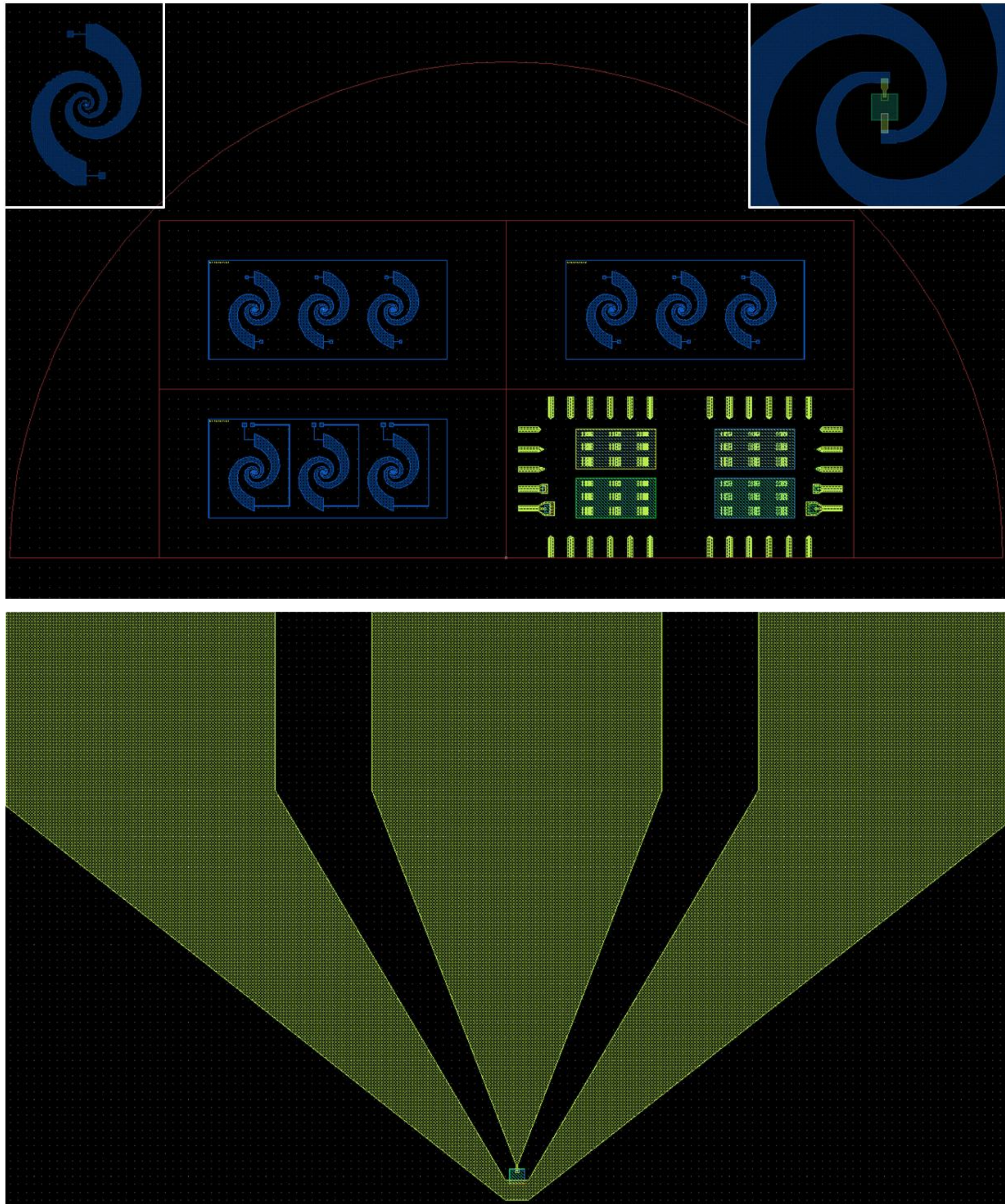

Figure 5.15: Masks for the design of the photodiodes. Global view of the semi-wafer (top), inserts detail one antenna (top left corner) and one photodiode (top right corner). Devices with coplanar lines are added for electrical microwave testing (bottom)

5.3 Conclusion and perspectives

Our initial target was to be able to characterize the device, but time constrain will not make this possible by the time of this writing. Still, the photodiode has been designed, the layers have been grown and the technological process is now well-defined. The fabrication process, while it's been engaged is unfinished. To investigate the capabilities of our device, extensive electrical and optical characterization will be required. IEMN possesses a number of electrical experimental equipment, as well as a THz photomixing characterization set-up under the supervision of Jean-François Lampin, head of the THz group at IEMN, that will prove a great help for the characterization of our device.

Ultimately, we hope to be able to prove that a device built using GaN, InGaN and InN can emit in the THz frequency domain. Our expectations towards efficiency are still somewhat limited for the moment as the component has not been designed with that focus in mind. There is also a lot of room for improvement in the growth of III-nitrides, especially for InN, and technological processes, while existent, are still far from mature. In any case, a positive result, even with low power output or frequency below our anticipation could be an important stepping stone on the path to a III-nitrides-based compact, efficient and tunable THz emitter working at room-temperature, opening new possibilities for an entire field of applications.

References

[1] M. Tonouchi, "Cutting-edge terahertz technology", *Nature Photon.* **1**, 97-105 (2007)

[2] W. Hafez, W. Snodgrass and M Feng. "12.5 nm base pseudomorphic heterojunction bipolar transistors achieving f_T = 710 GHz and f_{MAX} = 340 GHz", *Appl. Phys. Lett.* **87**, 252109 (2005)

[3] R. Krithivasan, Y. Lu, J.D. Cressler, J.S. Rieh, M.H. Khater, D. Ahlgren and G. Freeman, "Half-terahertz operation of SiGe HBTs". *IEEE Electron. Dev. Lett.* **27**, 567-569 (2006)

[4] W. Knap, J. Lusakowski, T. Parenty, S. Bollaert, A. Cappy, V.V. Popov and M.S. Shur, "Terahertz emission by plasma waves in 60 nm gate high electron mobility transistors", *Appl. Phys. Lett.* **84**, 2331-2333 (2004)

[5] N. Dyakonova, A. El Fatimy, J. Łusakowski, W. Knap, M.I. Dyakonov, M.A. Poisson, E. Morvan, S. Bollaert, A. Shchepetov, Y. Roelens, C. Gaquiere, D. Theron and A. Cappy, "Room-temperature terahertz emission from nanometer field-effect transistors", *Appl. Phys. Lett.* **88**, 141906 (2006)

[6] J.R. Söderström, E.R. Brown, C.D. Parker, L.J. Mahoney, J.Y. Yao, T.G. Andersson and T.C. McGill, "Growth and characterization of high current density, high-speed InAs/AlSb resonant tunneling diodes", *Appl. Phys. Lett.* **58**, 275-277 (1991)

[7] N. Orihashi, S. Suzuki and M. Asada, "One THz harmonic oscillation of resonant tunneling diodes", *Appl. Phys. Lett.* **87**, 233501 (2005)

[8] A.M. Kurakin, S.A. Vitusevich, S.V. Danylyuk, A.V. Naumov, C.T. Foxon, S.V. Novikov, N. Klein, H. Lüth and A.E. Belyaev, "Capacitance characterization of AlN/GaN double-barrier resonant tunnelling diodes", *Phys. Stat. Sol. (c)* **3**, 2265-2269 (2006)

[9] M.V. Petrychuk, A.E. Belyaev, A.M. Kurakin, S.V. Danylyuk, N. Klein and S.A. Vitusevich, "Mechanisms of current formation in resonant tunneling AlN/GaN heterostructures", *Appl. Phys. Lett.* **91**, 222112 (2007)

[10] J.S. Ward, G. Chattopadhyay, J. Gill, H. Javadi, C. Lee, R. Lin, A. Maestrini, F. Maiwald, I. Mehdi, E. Schlecht and P. Siegel, "Tunable broadband frequency-multiplied

terahertz sources", *33rd International Conference on Infrared, Millimeter, and Terahertz Waves Proceedings* (2008)

[11] H.W. Hübers, S.G. Pavlov and V.N. Shastin, "Terahertz lasers based on germanium and silicon", *Semicond. Sci. Technol.* **20**, S211-S221 (2005)

[12] J. Faist, F. Capasso, D.L. Sivco, C. Sirtori, A.L. Hutchinson, A.Y. Cho, "Quantum cascade laser", *Science* **264**, 553-556 (1994)

[13] R. Kohler, A. Tredicucci, F. Beltram, H.E. Beere, E.H. Linfield, A.G. Davies, D.A. Ritchie, R.C. Iotti and F. Rossi, "Terahertz semiconductor-heterostructure laser", *Nature* **417**, 156-159 (2002)

[14] B.S. Williams, S. Kumar, Q. Hu and J.L. Reno, "High-power terahertz quantum cascade lasers", *Electron. Lett.* **42**, 89-90 (2006)

[15] G. Scalari, C.Walther, J. Faist, H. Beere and D Ritchie, "Electrically switchable, twocolor quantum cascade laser emitting at 1.39 and 2.3 THz", *Appl. Phys. Lett.* **88**, 141102 (2006)

[16] B.S. Williams, S. Kumar, Q. Hu and J.L. Reno, "Operation of terahertz quantum-cascade lasers at 164 K in pulsed mode and at 117 K in continuous-wave mode", *Opt. Express* **13**, 3331-3339 (2005)

[17] E. Bellotti, K. Driscoll, T.D. Moustakas and R. Paiella, "Monte Carlo study of GaN versus GaAs terahertz quantum cascade structures", *Appl. Phys. Lett.* **92**, 101112 (2008)

[18] M. Moore, "Filling the THz gap with new applications", *Semiconductors Today Compounds & Advanced Silicon* **2**, 39-43 (2007)

[19] A. Satou, V. Ryzhii, I. Khmyrova, M. Ryzhii and M. S. Shur, "Characteristics of a terahertz photomixer based on a high-electron mobility transistor structure with optical input through the ungated regions", *J. Appl. Phys.* **95**, 2084 (2004)

[20] A. Beck, *Réalisation et Caractérisation de Photodiodes à Transport Unipolaire pour la Génération d'Ondes Térahertz*, PhD thesis, Université des Sciences et Technologies de Lille (2008)

[21] H. Ito, F. Nakajima, T. Furuta and T Ishibashi. “Continuous THz-wave generation using antenna-integrated uni-travelling-carrier photodiodes”, *Semiconductor Science and Technology* **20**, S191-S198 (2005)

[22] J.D. Dyson, “The equiangular spiral antenna”, *IRE Trans. Antennas Propag.* **7**, 181-187 (1959)

[23] Rohit Khanna, B. P. Gila, L. Stafford, S. J. Pearton, F. Ren, I. I. Kravchenko, Amir Dabiran and A. Osinsky, “Thermal stability of Ohmic contacts to InN”, *Appl. Phys. Lett.* **90**, 162107 (2007)

Conclusion

This thesis had set itself the goal to improve the knowledge of the scientific community on GaN, InN and their ternary alloy InGaN and to provide information on these materials that will make future InGaN-based device-oriented projects possible. In this framework, we have successfully grown by MOCVD thin films of GaN with various carrier concentrations, as well as $In_xGa_{1-x}N$ and InN on GaN-on-sapphire templates. Characterization through microscopy, X-ray diffraction, micro-photoluminescence and secondary ion-mass spectroscopy has detailed the numerous challenges and issues related to the synthesis of these materials and helped determining precisely the structure and composition of each sample.

The core of our work was focused on the optical characterization of these materials and the study of the evolution of the optical index with the indium fraction. This was achieved first in the visible/near infrared domain through ellipsometry thanks to collaboration with the University of Mons and through terahertz time-domain spectroscopy in the terahertz range under our partnership with IMRE. In both cases, we have set up an experimental process and an accurate, reliable and reproducible data analysis method that will be usable in the future as new samples are fabricated. There is still a lot of work to do to grow and characterize samples that enable us to obtain a broader picture on the evolution of the properties of InGaN on its full composition range, but ellipsometry and THz-TDS provide now-proven tools for this.

Of course, this characterization work is only a step towards the emergence of a new line of devices based on InGaN material. Recent works have shown the relevance of InGaN-based components and devices are starting to appear, taking advantages of the unique set of properties of InGaN. We hope that the contribution of this thesis will help fostering the III-nitrides family as a whole and provide a set of values and tools that will help characterize and design new pieces of hardware.

Applications in visible domain are already numerous and InGaN provides the base for candidates to more efficient devices, while in the terahertz range, there is hope that InGaN will be part of a solution to the source scarcity problem, making possible the fabrication of efficient, compact, tunable and room-temperature-operable sources and detectors. As the THz

domain is still a nascent field, there is room for new materials and applications and we strongly believe that InGaN has a set of properties that make it a suitable semiconductor candidate for a number of applications that are impossible to realize with the current material solutions.

Publications and communications

Articles in international journals

[J1] A. Gokarna, **A. Gauthier-Brun**, W. Liu, Y. Androussi, E. Dumont, E. Dogheche, J.H. Teng, S.J. Chua and D. Decoster, "Optical and microstructural properties versus indium content in $In_xGa_{1-x}N$ films grown by metal organic chemical vapor deposition", *Appl. Phys. Lett.* **96**, 191909 (2010)

[J2] **A. Gauthier-Brun**, J.H. Teng, E. Dogheche, W. Liu, A. Gokarna, M. Tonouchi, S.J. Chua and D. Decoster, "Properties of $In_xGa_{1-x}N$ films in terahertz range", *Appl. Phys. Lett.* **100**, 071913 (2012)

Articles in international conferences

[IC1] **A. Gauthier-Brun**, J.H. Teng, W. Liu, K. Takeya, M. Tonouchi, E. Dogheche, A. Gokarna, S.S. Norman, S.J. Chua and D. Decoster, *Properties of III-N in Terahertz Range*, ICMAT 2011, oral presentation

[IC2] **A. Gauthier-Brun**, J.H. Teng, W. Liu, M. Tonouchi, E. Dogheche, A. Gokarna, S.J. Chua, D. Decoster, *Properties of GaN and InN films in Terahertz Range*, HETECH 2011, oral presentation

[IC3] **A. Gauthier-Brun**, A. Gokarna, W. Liu, E. Dumont, J.H. Teng, E. Dogheche, S.J. Chua and D. Decoster, *Properties of InGaN Films over the Optical and Terahertz Ranges*, E-MRS 2012, poster

Abstract

The InGaN compound is a promising ternary alloy system that receives a lot of attentions thanks to its tunable bandgap that varies from the near infrared region to the near ultraviolet region. InGaN/GaN materials have been widely used in various applications like high efficiency solar cells, high-brightness blue to green light emitting diodes or laser diodes as well as non-phosphor based direct white light generation. The unique set of properties of this material also makes it a suitable candidate for a number of other new applications. However, to design efficient InGaN-based devices, it is a prerequisite to know the optical properties of InGaN films at the frequencies of interest and there is currently very little information on the index of GaN and $In_xGa_{1-x}N$ with x>0.07. In this thesis, we study and characterize the optical indices of GaN, InN and $In_xGa_{1-x}N$ thin films grown by metalorganic chemical vapor deposition with indium concentration varying up to x=0.14. We discuss the design and fabrication process of an InGaN-based ultrafast terahertz photodiode.

L'alliage ternaire InGaN reçoit beaucoup d'attention grâce à son énergie de bande interdite ajustable qui varie entre l'infrarouge et l'ultraviolet. Les matériaux GaN et InGaN sont largement utilisés dans de nombreuses applications telles que des cellules photovoltaïques à haute efficacité, des diodes électroluminescentes ou des diodes laser à forte luminosité allant du bleu au vert ou encore la génération de lumière blanche directe. L'ensemble des propriétés de ce matériau en fait aussi un candidat sérieux pour un certain nombre d'autres applications. Pour concevoir des composants à base d'InGaN, il est cependant vital de déterminer au préalable les propriétés optiques du matériau aux fréquences d'intérêt et il n'existe que très peu voire aucune communication sur les indices du GaN ou de l'$In_xGa_{1-x}N$ pour x>0.07. Nous étudions dans cette thèse la croissance par metalorganic chemical vapor deposition et la caractérisation des indices optiques de GaN, d'InN et d'$In_xGa_{1-x}N$ avec une concentration en indium variant jusqu'à x=0.14 dans les domaines de fréquence visible et térahertz et discutons la conception et le procédé de fabrication d'une photodiode térahertz ultrarapide.